

Design of Microstructured Fibers for Hollow Core Guidance

DISSERTATION

for the acquisition of the academic title

Doctor rerum naturalium (Dr. rer. nat.)

submitted to the council of the Faculty of Physics and Astronomy
of the
Friedrich Schiller University Jena



by M. Sc. Guangrui Li

born in Luoyang, China, on November 10, 1989

REVIEWERS:

1. Prof. Dr. Markus A. Schmidt
Leibniz Institute of Photonic Technology
2. Prof. Dr. Chris Poulton
University of Technology Sydney
3. Prof. Dr. Wei Ding
Jinan University

DAY OF THE DISPUTATION: May 3, 2022

Abstract

Instead of the traditional index guidance, microstructured fibers can guide light in a core of refractive index lower than that of its cladding using mechanisms like photonic band gap guidance, inhibited coupling guidance and anti-resonant guidance. Their guidance is usually leaky and depends on the photonic properties of their structured cladding. Specifically, photonic band gap guidance is possible with photonic crystals, whose photonic band gaps appear below the refractive index index of the core. Guidance in a low-index core or hollow core guidance, is of interest for applications in the fields of bioanalytic, quantum gas, lasers and others that involve interacting of the light with confined matter of low refractive index. My work is aimed at investigating the possibility of hollow core guidance with an all-solid microstructured cladding. Ideally, such a hollow core waveguide is expected to have obvious guidance advantages over capillaries. Besides, it also surpasses the holey hollow core band gap fibers in the optofluidic applications by avoiding undesired penetration of the liquid into the cladding channels. To achieve the design of the ideal hollow core waveguide, I developed two models for all relevant modes in microstructured fibers: an analytical method with binary functions and a reflection-based planar model.

For analysis of a photonic crystal cladding, which consists of high index strands arranged in hexagonal arrays embedded in a low index matrix, an analytical method was developed using binary functions to straightforwardly identify its band gaps. The analytical method enables analysis of parameter changes that lead to deeper band gaps. It indicates that the guidance of light in air is mostly possible with free-standing strands with air background instead of a solid silica background. This was proven experimentally by implementing the free-standing strands forming a “light cage” with 3D direct laser writing. Moreover, the analytical method with binary functions is so convenient that it is used to analyze the transmission bands of liquid-filled band gap fibers. The results allow me to directly determine the refractive index of the liquids filled in fibers through their transmission spectra, offering

another way to investigate light-matter interaction with band gap fibers.

While the concept of photonic band gap is more about ideal periodic structures extended into infinite, the reflection and transmission analysis with a reflection-based planar model is more practical to be used for waveguides with finite periodic structures and deliberately induced disorder. The reflection-based planar model gives an insight into the scattering of the structured cladding and offers an analytical approximation for the complex refractive index of the core modes. Specifically, the reflection-based planar model was applied to analyze the core modes of a single-ring microstructured fiber, showing a reduction of loss for the case with deliberately induced modification of cylinders in the cladding. Further, a design of water-core all-solid band gap fiber was proven by the mode analysis using the reflection-based planar model, which was also confirmed with numerical calculation.

Zusammenfassung

Anstelle der traditionellen Indexführung können mikrostrukturierte Fasern Licht in einem Kern mit einem niedrigeren Brechungsindex als dem des Mantels führen, indem sie Mechanismen wie die photonische Bandlückenführung, die sogenannte Inhibited-Coupling und die Antiresonanzführung nutzen. Ihre Führung ist in der Regel undicht und hängt von den photonischen Eigenschaften des strukturierten Mantels ab. Die Führung der photonischen Bandlücke ist insbesondere mit photonischen Kristallen möglich, deren photonische Bandlücken unterhalb des Brechungsindex des Kerns auftreten. Die Führung in einem Kern mit niedrigem Brechungsindex oder in einem Hohlkern ist für Anwendungen in den Bereichen Bioanalytik, Quantengas, Lasers und andere, bei denen das Licht mit eingeschlossener Materie mit niedrigem Brechungsindex wechselwirkt, interessant. Meine Arbeit zielt darauf ab, die Möglichkeit der Hohlkernführung mit einem vollständig festen mikrostrukturierten Mantel zu untersuchen. Im Idealfall sollte ein solcher Hohlkernwellenleiter deutliche Vorteile gegenüber Kapillaren haben. Außerdem übertrifft er die löchrigen Hohlkern-Bandlückenfasern in den optofluidischen Anwendungen, indem er das unerwünschte Eindringen der Flüssigkeit in die Mantelkanäle verhindert. Um das Design des idealen Hohlleiters zu erreichen, habe ich zwei Modelle für alle relevanten Moden in mikrostrukturierten Fasern entwickelt: eine analytische Methode mit binären Funktionen und ein auf Reflexion basierendes planares Modell.

Für die Analyse eines photonischen Kristallmantels, der aus Strängen mit hohem Brechungsindex besteht, die in hexagonalen Arrays angeordnet und in eine Matrix mit niedrigem Brechungsindex eingebettet sind, wurde eine analytische Methode entwickelt, bei der binäre Funktionen verwendet werden, um die Bandlücken auf einfache Weise zu ermitteln. Die analytische Methode ermöglicht die Analyse von Parameteränderungen, die zu tieferen Bandlücken führen. Sie zeigt, dass die Lichtführung in der Luft vor allem bei freistehenden Strängen mit Lufthintergrund anstelle eines festen Siliziumdioxid-Hintergrunds möglich ist. Dies wurde experimentell bewiesen, indem die freistehenden Stränge, die einen "Lichtkäfig" bilden, mit 3D-Laserdirektschreiben implementiert wurden. Darüber hinaus funktioniert die analytische Methode mit binären Funktionen so gut, dass sie zur Analyse der Transmissionsbänder von flüssigkeitsgefüllten Bandlückenfasern

verwendet wird. Die Ergebnisse ermöglichen es mir, den Brechungsindex der in die Fasern eingefüllten Flüssigkeiten anhand ihrer Transmissionsspektren direkt zu bestimmen, was eine weitere Möglichkeit zur Untersuchung der Licht-Materie-Wechselwirkung mit Fasern mit Bandlücken darstellt.

Während sich das Konzept der photonischen Bandlücke eher auf ideale periodische Strukturen bezieht, die ins Unendliche ausgedehnt sind, ist die Reflexions- und Transmissionsanalyse mit einem reflexionsbasierten planaren Modell praktischer für Wellenleiter mit endlichen periodischen Strukturen und absichtlich herbeigeführter Unordnung. Das reflexionsbasierte planare Modell gibt einen Einblick in die Streuung des strukturierten Mantels und bietet eine analytische Näherung für den komplexen Brechungsindex der Kernmoden. Konkret wurde das reflexionsbasierte planare Modell zur Analyse der Kernmoden einer mikrostrukturierten Ein-Ring-Faser angewandt und zeigte eine Verringerung des Verlusts für den Fall einer absichtlich herbeigeführten Modifikation der Zylinder im Mantel. Weiterhin wurde durch die Modenanalyse unter Verwendung des reflexionsbasierten planaren Modells ein Design für eine Festkörper-Bandlückenfaser mit Wasserkern nachgewiesen, das auch durch numerische Berechnungen bestätigt wurde.

Acknowledgement

I would like to express my sincere appreciation to my supervisor professor Markus A. Schmidt, who has offered me the chance to work on this exciting topic and guides me all the way with constant passion for the research and attitude of a professional. Without his persistent help, this thesis would not have been possible.

I would like to thank individually my colleague Ron Fatobene for passing his knowledge on using COMSOL generously to help me start my work right away and Matthias Zeisberger for his patient support for those discussion on reflection-based model.

In addition, my appreciation is also to my colleagues in the research group of hybrid fiber, who provide inspiring and cheering working environment and the Leibniz Institute for Photonic Technology, where all the events and work happened.

And finally many thanks to my big family far away in China, who support me unconditionally, and to my husband Kailin Niu for his fully understanding and caring, and to my friends for the warm company here in Germany.

Nomenclature

Physics Constants

β	Propagation constant
Δ	Refractive index profile height
Λ	Pitch of photonic crystal
n	Refractive index

Abbreviations

AR	Anti-Resonant
ARROW	Anti-Resonant Reflecting Optical Waveguide
DOS	Density of States
FEM	Finite Element Method
GVD	Group Velocity Dispersion
LFBG	Liquid-filled Band Gap
MWEQ	Maxwells Equations
PBG	Photonic Band Gap
PCF	Photonic Crystal Fiber
RI	Refractive Index
RMSE	Root Mean Square Error
SEM	Scanning Electron Microscope
TOC	Thermo-optic coefficient

Other Symbols

C_2Cl_4 Tetrachloroethylene

CO_2 Carbon dioxide

CS_2 Carbon disulphide

Contents

1	Introduction	1
1.1	Context	1
1.2	Objective of the study	6
1.3	Structure of the thesis	8
2	Theoretical Background	9
2.1	Electromagnetic Wave	9
2.1.1	Maxwell's equations	9
2.1.2	Scalar wave equation and the boundary conditions . .	11
2.1.3	Scaling properties of the Maxwell equations	13
2.2	Optical properties of matter	13
2.2.1	Sellmeier formula	13
2.2.2	Thermo-optic coefficient	14
2.3	Modes in waveguides	15
2.3.1	Guided modes in a step index fiber	16
2.3.2	Bloch modes in photonic crystals	19
2.3.3	Defect modes and the reflection model	23
2.4	Numerical methods	27
2.4.1	Finite element method	27
2.4.2	Multipole method	29
3	Results: Models to investigate light guidance with microstructured cladding	33
3.1	Photonic band gap maps	33
3.1.1	Model for calculating band gap maps with binary functions	34
3.1.2	Parameter effects on band gaps	39
3.2	Reflection from a microstructured cladding	43
3.2.1	Reflection-based model for calculation of core modes .	43

3.2.2	Parameter sweeping of the structure	48
3.3	Conclusion	51
4	Results: Novel hollow core waveguides	55
4.1	Guidance in a water core	55
4.1.1	Photonic band gap for light guidance in a water core .	57
4.1.2	Reflection model for the water-core all-solid photonic band gap fiber	58
4.1.3	Results and discussion	61
4.2	Guidance in an air core	68
4.2.1	Light-cage written by 3D direct laser writing	70
4.2.2	Optical characterization of a Light cage	72
4.3	Conclusion	75
5	Results: Sensing with band gap effect	77
5.1	Method	77
5.1.1	Fabrication of LFBG fibers	78
5.1.2	Optical characterization and analysis of the refractive index	81
5.2	Results	84
5.2.1	Refractive index of a bi-mixture system	84
5.2.2	Temperature dependence of refractive index	88
5.3	Conclusion	92
6	Conclusion	95
	Bibliography	99

1.1 Context

Conventional optical fibers have been popularly used in optical communication but still possess certain unwanted effects caused by the scattering, absorption and material dispersion of their solid core. Specifically, the solid core made of fused silica exhibits scattering from the minute variations in the density of the glass (Rayleigh scattering) and absorption from vibrational resonance of silica molecules at mid-infrared wavelengths [1–3]. Further absorption in the solid core is caused by the presence of impurities, especially the inevitable -OH group from contamination with water during the fabrication process [4]. The material dispersion of the solid core dominates the group velocity dispersion and nonlinear optical effects of conventional fibers [5]. As a result, the clarity of a conventional optical fiber is limited and the propagation of pulses in conventional optical fibers faces inevitable spectral broadening and unexpected nonlinear phenomena. These effects are obstacles to using optical fibers for numerous real-world applications: for example, research on the spectral fingerprint of gases requiring guidance in the mid-infrared region; high energy delivery for ultrashort pulse lasers expecting maintaining pulse duration, beam quality, and power level. To avoid the obstacles with conventional fibers, a hollow core optical fiber is attractive for offering guidance with lower Rayleigh scattering, lower absorption and lower nonlinearity.

Moreover, hollow core waveguides are expected to benefit future research into light-matter interaction, i.e. optical sensing, spectroscopy and nonlinear optical processes in gases. Previous research on light-matter interaction is based on focused free-space laser beams or light propagating in a large core capillary, which is of low efficiency and requires rather high power. Other advanced investigation methods for light-matter interaction are using the evanescent field of a tapered waveguide [6] or the enhanced field of the surface plasmonic resonances of metal elements [7]. Both fields are localized, only offering limited interaction areas. In contrast, with hollow core guidance, light can be directly guided in the targeted matter over a long distance with a high-quality beam profile, offering much more effective light-matter interaction .

Given the above, the development of hollow core fibers offers solutions for applications of optical fibers requiring low loss in a wide wavelength region or low nonlinearity for pulse propagation, as well as a novel platform for light-matter interaction. A promising solution for hollow core guidance is microstructured fibers using claddings of microstructured materials, like photonic crystals.

Photonic crystal

A photonic crystal is an optical material composed of periodic arrangement of material on a scale comparable to optical wavelengths. Photonic crystals in nature account for structural coloration, for example, the iridescent colors of precious opals or peacock tail feathers. The physics behind this phenomenon lies in the interference of the scattered light from the fine structured materials. The optical properties of photonic crystals highly depend on their structures, offering a convenient way to manipulate light.

The concept of photonic crystal was first brought up with promising applications in 1987 in the work by Yablonovitch and John [8, 9]. After that, these optical materials received significant attention. Photonic crystals of one, two and three dimensions have been fabricated based on demands for suppressing spontaneous emission of light in semiconductor lasers [8, 10], improving solar cells efficiency [11, 12], and applications as optical waveguides [13, 14].

Optical properties of a photonic crystal are normally characterized by photonic bands and photonic band gaps, as an analog to the bands and band gaps of an ionic lattice for electrons in solids [15]. While the band in solid state physics indicates the energy states of an electron allowed in the crystal, the photonic band shows the spectral range of constructive interference, i.e. light modes, supported in the photonic crystal. For example, in the direction that the material is periodic arranged, the light of the wavelengths in the photonic band can propagate in the photonic crystal, while the light of the wavelengths in the photonic band gap is forbidden to propagate and reflected by the photonic crystal. The inhibited propagation in the photonic band gaps offers a novel possibility to achieve confinement of light with photonic crystals.

Photonic crystal fibers

One important application of photonic crystals is the photonic crystal fiber (PCF). A photonic crystal fiber consists of a two dimensional photonic crystal

in the transverse plane and is invariant along the fiber axis. It has a purposely induced defect, i.e. any structural feature that breaks the periodicity of the photonic crystal, as core. Such defect core can be of a refractive index either higher or lower than that of the cladding using different guiding mechanisms, while the core of conventional fibers is always of a higher refractive index for guidance with total internal reflection. In particular, the guiding properties of a photonic crystal fiber can be manipulated by its cladding structure in ways not previously attainable, resulting in rapidly growing interest in developing photonic crystal fibers.

The fabrication of PCFs is, however, highly challenging. The first PCF was reported to be successfully fabricated in 1996 by the group of Russell [16], which was followed with an explosion of all kinds of PCFs [17, 18]. To fabricate a PCF of silica, the stack-and-draw technique [18] has been most widely used. The process of stack-and-draw technique includes: first, the preform, a scaled-up model of the desired fiber structure, is created by stacking millimeter-size capillaries together and inserting the stack into a glass tube; then, the preform is fused during drawing into the cane, which has a diameter of millimeter; finally, the cane is drawn into the fiber of desired dimensions. The parameters of the fabrication process such as the temperature, preform feeding rate, drawing speed and the air-pressure applied inside the preform must be carefully tuned to have structures of regularity. With the stack-and-draw technique, hundreds of meters PCFs with structured cladding can be fabricated from a single preform. Alternatively, extrusion-and-draw technology has also been reported for the fabrication of soft glass PCFs [19]. In a recent work, polymer PCFs of different microstructures were directly fabricated with an extrusion-only technology [20]. Meanwhile, a hollow-core concentric ring structure fiber of two different materials was fabricated by drawing a layered preform, which in turn was formed by depositing layers onto a film and subsequent rolling of the coated film into a tube [21]. Considering the drawing process, the combined materials have to be thermally compatible to avoid cracking or delamination in the layered structure. In addition, hybrid photonic crystal fibers were fabricated by combining semiconductors, soft glasses or liquids into all-silica PCFs [22–25]. Further post-processing methods were also developed to modify photonic crystal fibers for novel applications, like photonic crystal fibers Bragg gratings [26] or exposed-core fibers [27, 28].

One kind of PCFs has a core with a refractive index higher than that of its photonic crystal cladding, i.e. a solid core and a cladding of numerous air voids. The guidance mechanism in such PCFs is referred to as modified total internal reflection, for unlike cladding of conventional fibers, the photonic crystal cladding has dispersion dominated by structural dispersion. Structural dispersion corresponds to the dispersion of the supported modes and can be engineered by the structure of the material. Therefore, with proper designs, such PCFs exhibit unique guiding properties, like single-mode propagation in a broad wavelength range independent of core size[29, 30] and near-zero flattened modal dispersion[31]. Moreover, such PCFs allow higher index contrast of core-cladding and smaller attainable core, leading to high nonlinear response with anomalous group-velocity dispersion (GVD) in the visible range[32–34]. Such PCFs are used particularly for high-power delivery and lasers requiring large mode area (LMA) single-mode guidance[30, 35] and the generation of a single-mode broadband optical supercontinuum [33, 36, 37].

The other kind of PCFs can guide light in a core of refractive index lower than that of its cladding. Specifically, their cladding consists of a high ratio of the low-index part with arrays of connected high-index junctions or even isolated high-index strands in case of hollow-core band gap fibers [38, 39] or all-solid band gap fibers[40, 41] respectively. In these cases, the dispersion of modes in the photonic crystal cladding form photonic bands and band gaps [42]. Such PCFs exhibit radically different guiding properties, i.e. spectral selective transmission, strong mode dispersion near band gap edges, and offer guidance in a low-index core. The work in this thesis is focused on this kind of PCFs.

Development of hollow core fibers

Hollow core fibers appeared last century and are still evolving along with fabrication techniques and an increased understanding of their working principle. So far, hollow core guidance has been achieved with Bragg fibers, band gap hollow core fibers, Kagome fibers and negative curvature fibers.

The first non-capillary hollow core fiber shown to guide light had a cylindrical hollow core surrounded by periodic multilayer films of alternating high and low refractive index, i.e. a Bragg fiber. The possibility of using Bragg reflection from a multiannulus cladding in a cylindrical fiber to guide light in a low-index core was first proposed and analyzed by Yeh et al. in 1978, show-

ing light guidance with mode filtering effect[43]. Later, researchers reported on the design of multilayer films to have omnidirectional reflectivity[44], which lead to a hollow-core Bragg fiber confining light by omnidirectional reflection (figure 1.1(A))[21]. Such omnidirectional Bragg fibers have stratified cladding with adequate index contrast to provide photonic band gaps. One such fiber design achieves loss of around 1.0 dB m^{-1} at $10.6 \mu\text{m}$ wavelength for the carbon dioxide (CO_2) laser light and is applied to deliver high power CO_2 laser for surgery[45]. Further applications of such fibers working in shorter wavelengths below $2 \mu\text{m}$ are limited by the challenges in fabrication and finding new material systems with compatible thermal and thermo-mechanical properties.

Then, hollow-core PCFs with cladding of two-dimensional periodic structures were developed based on the stack-and-draw technique. The hollow core guidance in a silica-air photonic crystal fiber permitted by the full 2D band gaps was first proposed by Birks et al. in 1995[46] and then experimentally proven by the light guidance in a large air core surrounded with triangular array of air holes in silica[38]. Better guidance in this kind of hollow core photonic crystal fibers was later achieved by increasing the air filling fraction in the holey cladding to a structure as shown in figure 1.1(B). It has been shown that loss of such hollow-core photonic crystal fiber can be reduced to 1.2 dB km^{-1} [47], an order higher than the achievable loss of conventional fibers. The loss is dominated by the scattering due to the surface roughness from the frozen-in surface capillary waves.

The guidance of light in the above described hollow-core fibers is ensured by the band gaps of the cladding modes, in which no core modes propagate into the cladding. However, band gap is not the prerequisite for guidance. Kagome fibers, with a lattice of thin layers around the hollow core, can guide light in a wide range of wavelengths where the density of the cladding modes is relatively low. The guidance mechanism in this case is referred to as inhibited coupling guidance for the core and cladding modes of same effective indexes hardly couple with each other [48–50]. Kagome fibers show relatively high loss, but offer broadband guidance in a hollow-core inspiring applications in gas-based nonlinear optics [51–53].

Further understanding of the guidance mechanism has shown that for Kagome fibers, only the first few layers around the hollow-core matters for the confinement loss (not the case for bend loss), leading to the simplified

version of such fibers [54–56]. The simplified fibers are usually referred to as anti-resonant fibers, which have high losses at the wavelengths consistent with the resonances of the high-index structures in the cladding as indicated by the anti-resonant reflecting optical waveguide (ARROW) model[57, 58]. Later research indicated that the shape of the layer around the core can be designed to enhance the coupling inhibition[59–61], which leads to the so-called negative curvature fibers as depicted in figure 1.1(C-F). Negative curvature fibers play an important role for hollow core guidance in recent years for the reduced complexity in fabrication and the promised possibility of lower loss than conventional fibers [62–67].

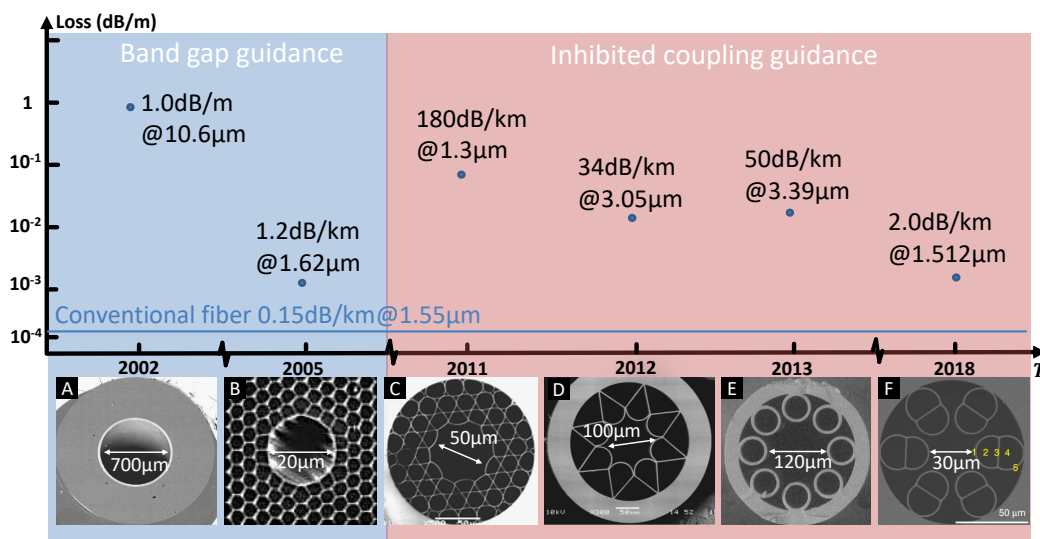


Fig. 1.1: Key development of hollow core fibers with the representative structures shown by their SEM picture (A-F). The indicated loss levels at certain wavelengths correspond to the structures of the labeled core dimensions [21, 47, 59, 65, 68, 69].

1.2 Objective of the study

Photonic crystals have been developed as a powerful tool to manipulate light without constraints of ready natural materials. Particularly, for hollow core guidance, instead of searching for materials with suitable spectral properties (like metals, working for limited frequencies), we can use a photonic crystal. The spectral characteristics of the photonic crystal can be designed straightforwardly with the refractive index contrast of its component materials and the dimensions of the structure. Many kinds of hollow core fibers, using band gaps or inhibited coupling, have been reported as introduced in the last

section. However, their holey cladding makes them delicate and not suitable for some applications requiring guidance of light in liquids.

Our key objective is to investigate the possibility to have hollow core guidance with an all-solid microstructured cladding. Ideally, such a hollow core waveguide has obvious guidance advantages over capillaries and also surpasses the holey hollow core band gap fibers in the optofluidic applications by avoiding undesired penetration of the liquid into the cladding channels. For the objective, we propose a conceptual hollow core waveguide (figure 1.2), which has a large hollow core in the center and a cladding of the all-solid photonic crystal fiber. The all-solid photonic crystal cladding, which consists of high index strands in periodic arrays embedded in a low index matrix, guides light in a solid core for all-solid band gap fibers [40, 41] and no hollow core guidance with it has been reported.

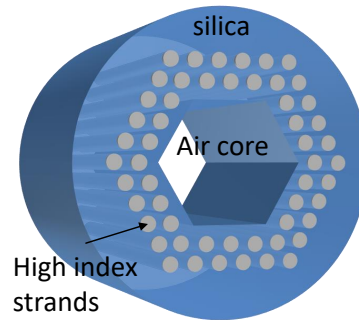


Fig. 1.2: Depicture of a hollow core fiber with all-solid photonic crystal cladding.

To achieve guidance in the proposed waveguide, the work is focused on:

- modeling the band gap of all-solid band gap cladding.
- analyzing the key parameters of all-solid band gap cladding leading to band gaps below the low index material in the core (air/liquids).
- modeling the guided core modes with all-solid photonic crystal cladding.
- investigating loss dependence of the core modes on specified disorder induced in the cladding structure.
- designing the proposed hollow core fiber with a central hollow core and an all-solid cladding.

1.3 Structure of the thesis

In the thesis, two models were developed for all relevant modes in microstructured fibers: an analytical method with binary functions and a reflection-based planar model, which were applied for different types of hollow core waveguides. The contents of the following chapters are briefly introduced here.

Chapter 2 includes the physical background of light propagation and modes in fibers based on the electromagnetic wave theory. Specifically, the basics of analytical methods as well as the numerical simulation methods are introduced.

In **Chapter 3**, an analytical method with binary functions is developed offering a straightforward way to identify the band gaps of an all-solid band gap cladding. This method is used for analyzing the key parameters affecting the depth of the band gaps. Another semi-analytical method is developed for the core modes in a large core microstructured fiber. This method is applied to a large core anti-resonant fiber to calculate the complex effective index of the core modes and do massive parameters sweeping for its loss dependence. It is shown that a reduction of loss is achieved for the case with deliberately induced disorder in the cladding.

In **Chapter 4**, a design of water core all-solid band gap cladding fiber is proven. An intensive study of the guided modes in the designed fiber is done with the self-developed semi-analytical method, which is also confirmed with numerical simulations. Besides, a hollow core waveguide, which consists of suspended polymer strands, is analyzed theoretically with simulations and experimentally implemented on chip with 3D laser writing. It shows guidance of light in the visible region in an air core.

In **Chapter 5**, the analytical method with binary functions for simulating the band gaps of all-solid band gap cladding is used to analyze the transmission bands of liquid-filled band gap fibers. The results allow direct determination of the refractive index of the liquids filled in fibers and show the thermal effect of the filled liquids in a wide spectral range.

These chapters are followed by a conclusion of the work and an outlook for further research on this topic in **Chapter 6**.

This part of the thesis includes the theory that my work is based on. It starts with the electromagnetic waves described by Maxwell's equations and their interaction with matters. Then, the modes in waveguides, including conventional step index fibers and photonic crystal fibers, are introduced in detail. The involved numerical simulation methods are briefly introduced at the end of this chapter. All discussions here are from the view of classic physics, quantum optics is beyond the scope of this work.

2.1 Electromagnetic Wave

Light can be described as electromagnetic waves following Maxwell's equations. The interaction of light with materials happens through the magnetization and polarization of the material as shown by the constitutive relations. Based on Maxwell's equations and the constitutive relations, solutions of electromagnetic waves in dielectric medium of any shape are theoretically solvable with heavy numerical calculation. A less complex case of circular symmetry medium with step index profile can be solved analytically using scalar wave equation and boundary conditions of Maxwell's equations. The scaling properties of the electromagnetic wave should be noticed for a straightforward extension of the solutions from one case to another. Details about the relevant derivation could be found in any textbooks on photonics and waveguides, for example [70, 71].

2.1.1 Maxwell's equations

In electromagnetic theory, the propagation of the electromagnetic wave is well described by **Maxwell's equations**:

$$\nabla \times \mathbf{E} = -\frac{\partial \mathbf{B}}{\partial t}, \quad (2.1a)$$

$$\nabla \times \mathbf{H} = \mathbf{j} + \frac{\partial \mathbf{D}}{\partial t}, \quad (2.1b)$$

$$\nabla \cdot \mathbf{D} = \rho, \quad (2.1c)$$

$$\nabla \cdot \mathbf{B} = 0. \quad (2.1d)$$

where $\mathbf{E}(\mathbf{r}, t)$ is electric field, $\mathbf{H}(\mathbf{r}, t)$ magnetic field, $\mathbf{D}(\mathbf{r}, t)$ electric flux density, $\mathbf{B}(\mathbf{r}, t)$ magnetic flux density, $\mathbf{j}(\mathbf{r}, t)$ conductive current density and ρ free

charge density. The electric and magnetic flux density $\mathbf{D}(\mathbf{r}, t)$ and $\mathbf{B}(\mathbf{r}, t)$ are related to the fields $\mathbf{E}(\mathbf{r}, t)$ and $\mathbf{H}(\mathbf{r}, t)$ with the electric and magnetic properties of the medium.

$$\mathbf{D} = \epsilon_0 \mathbf{E} + \mathbf{P}, \quad (2.2a)$$

$$\mathbf{B} = \mu_0 (\mathbf{H} + \mathbf{M}). \quad (2.2b)$$

where $\mu_0 = 4\pi \times 10^{-7} \text{Vs/Am}$ is the magnetic constant (permeability) of vacuum, $\epsilon_0 = 8,854 \times 10^{-12} \text{As/Vm}$ is the electric constant (permittivity) of vacuum. This is the so called **constitutive relations**. For nonmagnetic dielectric medium, magnetization density $\mathbf{M}(\mathbf{r}, t) = 0$. The polarization density $\mathbf{P}(\mathbf{r}, t)$ represents the macroscopic sum of the electric dipoles induced by the electric field in the medium, which can be expressed with the following equation:

$$\mathbf{P} = \epsilon_0 \chi \mathbf{E} \quad (2.3)$$

where χ is the electric susceptibility of materials. Then, the permittivity of materials is defined as $\epsilon = \epsilon_0 \epsilon_r = \epsilon_0 (1 + \chi)$, where ϵ_r is the relative permittivity of materials. Therefore, for a nonmagnetic medium with relative permittivity ϵ_r , the general case throughout our work, the constitutive relations is reduced to:

$$\mathbf{D} = \epsilon_0 \epsilon_r \mathbf{E}, \quad (2.4a)$$

$$\mathbf{B} = \mu_0 \mathbf{H}. \quad (2.4b)$$

Using these constitutive relations (Eqs. 2.4), the wave equation for electric field in a medium is derived from Maxwell's equations (Eqs. 2.1). To get rid of the partial derivatives, the field is decomposed into monochromatic waves with complex amplitude and harmonic time dependence, $\mathbf{E}(\mathbf{r}, t) = \bar{\mathbf{E}}(\mathbf{r}) e^{i\omega t}$. When Fourier transform of the field into frequency domain, we have: $\partial/\partial t = -i\omega$. Therefore, for a charge free and non-conductive dielectric medium ($\rho = 0$ and $\mathbf{j} = 0$), the frequency-domain wave equation is:

$$\nabla \times (\nabla \times \bar{\mathbf{E}}) - \frac{\omega^2}{c^2} \epsilon_r \bar{\mathbf{E}} = 0, \quad (2.5a)$$

$$\nabla \cdot (\epsilon_0 \epsilon_r \bar{\mathbf{E}}) = 0. \quad (2.5b)$$

where $c = \sqrt{1/(\mu_0\epsilon_0)}$ is the speed of the electromagnetic wave in vacuum.

An obvious solution of the wave equation is a monochromatic plane wave: $\mathbf{E}(\mathbf{r}, t) = \mathbf{E}_0 \exp[i(\mathbf{k} \cdot \mathbf{r} - \omega t)]$, where \mathbf{k} is the wave vector. By substituting the plane wave solution into equation 2.5, we get the dispersion relation condition for electromagnetic waves in a free-space medium of relative permittivity ϵ_r :

$$|\mathbf{k}| = \frac{\omega}{c} \sqrt{\epsilon_r} = \frac{\omega}{c} \mathbf{n}. \quad (2.6)$$

where \mathbf{n} is the complex refractive index of the medium. It is an important concept that is adopted to the waveguides' modes, for which the dispersion relation shows the propagation constant β , wave vector along the waveguide, as a function of frequency (more details in section 2.3).

Electric and magnetic power (P_e and P_m) can be calculated with Poynting's theorem as:

$$P_e + P_m = - \int_V (\mathbf{E} \cdot \frac{\partial \mathbf{D}}{\partial t} + \mathbf{H} \cdot \frac{\partial \mathbf{B}}{\partial t}) dV = \int_V \mathbf{j} \cdot \mathbf{E} dV + \oint_S (\mathbf{E} \times \mathbf{H}) \cdot \mathbf{n} dS. \quad (2.7)$$

where the first term on the right-hand side represents the resistive losses and the second term represents the radiative losses. The Poynting vector, which is defined as $\mathbf{S}(\mathbf{r}, t) = \mathbf{E}(\mathbf{r}, t) \times \mathbf{H}(\mathbf{r}, t)$, shows the direction of the radiation flow.

2.1.2 Scalar wave equation and the boundary conditions

The wave equation deduced above (equation 2.5) is true everywhere but is troublesome to solve if it is not solved with numerical methods using a computer. In the case of linear, homogeneous and isotropic medium, the susceptibility and permittivity are complex scalar numbers and each component of the field \mathbf{E} and \mathbf{H} just satisfies the simplified wave equation, i.e. the scalar wave equation shown below:

$$\nabla^2 \psi - \frac{\omega^2}{c^2} \psi = 0, \quad (2.8)$$

For a dielectric medium with step index profile, for example a step index fiber with a core of refractive index n_{co} surrounded by a cladding of n_{cl} , the

scalar wave equation 2.8 is valid within either the core or cladding but not on the core-cladding interface. At the interface of two homogeneous mediums, the fields follow the boundary conditions expressed mathematically as:

$$\mathbf{n}_2 \times (\mathbf{E}_1 - \mathbf{E}_2) = 0 \quad (2.9a)$$

$$\mathbf{n}_2 \cdot (\mathbf{D}_1 - \mathbf{D}_2) = \rho_s \quad (2.9b)$$

$$\mathbf{n}_2 \times (\mathbf{H}_1 - \mathbf{H}_2) = \mathbf{J}_s \quad (2.9c)$$

$$\mathbf{n}_2 \cdot (\mathbf{B}_1 - \mathbf{B}_2) = 0 \quad (2.9d)$$

where the subscript 1 and 2 denote the medium, respectively and \mathbf{n}_2 is the outward normal from medium 2. ρ_s and \mathbf{J}_s are surface charge density and surface current density, in the absence of which, the tangential component of the magnetic field \mathbf{H} and the normal component of the electric flux densities \mathbf{D} are continuous.

To have solutions everywhere for a dielectric medium with step index profile, we can impose the boundary conditions on the solutions of the scalar wave equation derived in each homogeneous region instead of solving the vector wave equation 2.5 everywhere.

For a simple case of two half-infinite homogeneous mediums in x - y plane, where the boundary is along y direction, applying boundary conditions to the plane wave solutions of two mediums shows that the tangential components of the wave vectors should be continuous: $\mathbf{k}_1^y = \mathbf{k}_2^y$. Therefore, the normal components of the wave vector in the second medium can be expressed as: $(\mathbf{k}_2^x)^2 = (\mathbf{k}_2)^2 - (\mathbf{k}_1^y)^2$. For example, when light is propagating from a medium of high refractive index n to air, we have the normal components of the wave vector in the second medium as:

$$(\mathbf{k}_2^x)^2 = \frac{w^2}{c^2} (1 - n^2 \sin^2 \theta_i) \quad (2.10)$$

where θ_i is the incident angle in medium 1. If $n^2 \sin^2 \theta_i > 1$, $(\mathbf{k}_2^x)^2$ will be negative and the normal components of the wave vector are pure imaginary, which means the transmitted light decays exponentially from the interface and the total internal reflection happens.

2.1.3 Scaling properties of the Maxwell equations

There is no fundamental length scale regarding electromagnetism in dielectric materials [14]. From the Maxwell wave equations, we see that for a solution, like a plane wave $\mathbf{E} = \mathbf{E}_0 e^{i\omega t - kx}$ with a set of parameters: wavelength λ , refractive index n of the material (real value) and the length scale x , there can be another solution with a set of parameters λ', n' for x' , which are related to the original set of parameters as:

$$\frac{nx}{\lambda} = \frac{n'x'}{\lambda'} \quad (2.11)$$

The scaling properties work as well for the harmonic modes of a waveguide in the following sections. For example, when the structure supports a mode with one wavelength, we can scale up the core of the structure with a factor of two so that it supports a mode for a doubled wavelength, which alternatively can also be achieved by multiplying the refractive index in the core of the structure and that of the surroundings by a factor of two. In practice, this simple fact makes all the designs of waveguides possible to scale.

2.2 Optical properties of matter

Light propagates in vacuum with a speed of c , while in a medium of index $n + i\alpha$ with a speed of c/n and a reduction of the intensity $I = I_0 \exp\{-\alpha z\}$ (no nonlinear effect is considered here). The optical properties of the medium can be physically expressed with its electric susceptibility as defined in equation 2.3, which is frequency dependent. A simple oscillator model is used for modeling the optical properties of insulators, which results in the dispersion of the refractive index of materials expressed by the Sellmeier formula[15]. Changing of the status of the medium due to the change of surrounding temperature leads to modified optical properties.

2.2.1 Sellmeier formula

The reaction of the bound electrons or the phonons of the lattice in a medium to electromagnetic waves is expressed with the polarization density P , which

can be modeled as harmonic oscillation driven by the electric field and described by the following equation:

$$\frac{\partial^2}{\partial t^2} \mathbf{P}(t) + \gamma \frac{\partial}{\partial t} \mathbf{P}(t) + w_{e/l}^2 \mathbf{P}(t) = \frac{Ne^2}{\mu} \mathbf{E}(t) \quad (2.12)$$

where γ is the damping rate, $w_{e/l}$ is the resonant frequency of electronic/vibrational dipoles, N is the number of atoms per unit volume, e is the magnitude of the electric charge of the electron, μ is the effective mass and E is the electric field of the light wave. The Fourier transform of equation 2.12 gives:

$$\bar{\mathbf{P}}(w) = \frac{Ne^2}{\mu} \frac{1}{w_{e/l}^2 - w^2 - iw\gamma} \bar{\mathbf{E}}(w) \quad (2.13)$$

which combined with equation 2.3, suggests that the complex susceptibility of a medium can be expressed with frequency as:

$$\chi_{e/l}(\omega) = \frac{Ne^2}{\epsilon_0 \mu} \frac{1}{w_{e/l}^2 - w^2 - iw\gamma} \quad (2.14)$$

Therefore, the complex permittivity of an insulator can be modeled as equation 2.15 for certain wavelength range, in which the second term represents the influence of the electronic resonance in the UV region and the third term the lattice vibrational resonance in the IR region.

$$\epsilon(\omega) = 1 + \chi_e(\omega) + \chi_l(\omega) \quad (2.15)$$

At wavelengths away from the resonances of the medium, the damping term can be negligible and the refractive index of a medium is expressed as the Sellmeier formula.

$$n^2(\omega) = 1 + \sum_i \frac{f_i}{w_i^2 - w^2}, \quad f_i = \frac{Ne^2}{\epsilon_0 \mu_i} \quad (2.16)$$

where $i = e, l$ would be enough for the dispersion of the refractive index of insulators from UV to IR region.

2.2.2 Thermo-optic coefficient

Optical properties of a medium are influenced by its environmental temperature. The variation of refractive index of a medium regarding the change of temperature can be described by the thermo-optic coefficient (TOC: dn/dT).

Studies have been done for optical solid materials, such as glasses [72, 73], which results in a model relating the TOC to the thermal expansion and the temperature dependence of the optical band gaps of the material.

Refractive index and its dispersion can be modeled with the electronic resonance in the UV region w_e and the lattice vibrational resonance in the IR region w_l as shown by equation 2.16 in the last section. The shift of the lattice vibrational resonance by temperature is considered negligible compared to the other effects for most of the optical glasses. Therefore, differentiating equation 2.16 with respect to temperature, T , gives:

$$2n \frac{dn}{dT} = \left(\frac{1}{w_e^2 - w^2} \right) \frac{d}{dT}(f_e) - \frac{f_e}{(w_e^2 - w^2)^2} \frac{d}{dT}(w_e^2), \quad f_e = \frac{Ne^2}{\epsilon_0 \mu_e}. \quad (2.17)$$

For f_e is inversely proportional to the volume of a material, $d(f_e)/dT$ is related to the thermal expansion of the material. Since most optical materials expand with increasing temperature, the first term of equation 2.17 contributes a negative thermo-optic coefficient. The second term depends on the thermal sensitivity of the band gaps of the materials, in which the excitonic band gap was claimed to have the dominant contribution to TOC. The excitonic band gap decreases with temperature, therefore, the second term contributes a positive thermo-optic coefficient. From equation 2.17, we can see that the thermo-optic coefficient is again a function of both frequency and temperature.

2.3 Modes in waveguides

Electromagnetic waves can propagate along waveguides, while they are confined to one or two dimensions. These particular solutions are the modes of the waveguides. For example, optical fibers have light confined in the transverse plane as fiber modes and propagating along the axial direction. Its working principle can simply be understood as following: waves reflected by the boundary of the waveguides interfere with the original waves and, depending on its geometry and index profile, waves of certain wavelengths have constructive interference resulting in spatially stable patterns in the waveguide. The modes are referred to as guided modes if the reflection on the boundary is complete and otherwise are called leaky modes.

In this section, I would first introduce the guided modes of a conventional step index fiber with basic concepts, for example, the effective RIs of the

propagating modes and their dispersion. Then, for band gap PCFs, the extended Bloch modes of the photonic crystal cladding are introduced. An analytical model, Birks's model, is introduced to calculate the photonic band gap (PBG) maps. Finally, the leaky core modes supported in the band gaps of a PCF are introduced as defect modes. Besides, I will introduce the reflection-based model developed in our group for analyzing the core modes of large core antiresonance fibers, which I used later, for the core modes with modified cladding structure and in a water-core photonic band gap fiber. We leave the numerical methods for the calculation of core modes to the next section.

2.3.1 Guided modes in a step index fiber

A step index fiber is characterized by its index profile, which has a core of the higher index and cladding of the lower index as sketched in the inset of figure 2.1. Such fiber supports discrete modes confined in its core by total internal reflection. The propagation of a mode is usually described by the component of wave vector in the longitudinal direction, i.e. the propagation constant: $\beta = k_0 \cdot n_{eff}$, where n_{eff} is defined as the effective refractive index of the mode. To analyze the guidance of a fiber, the propagation constants (or effective index) of different modes are solved.

In practice, the scaling properties of the electromagnetic wave suggest several normalized parameters to serve the calculation of the fiber modes. The common ones used in text books are U , V and W defined by the following equations:

$$U = \frac{2\pi R}{\lambda} \sqrt{n_{eff}^2 - n_{cl}^2} \quad (2.18a)$$

$$V = \frac{2\pi R}{\lambda} \sqrt{n_{co}^2 - n_{cl}^2} \quad (2.18b)$$

$$W = \sqrt{V^2 - U^2} \quad (2.18c)$$

where n_{co} and n_{cl} are the refractive index of the core and cladding respectively, R is the radius of the core. We can see that the parameters R and λ can be scaled up or down together and the solutions, U , V and W , will stay the same as long as we keep the ratio R/λ constant. Besides, by keeping the contrast of the refractive index constant, the refractive index of the core and cladding can also be scaled together without changing those normalized solutions.

Normally, the contrast of the refractive index for a step index fiber is defined by the index profile height:

$$\Delta = \frac{1}{2} \left(1 - \frac{n_{cl}^2}{n_{co}^2} \right). \quad (2.19)$$

For a specified step index fiber with fixed Δ , the homogeneous scalar wave equation for the field components within the cladding and core suggests solutions in the form of Bessel functions. By imposing boundary conditions to those solutions, we can have a characteristic equation for the fiber as shown below:

$$\left\{ \frac{J'_n(U)}{U J_n(U)} + \frac{K'_n(W)}{W K_n(W)} \right\} \left\{ \frac{J'_n(U)}{U J_n(U)} + \frac{n_{cl}^2}{n_{co}^2} \frac{K'_n(W)}{W K_n(W)} \right\} = \left(\frac{n\beta}{kn_{co}} \right)^2 \left(\frac{V}{UW} \right)^4, \quad (2.20)$$

where J , K are the Bessel functions and n is an integer showing the order of the solution.

From the characteristic equation, we can solve the normalized parameters and therefore the propagation constant of the fiber modes. In figure 2.1, we plot the solutions, U versus V , for a step index fiber of index profile height $\Delta = 0.2$. Discrete modes supported by fiber are labeled as TE_{nm} modes ($E_z = 0$), TM_{nm} modes ($H_z = 0$) and hybrid modes HE_{nm} and EH_{nm} ($E_z \neq 0$, $H_z \neq 0$), where two integers 'nm' shows that it's the m 's solution of the n ' order. For a particular fiber (n_{co} , n_{cl} and R are fixed), the plot shows the dependence of the normalized propagation constant on the frequency ($1/\lambda$), the dispersion of the modes. The dispersion of the modes cut off at $U = V$, where the effective refractive index equals the refractive index of the cladding ($\beta = k_0 \cdot n_{cl}$) and light leaks out to the cladding.

When the index contrast between the core and cladding is considerably small ($n_{co} \approx n_{cl}$ and $\Delta \ll 1$), the weakly guiding approximation is available for the waveguides and we can apply scalar wave equation everywhere. In this case, we have $n_{eff} \approx n_{co}$ meaning that the transverse component of the wave vector of the guided modes is much smaller than its longitudinal component β and the polarization influence of the index step at the boundary can be ignored. Applying the condition that the solution of the scalar wave equation and its first derivative are everywhere continuous at the boundary leads to the characteristic equation for this scalar case. In figure 2.2, the

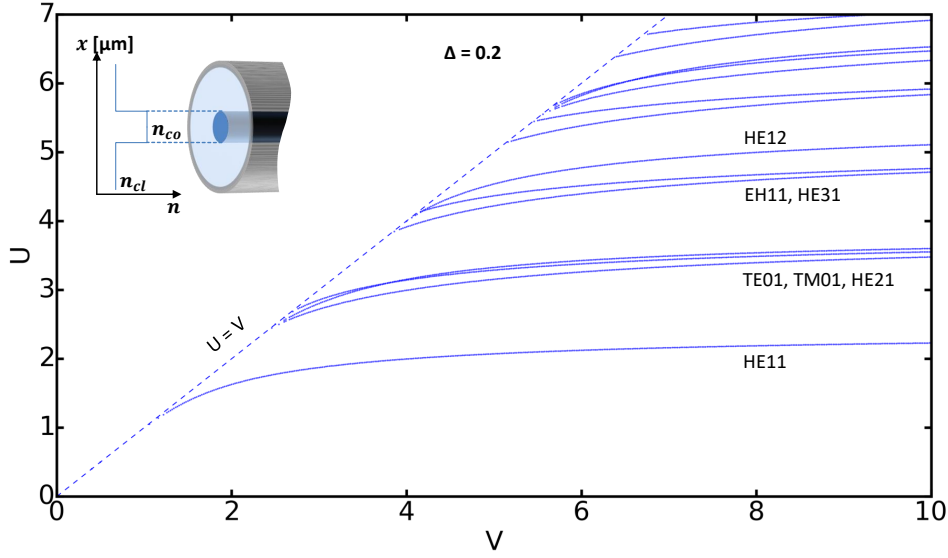


Fig. 2.1: Modes dispersion in a step index fiber (index profile height $\Delta = 0.2$) with normalized parameters U regarding V . Dashed line shows the cut off of the modes. Inset is a sketch of the step index fiber and its index profile.

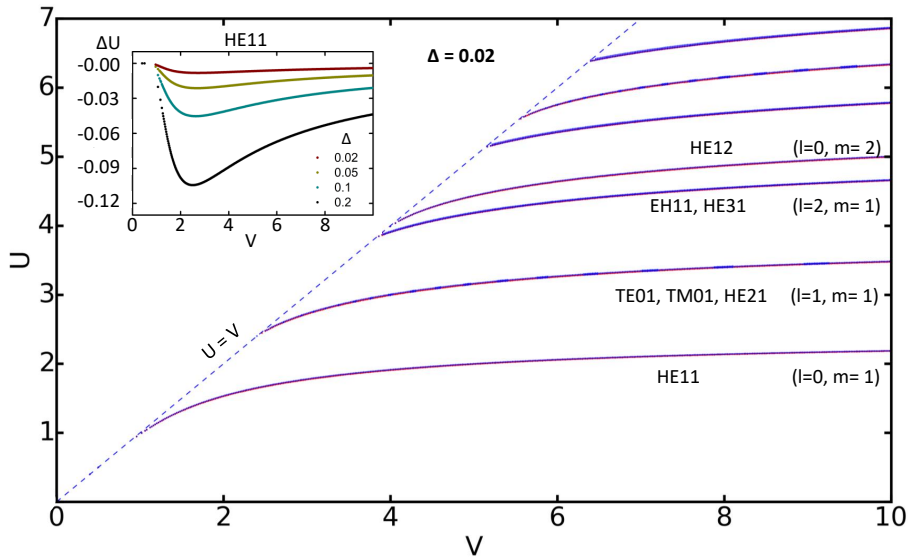


Fig. 2.2: Modes dispersion calculated with the weak guiding approximation (red line) compared with the exact solutions (blue line) for a step index fiber of index profile height $\Delta = 0.02$. Inset plots the difference between the solutions of the approximation method and the exact method for the fundamental mode HE_{11} with Δ of the values 0.02, 0.05, 0.1 and 0.2.

solutions calculated for the scalar case are plotted together with the solutions for the vector case for a fiber of $\Delta = 0.02$. We can see that in the case of low index profile height, higher order modes degenerate and the scalar solutions

(noted with the order l and the number of solutions m) can represent the degenerated modes quite well. The guided modes in this case are called linear polarized modes (LP modes), which have a large $\beta \approx k_0 n_{co}$ and approximated TEM field: $E_z \approx 0$ and $H_z \approx 0$.

The plot of the inset in figure 2.2 shows the difference of the approximated scalar solutions from the exact ones (ΔU) for the fundamental mode HE_{11} . We see that the difference decreases with the reduction of Δ value. Besides, for the same Δ , a smaller difference can be expected for a large V , which indicates that the weakly guiding approximation works better in case of a large R/λ . Therefore, a large core compared to the working wavelengths is a condition to use weakly guiding approximation in addition to the condition of a small index profile height for a fiber.

2.3.2 Bloch modes in photonic crystals

The photonic crystal cladding of a photonic band gap fiber consists of periodic arrays of high index strands in a low index matrix (figure 2.3(A)). Such photonic crystal, with index profile of discrete translational symmetry in the transverse plane, supports Bloch modes, which show continuous photonic bands and band gaps in spectra. The numerical methods to calculate Bloch modes and its band gaps will be introduced in the later section. Here, to have an insight into the formation of band and band gaps of Bloch modes, I will introduce a simplified model by Birks et. al., referred to as Birks' model in the thesis, to solve bands and band gaps of Bloch modes [74].

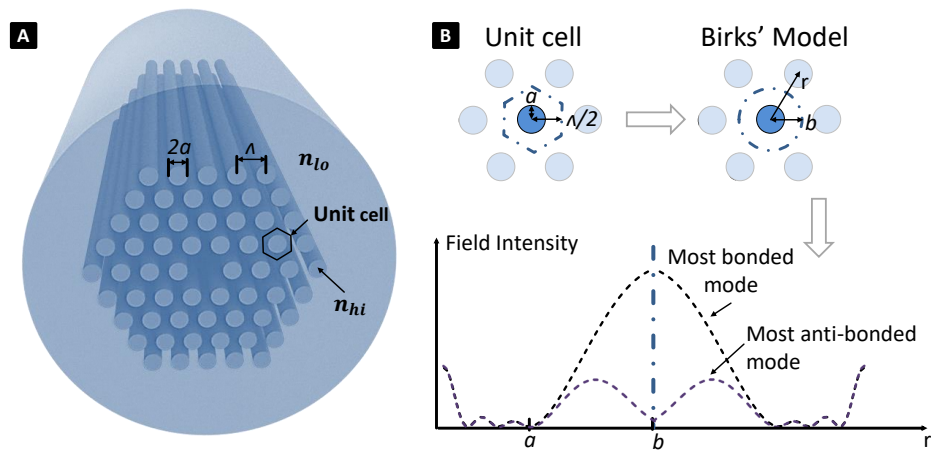


Fig. 2.3: Sketch of a photonic band gap fiber (A) and the basic concept of Birks' model (B). The plot is calculated based on the parameters in the literature [74] for two edge modes as an example.

In Birks' model, the photonic band gap cladding is defined by a hexagonal unit cell as sketched in figure 2.3(B). The unit cell has one high index strand in the center and periodic boundaries, including all the key parameters of the photonic crystal: the radius of the strands a , the distance between the neighboring strands Λ and the high and low index n_{hi} , n_{lo} . This unit cell is further approximated by a circular cell, whose radius is defined as $b = (\sqrt{3}/2\pi)^{1/2}\Lambda$ to preserve the area ratio of the strand in the unit cell. Besides, weakly guiding approximation is applied for low index contrast between n_{hi} and n_{lo} (or more precisely a large β resulting from a large a/λ and low index contrast as discussed in last section). Therefore, the analysis is simplified to a scalar problem separable in cylindrical coordinates.

The key idea for find the bands of Bloch modes is, drawn from the solid-state physics, that the top and bottom of a band are defined by the Bloch modes with the most bonding and the most anti-bonding character, respectively. In the case of a square lattice of strands, the top and bottom modes are those determined by two alternative boundary conditions at the periodic boundary of the unit cell: $\Psi(b) = 0$ defining modes with anti-mirror lines along the cell boundaries as the most anti-bonded modes; $\partial\Psi(b)/\partial r = 0$ defining modes with lines of mirror symmetry along the boundaries as the most bonded modes, where Ψ is the field and r is normal to the cell boundary. In the case of a hexagonal lattice, the nature of bonded and anti-bonded modes is not as clear leading to a more complex problem. Nevertheless, as shown below in figure 2.4, the application of these boundary conditions identified for the square lattice to the hexagonal unit cell still gives good approximation to the band structure[74].

Thus the top and bottom modes of the band are found by solving the scalar wave equation for the unit cell with two alternative boundary conditions. First, the general solutions of the fields in different regions of the circular unit cell corresponding to the LP_{lm} mode of the rod is assumed as

$$\Psi(r) = \begin{cases} J_l(Ur/a) & r \leq a \\ AK_l(Wr/a) + BI_l(Wr/a) & r > a, \beta - kn_{lo} > 0 \\ CJ_l(Qr/a) + DY_l(Qr/a) & r > a, \beta - kn_{lo} < 0 \\ E(r/a)^l + F(r/a)^{-l} & r > a, \beta - kn_{lo} = 0, l \neq 0 \\ G + H \ln r/a & r > a, \beta - kn_{lo} = 0, l = 0 \end{cases} \quad (2.21)$$

multiplied by any linear combination of $\cos(l\theta)$ and $\sin(l\theta)$. J_l , Y_l , I_l and K_l are Bessel functions, A to H are unknown constants and U , W and V are the waveguide parameters for the strands:

$$\begin{aligned} V^2 &= k^2 a^2 (n_{hi}^2 - n_{lo}^2) \\ W^2 &= a^2 (\beta^2 - k^2 n_{lo}^2) = -Q^2 \\ U^2 &= a^2 (k^2 n_{hi}^2 - \beta^2) = V^2 - W^2. \end{aligned}$$

Then, applying the continuity conditions for the fields on the material boundary $r = a$ (the same as for the weakly guiding step-index fiber) and the alternative boundary conditions on the periodic boundary $r = b$ gives characteristic equations for propagation constant β of the edge modes, which is written as:

$$g(V, W^2) = 0 \quad (2.22)$$

with separated cases for the top modes of a band

$$g_{top}(V, W^2) = \begin{cases} [AK'_l(\alpha W) + BI'_l(\alpha W)]W/U^l & W^2 > 0 \\ [CJ'_l(\alpha Q) + DY'_l(\alpha Q)]Q/U^l & W^2 < 0 \\ [E\alpha^l - F\alpha^{-l}]l/\alpha V^l & W^2 = 0, l \neq 0 \\ H/\alpha & W^2 = 0, l = 0 \end{cases} \quad (2.23)$$

and for the bottom modes of a band

$$g_{bottom}(V, W^2) = \begin{cases} [AK_l(\alpha W) + BI_l(\alpha W)]/U^l & W^2 > 0 \\ [CJ_l(\alpha Q) + DY_l(\alpha Q)]/U^l & W^2 < 0 \\ [E\alpha^l + F\alpha^{-l}]/V^{l-1} & W^2 = 0, l \neq 0 \\ G + H \ln / \alpha & W^2 = 0, l = 0 \end{cases} \quad (2.24)$$

where $\alpha = b/a$, J'_l is the derivative of J_l etc. The coefficients A to H are:

$$\begin{aligned} A &= WI_{l+1}(W)J_l(U) + UJ_{l+1}(U)I_l(W) & E &= VJ_{l-1}(V)/2l \\ B &= WK_{l+1}(W)J_l(U) - UJ_{l+1}(U)K_l(W) & F &= VJ_{l+1}(V)/2l \\ C &= [-QY_{l+1}(Q)J_l(U) + UJ_{l+1}(U)Y_l(Q)]\pi/2 & G &= J_0(V) \\ D &= [QJ_{l+1}(Q)J_l(U) - UJ_{l+1}(U)J_l(Q)]\pi/2 & H &= -VJ_1(V). \end{aligned}$$

Finally, using the characteristic equation given above, the effective index of the edge modes are solved by root searching methods with Python or Matlab. The particular form of equation 2.23 and 2.24 are chosen to give continuous and finite $g(V, W^2)$ for root searching algorithm. [74].

In figure 2.4 (A), I plot the bands of the Bloch modes from numerical simulation (green region) and band edge modes calculated from the Birks' model (blue and dark green squares) using the parameters of the photonic band gap cladding discussed in literature [74]. According to the scaling law (see section 2.1.3), the contraction or expansion of Λ , a and λ all together will not change the solution. Here, for fixed a/Λ and index profile, the band gap map is plotted for the coordinate axis of the normalized parameters $(n_{eff} - n_{lo})2\pi\Lambda/\lambda$ and $2\pi\Lambda/\lambda$.

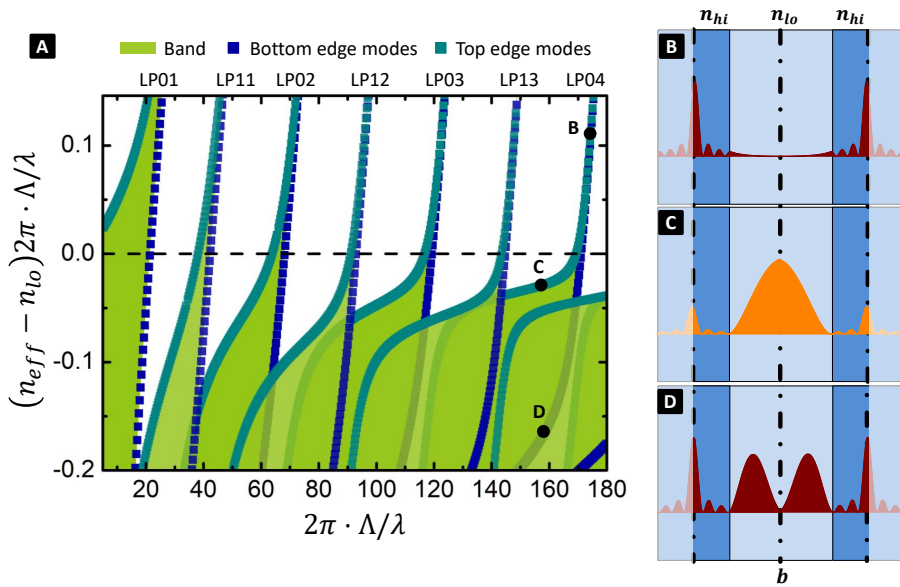


Fig. 2.4: (A) A band gap map with bands of the Bloch modes calculated from numerical simulation (green region) and band edge modes from the Birks' model (blue and dark green squares) for fixed a/Λ and index profile. The calculations were done using parameters of the photonic band gap structure discussed in the literature [74]. (B-D) Plots of the normalized radial intensity profiles for the LP_{04} band corresponding to the labels in (A): (B) a strands mode, (C) a top edge mode and (D) a bottom edge mode.

The zero-line in the band gap map indicates the cut-off for highly-confined modes in the strands ($n_{eff} = n_{lo}$). We can see that much above the zero-line, light is concentrated in the high index strands, corresponding to discrete dispersion lines in the map (figure 2.4(B)). They are simply the weakly-coupled LP_{lm} modes of the strands and have labels l and m defining the

azimuthal and radial variations respectively from the Birks' model. Birks' model allows us to track the dispersion of edge modes as they move below the zero-line, where they split and extend forming bands. This can be ascribed to the leak of light into the low index media and coupling between the strands modes in case of $n_{eff} < n_{lo}$. As we can see in figure 2.4(C-D), in this case the strands mode is no longer concentrated in the high index strands and has become hybridized with the modes in the low index regions between the strands. The hybridized modes of different intensity distributions have different effective indexes, which causes the splitting of the modes dispersion. In particular, the most bonded mode has a higher effective index as the top band edge and the most anti-bonded mode has the lower effective index as the bottom band edge.

Overall, the band gap map from the solutions of the edge modes based on Birks' model is consistent with that from the solutions of the Bloch bands using numerical methods, which will be introduced in the later section. Such band gap map shows the band gaps below the zero-line, in which the photonic band gap fiber offers guidance of the defect core modes.

2.3.3 Defect modes and the reflection model

The core of a photonic band gap fiber is formed by omitting one strand or several rings of the high index strands of the photonic crystal lattice, which is also referred to as a defect core. For example, the photonic band gap fiber shown in figure 2.3(A) has a core of index as the background, formed by omitting one high index strand. The modes confined in such defect core are called defect modes.

The confinement of the defect modes is a result of band gap guidance by the photonic crystal cladding. Band gap guidance is based on the optical properties of microstructured materials, which is principally different from the guidance with total internal reflection in a step index fiber or metallic reflection in a metal tube. Interference is essential for all effects in respect of band gap guidance. The reflection on the photonic band gap cladding can be understood as due to the constructive interference of the scattered light for certain wavelengths. Therefore, unlike guidance with total internal reflection, which works for particular frequencies depending only on the materials, the band gap guidance has working frequencies scaled with the geometry and periodicity of the microstructured materials. In another word, with photonic

band gap guidance, we can expect to change the guiding properties (shifting the band gaps) by scaling the geometry of the photonic crystal cladding instead of changing the composing materials.

The defect modes are characterized by the following facts: first, the effective refractive indexes of the modes are smaller than the refractive index of the defect core; second, the dispersion of the modes is limited to the band gap of the photonic band gap cladding; third, the dispersion of the modes anti-crosses with the bands of the cladding [71]. For a cladding of infinite photonic crystal, the loss of the defect modes, especially bend loss, is ascribed to the coupling of the core modes to the cladding modes, which can be related to the effective index mismatch between the defect modes and the nearest cladding modes [75]. In practice, the loss of the defect modes also subjects to the absorption of the core materials and the tunneling of the light through the finite extent of the photonic crystal cladding. A reduction of the loss can be realized by increasing the number of layers in the cladding of a photonic band gap fiber.

The calculation of the dispersion and loss of the defect modes relies normally on numerical simulations, like the multipole method or the finite element method, which we will discuss in the next section. Here, I would like to introduce a semi-analytical method based on the reflection model, which was proposed in our group for an antiresonant fiber[76]. This method allows considering the band gap guidance from the view of reflection of the light from the photonic crystal cladding offering new insights. Since the method separates the core modes from the cladding properties, it has the distinct advantage of avoiding the heavy numerical simulation for the full geometry and offering analytically calculation of the core modes for different core sizes. This method was applied in my work for analyzing the guidance properties of the defect modes in large-core photonic band gap fibers.

The basic idea of the reflection model is that the complex effective index of the guided modes in a comparably large core ($\lambda/R \ll 1$) can be calculated by inducing modifications to that of guided modes in a perfectly reflecting core. The modifications are determined by the phase shift and loss per reflection on the boundary, which can be approximated by the series expansions on the angle ϕ (small for the case of a large-core fiber). Figure 2.5 shows the parameters considered in the reflection model: the angle ϕ , the index n and the radius R of the core.

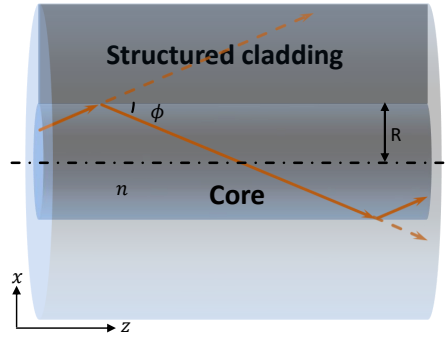


Fig. 2.5: Sketch for the reflection model with all the parameters. The orange lines refer to the waves zigzagging inside the waveguide core.

In the case of a perfectly reflecting cladding, the radial component of the wave vector for the modes guided in the core can be expressed as:

$$\kappa = \frac{j}{R}, \quad j = \begin{cases} j_{1,n} & TE_{0n}, TM_{0n} \\ j_{m-1,n} & HE_{mn} \\ j_{m+1,n} & EH_{mn} \end{cases}$$

where j_{mn} are Bessel zeros ($J_m(j_{mn}) = 0$). With wave number $k_0 = 2\pi/\lambda$, $k_{co} = k_0 n_{co}$, the propagation constant is found as $\beta^2 = k_{co}^2 - \kappa^2$, $\beta = n_{eff} k_0$. The real part of the effective index in a perfectly reflecting core can be approximated for the large core case as:

$$n_{eff}^o = n_{co} \left[1 - \frac{j^2}{2k_{co}^2 R^2} + O\left(\frac{1}{k_{co} R}\right)^4 \right]$$

For the case of band gap guidance with a photonic band gap fiber, we need to modify the solution of perfect reflected case shown above with additional terms regarding the loss and phase shift per reflection along the propagation.

First, with the assumption of small angle ϕ , the reflection coefficient at the interface of the core-cladding can be normally approximated with a quadratic equation:

$$r = -1 + q_1 \phi + q_2 \phi^2 + O(\phi^3), \quad (2.25)$$

with complex coefficients $q_1 = q'_1 + i q''_1$ and $q_2 = q'_2 + i q''_2$. Then, the loss per reflection is:

$$T = 1 - |r|^2 = C_1 \phi + C_2 \phi^2 + O(\phi^3), \quad C_1 = 2q'_1, C_2 = 2q'_2 - |q_1|^2,$$

and the phase shift per reflection is:

$$\Phi_{ref} = \arg(r) = D_1\phi + D_2\phi^2 + O(\phi^3), \quad D_1 = -q_1'', D_2 = -q_1'q_1'' - q_2''.$$

By expressing the angle ϕ and the distance between two reflections L as the following:

$$\begin{aligned} \phi &= \arcsin \frac{\kappa}{k_{co}} = \frac{\kappa}{k_{co}} + O\left(\frac{\kappa}{k_{co}}\right)^3 = \frac{j}{k_{co}R} + O\left(\frac{1}{k_{co}R}\right)^3, \\ L &= \frac{2\beta R}{\kappa} = \frac{2\beta R^2}{j} = \frac{2k_{co}R^2}{j}(1 + O\left(\frac{1}{k_{co}R}\right)^2), \end{aligned}$$

we have the loss coefficient α and the modification of the propagation constant $\Delta\beta$ for the non-perfect reflection case regarding the loss per reflection T and the phase shift Φ_{ref} respectively as following:

$$\begin{aligned} \alpha &= \frac{-\log_{10}(1-T)}{\log_{10}(e)L} \approx \frac{T}{L} = \frac{C_1j^2}{2k_{co}^2R^3} + \frac{C_2j^3}{2k_{co}^3R^4} + O\left(\frac{1}{k_{co}^4R^5}\right), \\ \Delta\beta &= \frac{\Phi_{ref}}{L} = \frac{D_1j^2}{2k_{co}^2R^3} + \frac{D_2j^3}{2k_{co}^3R^4} + O\left(\frac{1}{k_{co}^4R^5}\right). \end{aligned}$$

In the end, the real part and imaginary part of the effective indexes for the modes guided in a photonic band gap fiber can be approximated as:

$$n'_{eff} = n_{co}^o + \frac{\Delta\beta}{k_0} = n_{co} \left[1 - \frac{j^2}{2k_c^2R^2} + \frac{D_1j^2}{2k_c^3R^3} + O\left(\frac{1}{k_c^4R^4}\right) \right] \quad (2.26a)$$

$$n''_{eff} = \frac{\alpha}{2k_0} = n_{co} \left[\frac{C_1j^2}{4k_c^3R^3} + \frac{C_2j^3}{4k_c^4R^4} + O\left(\frac{1}{k_c^5R^5}\right) \right] \quad (2.26b)$$

In the results sections, we applied the method to photonic band gap fibers. We first built an approximated planar model for the cladding in COMSOL, which includes only a slice of the structured cladding. The planar model was analyzed numerically to get the reflection coefficients r regarding angles ϕ for TE and TM polarized waves. Then, the complex effective index of the modes guided by this structured cladding can be calculated according to equation 2.26, in which the complex parameters q_1 and q_2 were got by fitting equation 2.25. For the case of cladding with small index contrast, the difference of the reflections corresponding to different polarized waves can be ignored. In general case, we can use q_1^e, q_2^e or q_1^m, q_2^m for TE modes or TM modes, and the average values $(q_1^e + q_1^m)/2, (q_2^e + q_2^m)/2$ for hybrid modes respectively.

2.4 Numerical methods

For studying the Bloch states in a photonic crystal cladding as well as the guided modes in the core, numerical methods, like plain wave methods[77], multipole methods and finite element methods[71], can be used. Here, I would like to introduce finite element methods and multipole methods, which are practically used in my work. More details about simulations with these two methods are available in the book[71] as well as on the websites of the software (COMSOL and CUDOS MOF).

2.4.1 Finite element method

A space- and time- dependent physical problems can be modeled approximately based on discretization and solved numerically using the finite element method (FEM). It can be implemented conveniently with commercial software COMSOL. In our work, we have built two models to calculate the band gap maps of a photonic crystal cladding and guided modes in the defect core.

Modeling of Bloch modes

Bloch modes in a photonic crystal can be simulated with Bloch finite element methods[71].

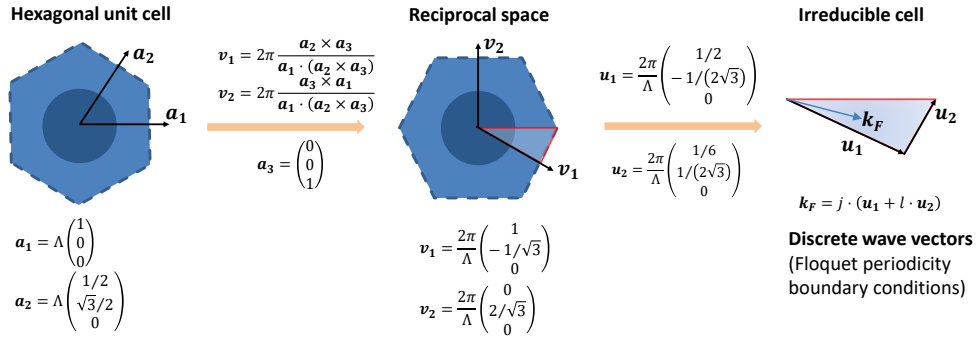


Fig. 2.6: Sketch for the calculation of discrete vectors \mathbf{k}_F for a hexagonal unit cell.

First, we build a model of the unit cell of photonic crystal using periodic boundaries and discrete vectors satisfying Floquet periodicity boundary conditions. The calculation of the discrete vectors for a hexagonal unit cell is shown in figure 2.6. The unit cell, defined by two vectors $\mathbf{a}_1, \mathbf{a}_2$, is first transformed to the reciprocal space giving a new pair of vectors $\mathbf{v}_1, \mathbf{v}_2$. In the reciprocal unit cell, we can then use vectors $\mathbf{u}_1, \mathbf{u}_2$ along the boundary of its

irreducible cell to define discrete vectors \mathbf{k}_F . Then, for unit cells defined by each discrete vector \mathbf{k}_F , we calculate the Bloch modes at different frequency. Finally, the mode solutions within a certain interval of the propagation constants are counted with different weighting coefficients corresponding to the discrete vectors giving the density of state (DOS) of the photonic crystal [78, 79]. The DOS map shows the bands and band gaps of a photonic crystal.

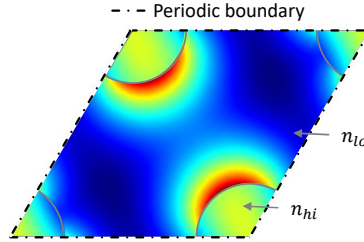


Fig. 2.7: An example solution (E-field norm) of the Bloch mode in a hexagonal photonic crystal shown with the unit cell built in COMSOL.

The calculation of DOS map, which is usually time consuming, can be done using commercial software COMSOL and COMSOL with Matlab. First, the unit cell model with periodic boundary conditions is built in COMSOL. Then by exporting the model to script in COMSOL with Matlab, the modal solutions for each discrete vectors are solved in the interesting frequency range (An example in figure 2.7). In the end, the post-process is done to count the modal solutions with a weighting filter for plotting the DOS map.

Modeling of defect modes

The core modes of a photonic crystal fiber are usually simulated by mode searching based on an initiative effective index. In the case of a photonic band gap fiber, the core modes exist only in the region of wavelengths in its band gaps. With a model of the transverse geometry surrounded by a perfect match layer as shown in figure 2.8(A), we start with one wavelength in a band gap and search for several modal solutions with a value close to the index of the core material as the initiative value of the effective index. To further calculate the dispersion of a mode, like for the fundamental mode, we can set the modal solution giving the fundamental one as the initiative value for the calculation at the next nearby wavelength and so on. This can be done within COMSOL, but to save some work, we can export the model as a script to COMSOL with Matlab and calculate dispersion of modes with

changing initial values.

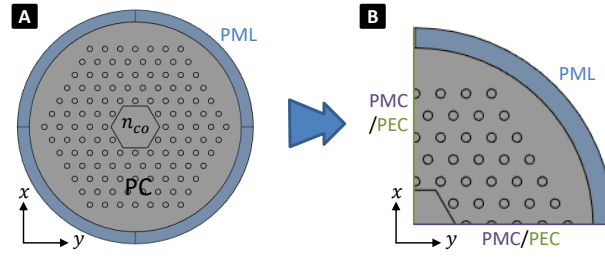


Fig. 2.8: An example model of a photonic crystal fiber in COMSOL for the calculation of defect modes. (A) shows the model with complete geometry and (B) the quarter-model.

The symmetry properties of geometry and modes can be used to save computational power. Especially in the case of large geometry dimensions, a model of only a quarter of the transverse geometry, instead of the complete geometry, of a photonic band gap fiber can be used for calculation (figure 2.8(B)). Moreover, it is convenient to trace the modal solutions with the boundary conditions in the quarter-model. In the case of HE modes, the boundaries along x and y should be set to one perfect magnetic conductor (PMC) and one perfect electric conductor (PEC), while in the case of TE modes or TM modes, the boundaries along x and y should be set to both PEC or both PMC respectively. For the order of modes, we can count the zero nodes of the fields along the radial direction for determination. All these were implemented with a model in COMSOL with Matlab.

2.4.2 Multipole method

Based on the multipole formulations for multicore conventional fibers, the multipole method to treat microstructured fibers was developed by the university of Sydney [80, 81]. The method can be used to deal with PCFs, which have a solid-core/air-core surrounded by solid cylinders or air holes, and yields the complex propagation constants of the modes in the PCFs. It makes use of the circularity of the structures and has been adapted to take into account the symmetry properties of the modes, offering high computational efficiency for microstructured fibers.

To enable the general implementation of the multipole method for simulating photonic crystal fibers, a software package, CUDOS MOF Utilities, is designed by the university of Sydney and free for downloading. We have used it for finding modes of light cage structures and computing their dispersion

curves.

To find modes of a photonic crystal fiber with CUDOS MOF Utilities, we start with defining the structure parameters and physical parameters in the parameter file (labeled in figure 2.9). There are also parameters relating to the algorithm, most of which are internal parameters with default values, which will be adjusted automatically during the calculation or can also be specified to suit special cases. Then, by running the executable file, 'fiber.exe', we can solve the modes for the set of parameters. A bunch of new files containing the report on the simulation process and the results will be generated in the local folder. The .fbb and .bcf files contain the Fourier Bessel coefficients of the modes, which can be read by the executable file: winfield.exe. Figure 2.9 shows an example of a fundamental mode with winfield.exe. On the panel of the winfield.exe, we can read the corresponding input physical parameter wavelength as well as the output complex effective index. The window next to the panel shows the structure for the calculation and the distribution of field profile (the figure shows the z component of the Poynting vector here).

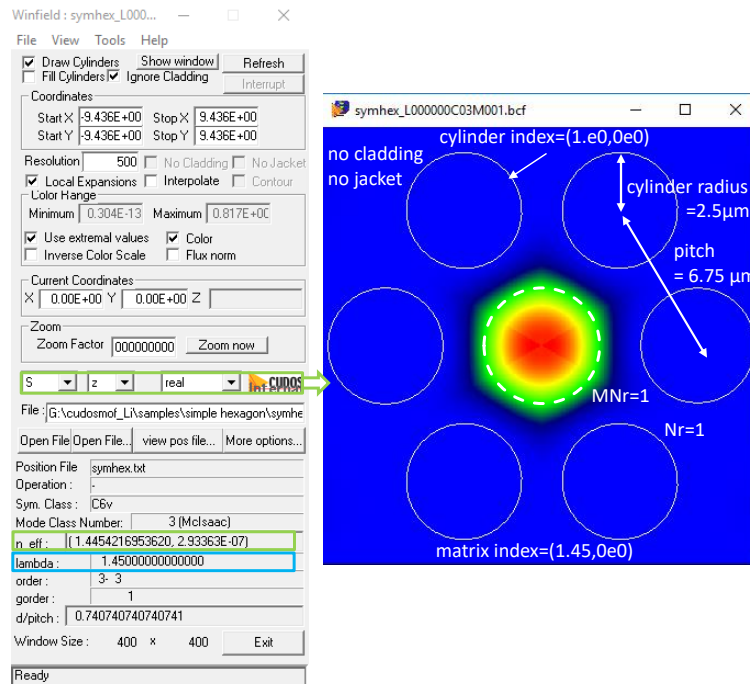


Fig. 2.9: An example shows a fundamental mode found by CUDOS MOF Utilities for a structure with solid core surrounded by a ring of air holes. The key parameters to be defined are labeled in the modal plot and highlight with blue square on the panel of Winfield. The green square highlighted the the effective index of the mode and the field component plotted.

The dispersion of a mode can be calculated with CUDOS MOF Utilities conveniently. We can simply set the physical parameter wavelength as a range with initial wavelength (keyword: `start_lambda`), final wavelength (keyword: `stop_lambda`) and the number of points in between in the parameter file. Alternatively, it can also be done by loading the known solution (`.fbb` or `.bcf` file) into a new parameter file and setting the initial wavelength as the wavelength for the known solution, then only define the final wavelength and the number of points in between. Additionally, by loading the known dispersion file (`.dat`) in the parameter file, we can extend the known dispersion to a further wavelength defined as final wavelength.

The Multipole method works efficiently for standard photonic crystal structures, like solid core photonic crystal fiber, especially with the knowledge of the range of their band gaps. However, for novel designs, additional efforts for searching the modes, like increasing the points for scanning, are unavoidable.

Results: Models to investigate light guidance with microstructured cladding

Instead of total internal reflection in conventional fibers, a microstructured fiber, which has a core of lower index materials, confines light by forbidding propagation of light in the microstructured cladding with photonic band gap, inhibited coupling or anti-resonance. Here, we developed models for both cladding modes and core modes to investigate the guidance with microstructured cladding.

In this section, we first introduce a completely analytical method based on Birks' model[74] to calculate the photonic band gap maps of the cladding. It enables us to identify the photonic band gaps straightforwardly from analytical expression and investigate the key parameters affecting the photonic band gaps. Then, for the core modes, we apply the reflection model that relates the reflection and transmission properties of a microstructured cladding to the real and imaginary part of the refractive index of the core modes. It offers a new insight into the guidance with microstructured claddings and is used as an efficient way to optimize the structure to achieve lower loss.

3.1 Photonic band gap maps

To analyze the guidance of a photonic band gap cladding, we need to calculate the band gap map of the cladding modes. A band gap map shows the parameter combinations, like effective indexes of modes and frequencies, that correspond to bands of the cladding modes and to band gaps for guidance by such cladding. Band gap maps are affected by parameters such as the material index contrasts and geometry parameters of the photonic band gap cladding.

In this section, I would like to introduce a completely analytical method using binary functions developed from the Birks' model [74]. It allows us to identify band gap regions straightforwardly from simple calculations with key parameters including effective index (n_{eff}), frequency (ω), material indexes

(n_{hi}, n_{lo}) and geometry parameters (radius of the strands a , distance between neighboring strands Λ) of the microstructured cladding.

3.1.1 Model for calculating band gap maps with binary functions

One effective simulation method for the band gap map of a photonic crystal cladding is Birks' model [74]. As described in the theory part, Birks' model has two characteristic equations from two particular periodic boundary conditions to calculate the top and bottom band gap edge modes. However, it is only semi-analytic since solving the characteristic equations for the top and bottom band gap edge modes still requires numerical root searching methods. To solve the problem completely analytically, our work [82] proposed a binary function from the two characteristic functions.

The main idea of the binary function has been illustrated in figure 3.1. As we can see that the band region (the yellow-green region) is between the zeros of the top and bottom characteristic functions (solutions for the top and bottom edge modes), where the two characteristic functions change their signs. This fact results in that: within the band region, the two characteristic functions always possess opposite signs, whereas in the band gap region (white region) both functions exhibit the same sign. Therefore, instead of searching for zeros of the characteristic functions for the edge modes, we can define the band regions by the opposite signs of the two characteristic functions.

Since the actual value of the functions is irrelevant, we constructed a normalized binary function, which results in 0 or 1 depending on the sign of the product of the two characteristic functions, as shown in equation (3.1):

$$f_{bool} = \frac{1}{2} \left(1 - \frac{f_T \cdot f_B}{|f_T| \cdot |f_B|} \right) \quad (3.1)$$

where f_T and f_B are the characteristic functions for top and bottom edge modes (the left side of the equation (2.22)). Because only the sign of the functions matters, we can leave the factors in the equations, which were just used to have continuous values of the functions when roots searching is

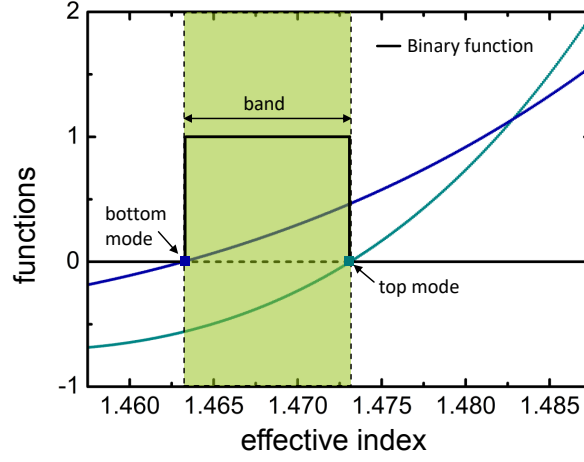


Fig. 3.1: The example plots of the characteristic functions (the blue and blue-green lines) based on the Birks' model and our binary function (black line). The square dots show the solutions of the corresponding characteristic equations. The yellow-green region indicates the region of effective index for a band.

conducted. As an example, for the interesting region below the index of the cladding ($W^2 < 0$), we have the two characteristic functions as,

$$\begin{aligned} f_T &= C J'_l(\alpha Q) + D Y'_l(\alpha Q), \\ f_B &= C J_l(\alpha Q) + D Y_l(\alpha Q). \end{aligned}$$

with $\alpha = b/a$ (a is the radius of the strands in cladding and b is the radius of the circular unit cell). The coefficients C to D are defined as:

$$\begin{aligned} C &= [-Q Y_{l+1}(Q) J_l(U) + U J_{l+1}(U) Y_l(Q)], \\ D &= [Q J_{l+1}(Q) J_l(U) - U J_{l+1}(U) J_l(Q)]. \end{aligned}$$

With equation (3.1), a band gap map of any Bessel function order can be straightforwardly calculated by $f_{bool} = 0$ for the band gaps and $f_{bool} = 1$ for the bands. When Bessel function orders from 0 to l_{max} (the maximum Bessel function order) are considered, for a full band gap map, we should sum all the binary functions as shown in equation (3.2). Ultimately, the band gaps are the region of $f_{bool}^{full} = 0$.

$$f_{bool}^{full} = \begin{cases} 0 & \text{if } \sum_{l=0}^{l_{max}} f_{bool} = 0 \\ 1 & \text{if } \sum_{l=0}^{l_{max}} f_{bool} \neq 0 \end{cases} \quad (3.2)$$

To verify the validity of this method, for a band gap fiber of parameters identical to those used in the original work of Birks et al.[74], the bands region identified with our binary function are plotted together with the dispersion of the edge modes, which are calculated by the root searching algorithm, in figure 3.2.

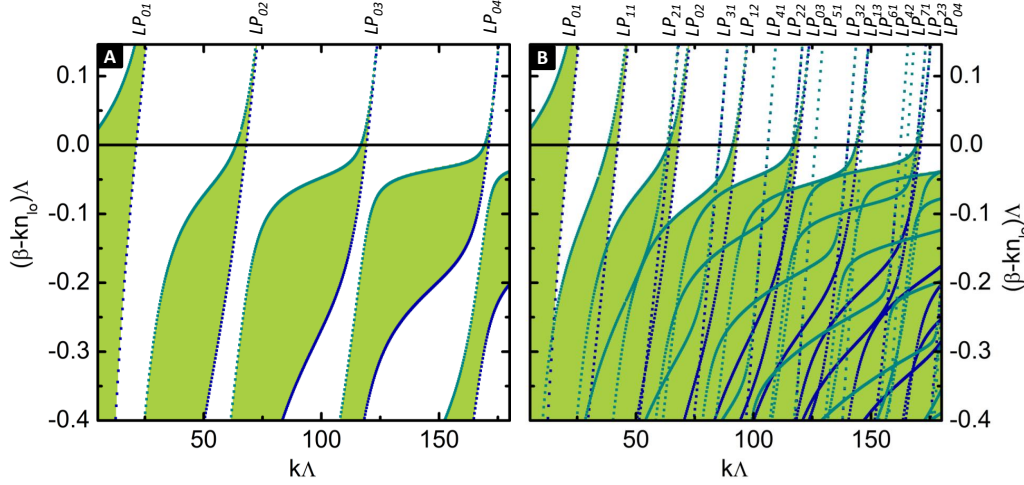


Fig. 3.2: Dispersion of the normalized effective index of the cladding modes for a band gap fiber are plotted with two methods based on Birks' model: the dots show the roots of the top and bottom edge modes characteristic equations, while the green and white region are given by the value of the binary function. This calculation was done for the parameters used in the original work of Birks et al: $n_{lo} = 1.458$, $n_{hi} = 1.48716$ and $d/\Lambda = 0.41$ [74]. (A) Dispersion of the lowest Bessel function order ($l = 0$). (B) Full dispersion map by summing the results of the first seven orders ($l = 0...7$).

We started by considering the lowest Bessel function order $l = 0$ (figure 3.2(A)). We can see that two simulations gave the same results: the band regions indicated by the green regions given by the non-zeros of the analytical binary functions have edges consistent with the band edge modes indicated by dots calculated from the numerical root-searching for the two characteristic equations. The mechanism of our binary function is always tenable for the fact that the dispersion of the adjacent top and bottom edge modes of the same Bessel function order never cross. As we observed above the zero line ($n_{eff} = n_{lo}$), the adjacent top and bottom edge modes of the same Bessel function order couple and thus anti-cross with each other.

More Bessel function orders need to be considered for a full band gap map.

The maximum Bessel function order can be estimated with the expression for the guided modes in a multimode fiber: $l_{max} = \text{ceiling}(2V/\pi)$, where the $V = 2\pi \cdot R\sqrt{n_{co}^2 - n_{cl}^2}/\lambda$ is the waveguide parameter ($\text{ceiling}(x)$ gives the least integer greater than or equal to x) [83]. In figure 3.2(B), the sum of the first seven orders is presented. We can see that different evolution of the higher order bands leads to a significant reduction of the band gaps after overlapping the first seven dispersion maps, particularly at large frequencies. Moreover, we observed that the broadening of the bands (consequently the narrowing of the band gaps) just below the zero line is mainly determined by the maps of the first few Bessel function orders and will not be affected by the maps of even higher Bessel function orders ($l > 7$).

Using our binary function without root searching, the calculation process is completely analytical and straightforward. As the dispersion function f_T and f_B constructing the binary function contain all key parameters, we can use the binary analytical function to play with all these parameters for design.

To demonstrate the design capability of the binary function, the band gap maps were calculated with binary functions regarding geometry parameters, pitch Λ and strand diameter d , as shown in figure 3.3. We used the same refractive indices of the materials as in figure 3.2 and assumed a fixed effective index ($n_{eff} = 1.4561$) for a wavelength ($\lambda = 1\mu\text{m}$). Considering the feasibility from the perspective of fabrication, the parameter combinations not realistic to use are indicated by gray region.

The resulting band gap map has band gaps indicated by zeros (white regions in figure 3.3) and cladding modes by non-zeros (green regions in figure 3.3). The results by overlaying the maps of the first two lowest Bessel function orders show already the likely domains for the band gaps, pure white areas in figure 3.3(A). Overlaying the first ten maps reveals more features to the band gaps (figure 3.3(B)). The parameter combinations in the band gaps indicate the configurations of the photonic crystal cladding, which can offer the photonic band gap guidance in the defect core. An example of the guided core mode is plotted in the inset of figure 3.3(B), which was calculated with Multipole method (CUDOS MOF) for the configuration indicated by the red dot in the figure.

For applications in certain effective index regime with a predefined wavelength, it is helpful to have a band gap map regarding geometry parameters of the cladding for a fixed value of effective index of the guided mode (usually

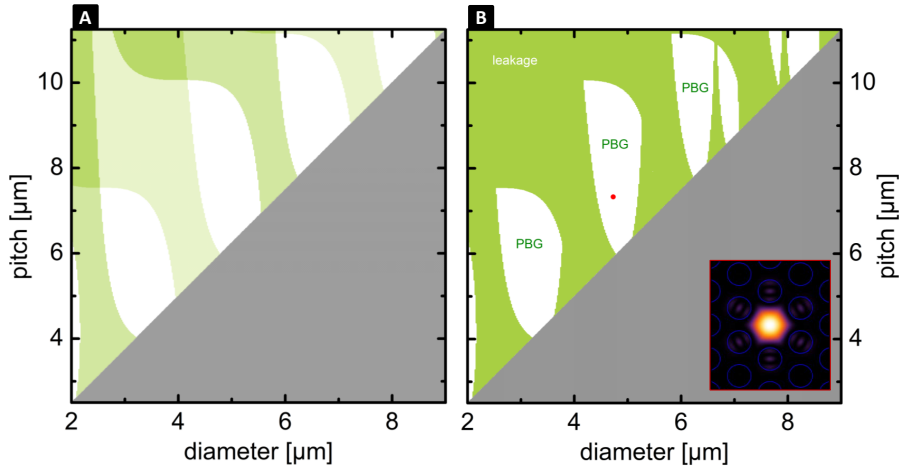


Fig. 3.3: Photonic band gap maps calculated with binary functions regarding geometry parameters: pitch Λ and strand diameter d . The calculation was done for a fixed effective index ($n_{eff} = 1.4561$) and wavelength ($\lambda = 1 \mu\text{m}$). The material parameters used are the same as the example in figure 3.2 ($n_{lo} = 1.458$, $n_{hi} = 1.48716$). In both plots, the gray regions correspond to the ratio of the diameter to pitch, which is unrealistic from the fiber fabrication perspective. The white domains refer to the band gaps. (A) Plot of the overlay of the maps of the first two Bessel function orders ($l = 0$ and $l = 1$). (B) Complete map by summation of the first ten orders ($l = 0 \dots 10$). The inset shows the guided fundamental mode corresponding to the parameters indicated by the red dot in the band gap ($\Lambda = 7.33 \mu\text{m}$, $d = 4.7277 \mu\text{m}$).

assumed slightly below the index of the core material for the fundamental mode). The band gap map versus geometry parameters is also a particular key to see the susceptibility of the individual guidance to the inevitable geometry deviations induced from the fabrication process. For instance, the guided mode shown by the inset in figure 3.3(B), from the location of the corresponding parameters in the band gap, we see a better tolerance of the guidance to deviations in pitch than to deviations in strand diameter. From the shape of the corresponding band gap, we see the corresponding band gap showing an average tolerable deviation of around 20% in pitch, whereas around 10% in diameter (assuming the guidance with parameters in the middle of this band gap). Thus, the band gap map plotted with our binary function method regarding geometry parameters can be used for the evaluation of the photonic band gap fiber in terms of robustness against structural imperfections.

3.1.2 Parameter effects on band gaps

Here, we studied the affection of key parameters on band gap maps using binary functions. The binary function introduced above is based on Birks' model, which relies on assumptions, i.e. a small index contrast (or a large ratio of strand dimension to wavelength as discussed in section 2.3.1) and a small ratio of diameter to pitch, d/Λ [74]. To keep these assumptions, we apply only small variations on the parameters to get a clear picture of their influence on band gaps.

There are several key parameters for band gap guidance with photonic crystals: diameter of the strands d , distance between neighboring strands pitch Λ , frequency w (or wavelength λ) and indices n_{hi}, n_{lo} composing the cladding. Considering the scaling properties of the electromagnetic waves, we will plot band gap maps for fixed index contrasts and ratios of strands diameter to pitch (as shown in figure 3.2(B) and popularly used in other literatures).

The simulation of the band gap map regarding $(\beta - kn_{lo})\Lambda$ and $k\Lambda$ (figure 3.2(B)) shows that the first band gap along frequency, which is also defined as fundamental band gap, goes deeper below the zero line ($n_{eff} = n_{lo}$) than the following band gaps. Moreover, it is observed that the fundamental band gap is basically formed from the results of the first two Bessel function orders ($l = 0$ and $l = 1$). Therefore, we focused our investigation on the fundamental band gap from the calculation with the first two Bessel function orders.

Given the above, we plotted the band gap maps of the first two Bessel function orders ($l = 0$ and $l = 1$) regarding $(\beta - kn_{lo})\Lambda$ and $k\Lambda$ for the region of the fundamental band gap. We started using the parameters same as those in the previous example (figure 3.2). Then, further small variations were made by the ratio of strands diameter to pitch d/Λ and the high index of photonic cladding n_{hi} (keeping $n_{lo} = n_{silica}$) respectively. Each calculation using the self-written python code of our binary function takes only a few minutes. The results are shown in figure 3.4 and figure 3.5.

We can see that as we increase d/Λ by 0.01 and 0.04, the bands shift to smaller frequencies while the band gap extends towards smaller effective index (figure 3.4). For the same pitch, as we increase the ratio of strand to pitch, it equals increasing the diameter of strand. For a larger strand diameter, the same guided mode in the strand works at a longer wavelength (smaller

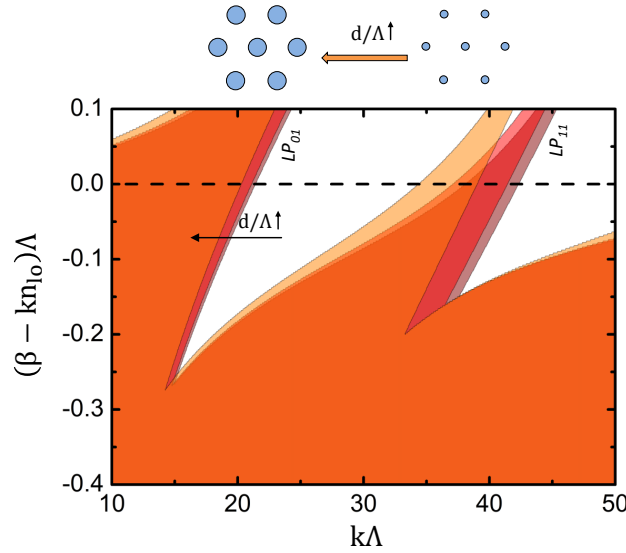


Fig. 3.4: Band gap maps with varying d/Λ for the first two Bessel function orders: $l = 0$ and $l = 1$ and the region of the fundamental band gap. The color regions refer to the bands of the cladding modes, whereas the white regions refer to the band gaps. The maps of bands in color of wine, red and orange correspond to the calculation with ratio of strand diameter to pitch d/Λ as 0.41, 0.42 and 0.45 respectively. The material parameters used are the same as the example in figure 3.2 ($n_{lo} = 1.458$, $n_{hi} = 1.48716$).

frequency). This scaling property of the electromagnetic wave is the reason for the obvious shift of modes above the zero line, where most of the light is in the strands. The growth of the band gap ascribes to the different scale of shift regarding the top and bottom edge modes due to their different relative concentrations of power in the various materials. The bottom edge modes of the first order band ($l = 0$) shift a bit more than the top edge modes of the second order band ($l = 1$). Therefore, the band gap extends and goes a bit deeper to smaller effective index.

As we increase the index of the strands in the photonic crystal cladding n_{hi} by $dn = [0, 0.001, 0.003]$ (increasing the index contrast), we also observed a shift of the band to smaller frequencies and a bit growth of the band gap towards smaller effective index (figure 3.5). The shift of the modes above the zero line as well as the extended band gaps below the zero line can be explained again by the scaling properties of the electromagnetic waves: as we increase the index of the strands, the same mode works at a longer wavelength (smaller frequency). In this case, the bottom edge modes of the first order band ($l = 0$) shift still a bit more than the top edge modes of the

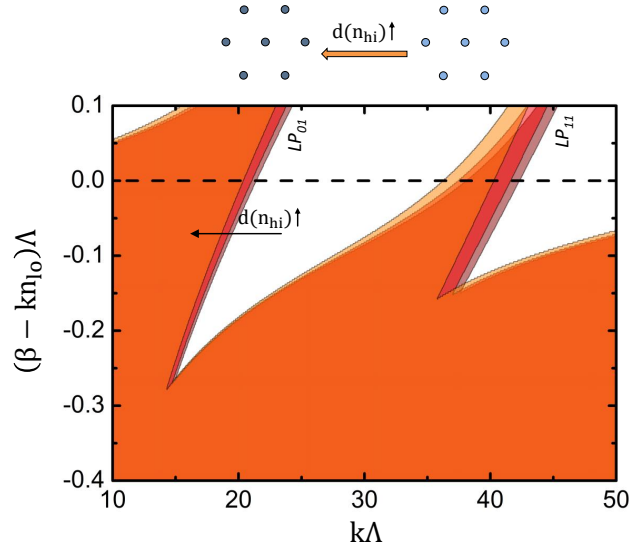


Fig. 3.5: Band gap maps with varying n_{hi} for the first two Bessel function orders: $l = 0$ and $l = 1$ and for the region of the fundamental band gap. The color regions correspond to the bands of the cladding modes, whereas the white regions refer to the band gaps. The maps of bands in color of dark red, red and orange correspond to the calculation with high index $n_{hi} = 1.48716$ varied by $dn = [0, 0.001, 0.003]$ respectively. This calculation was done for a fixed background index ($n_{lo} = 1.458$) and geometry parameters ($d/\Lambda = 4.1$) the same as the example in figure 3.2.

second order band ($l = 1$), leading to the growth of the band gap into smaller effective index.

Despite the different parameters we modified above, both of the cases show a growth of the fundamental band gap towards smaller effective index due to a different scale of shift regarding the bottom edge modes of the first order band ($l = 0$) and top edge modes of the second order band ($l = 1$). To figure out what is the reason for this different scale of shift between the bottom and top edge modes, we extracted the data from the band gap map (the one with $d/\Lambda = 0.45$ in figure 3.4) to plot the field profile in Birks' model using equation (2.21) for a bottom edge mode of the first order ($l = 0$) and a top edge modes of the second order ($l = 1$).

In figure 3.6(B) and (C), we showed two modal profiles based on the Birks' model, which are approximated in one dimension and in a region consisting of two neighboring strands. The different scales of shift between the bottom edge modes of the first order band ($l = 0$) and top edge modes of the second order band ($l = 1$) can be explained by their different field distributions in the structure. The bottom edge mode of first Bessel order (figure 3.6 (B)) has

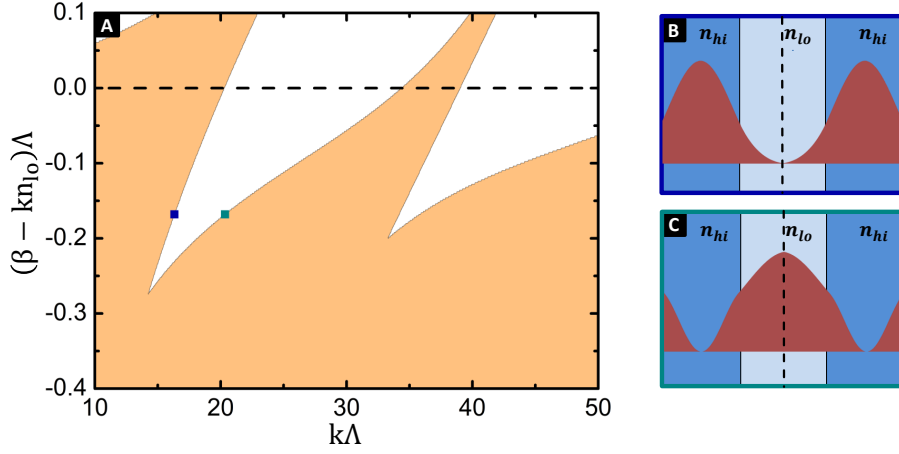


Fig. 3.6: (A) Band gap map for the first two Bessel function orders: $l = 0$ and $l = 1$ with material parameters: $n_{lo} = 1.458$, $n_{hi} = 1.48716$ and geometry parameters $d/\Lambda = 0.45$. The color regions correspond to the bands of the cladding modes, whereas the white regions refer to the band gaps. (B) and (C) show two modal profiles of intensity (dark red) corresponding to the parameters labeled by the square dots in (A). Two neighboring strands (blue region) are shown here with the dash line in the center indicating the periodic boundary in the Birks' model.

light concentrated in the high index strands with a minimum at the periodic boundary (dashed line). Its dispersion follows the dispersion of the strand modes even below the zero line. The top edge mode of the second Bessel order (figure 3.6 (C)) has a dominating amount of light located in the low index region between strands with a maximum at the periodic boundary (dashed line). Its dispersion below the zero line bends from strand modes due to the increasing light distribution in the low index region between the strands. When we increase the ratio of the strand's diameter to pitch or the high index, we increase the product of the refractive index and the geometry length ($n \cdot x$) in the strands part relative to the unit cell (if we reduce the n_{lo} , we still have increased $n \cdot x$ relatively for the strands). With this change, the modes distribution tends to locate more in the strands but with different degrees for the one of most of the light in strands and the one of most of the light in between the strands. This explains the different shifting behavior of the top and bottom edge modes dispersion that we observed above.

3.2 Reflection from a microstructured cladding

In principle, regardless of the cladding structures, the guidance of a low-index core microstructured fiber can be attributed to destructive interference in the cladding, leading to high reflection. The core modes exist when the phase change across the core plus the phase change induced by the reflection from the cladding produces constructive interference as indicated in the work for 2D planar photonic crystal waveguides [84, 85]. A reflection-based method was also applied on circular waveguides with an approximated planar model as shown in the work by Zeisberger on the analytic expression for an anti-resonant fiber [76]. In the case of a core large enough compared with wavelength, an approximated planar model consisting of a small part of the cladding, where the curvature can be neglected and the field can be locally approximated as a single plane wave, was used to analyze the reflection from the cladding. These previous works show that the dispersion and loss of the core modes can be obtained analytically from the complex reflection coefficient in the planar model (details introduced in theory section 2.3.3). Analyzing the reflection from the interface between structured cladding and homogeneous core is much simpler than studying the entire fiber cross section, offering a straightforward way to optimize the cladding structure of a microstructured fiber for better guidance.

In this section, we explored analyzing the guidance in an all-solid single-ring microstructured fiber with a reflection-based planar model. We started with showing the transmission properties of the cladding for the fundamental modes in the first four transmission windows of the fiber. Then, we calculated the mode dispersion and loss from the complex reflection coefficient and compared them with the results from the numerical mode calculation. In addition, by doing intensive parameters sweep for the geometry of the cladding, we found interesting features to have extraordinary low loss.

3.2.1 Reflection-based model for calculation of core modes

The all-solid single-ring microstructured fiber, which has a large core surrounded by circularly arranged strands of a higher refractive index ($\Delta n =$

0.02, for practically doped silica) as shown in figure 3.7(A), was modeled here. This geometry was deliberately chosen to resemble the commonly considered situation of a low-index core band gap fiber, which for lower loss and delivering of higher power has a large core, consisting of GeO_2 -doped strands located in a silica background [86]. The particular choice was made to present the model in an illustrative way.

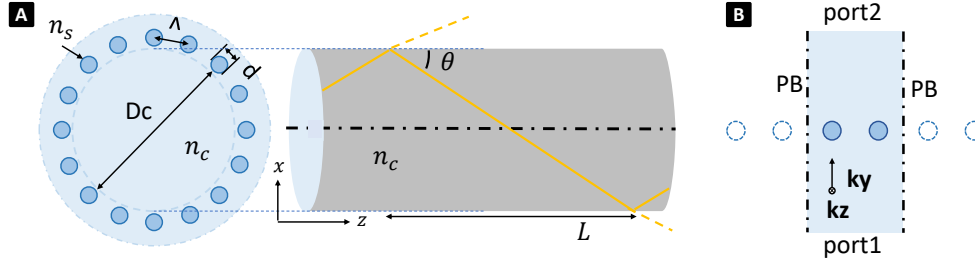


Fig. 3.7: (A) Sketch of a single-ring microstructured fiber and the concept of the reflection model. n_c and n_s are refractive indexes of core material and cylinder material respectively. L is the longitudinal distance between two neighbouring reflections. (B) The corresponding approximated planar model.

In the case of a cylindrical core surrounded by a perfectly reflecting core-cladding interface, the constructive interference as guided modes in the core has Bessel form solutions. The phase of light accumulated from propagating across the core should be given by the roots of the Bessel function: $\kappa \cdot R = j_{lm}$, where κ is the transverse component of the wavevector in the core and j_{lm} represents the m -th root of the Bessel function J_l and R the core radius. Here, we focus our analysis on the fundamental mode, whose transverse component of the wave vector can be analytically expressed as:

$$\kappa = \frac{j_{01}}{R} \quad (3.3)$$

where j_{01} is the first root of the zero-order Bessel function.

For the sake of simplicity, we consider the guidance of the light in a large core fiber as light rays getting reflected and transmitted at an approximated planar boundary of the cladding. The angle θ and the longitudinal length between two reflection L in Fig.1 can be expressed as:

$$\theta = \arcsin \frac{\kappa}{k} \approx \frac{\kappa}{k} = \frac{j_{01}}{kR}, \quad L = \frac{2R}{\tan(\theta)} \approx \frac{2R}{\theta}. \quad (3.4)$$

with wave vector $k = k_0 n_c$, n_c is core index. The approximation here is valid for the case of the propagation constant $\beta \gg \kappa$, a rather small angle θ , which is true for a large core fiber especially for the low-order modes.

The corresponding approximated planar model, as shown in figure 3.7(B), comprises the single-ring microstructured cladding to two cylinders using periodic boundary conditions. Two ports were set to model the reflection and transmission properties of the cladding. For a single-ring microstructured fiber with a set of parameters: number of cylinders $N = 16$, $d/\Lambda = 0.50$, wavelength $\lambda = 1\mu\text{m}$, $n_c = n_{\text{SiO}_2}$ and $n_s = n_c + 0.02$ (at $\lambda = 1\mu\text{m}$), we did parameter sweeping for V parameter ($V = \pi d \sqrt{n_s^2 - n_c^2} / \lambda$) of the cylinders by changing the diameter of the cylinders d . Note that we have d/Λ fixed, when d increases, Λ and R increase accordingly and the angle θ also changes according to equation (3.4). To illustrate this effect, the angle θ corresponding to the fundamental modes is plotted in figure 3.8(A), showing considerable small values supporting the approximation in equation (3.4) (here we used \sin and \tan in the calculation.). The small index contrast between the cylinders and the matrix, as well as between the cladding and the core, results in a polarization independent reflection, as it can be shown for the reflection at a single interface with the Fresnel equation. Therefore, we can use a single plane wave (transverse-magnetic (TM) polarization is used here, transverse-electric (TE) will be the same) as the incident field from port1.

The power transmission coefficient T for various V parameters, calculated at port2 in the planar model (figure 3.8(B)), exhibits maxima corresponding to the resonances in the cladding as the case for anti-resonant (AR) fibers. Figure 3.8(C) shows the related phase difference between the forward scattered and the incident electric field $\Delta\Phi = \arg(E_s/E_i)$. We noticed that the domains of low transmission are associated with phase difference close to 180° , demonstrating the importance to have a destructive interference in the microstructured cladding for achieving low loss guidance.

The reflection and transmission behavior at a core-cladding interface of a fiber with resonant cladding induce an additional phase change and loss compared to the case of a perfectly guiding core-cladding interface. Here, we calculate the dispersion (real part of the effective index of core modes $\text{Re}(n_{\text{eff}})$) and loss of the modes $Loss$ in the single-ring microstructured fiber analytically using the amplitude complex reflection coefficients r from the

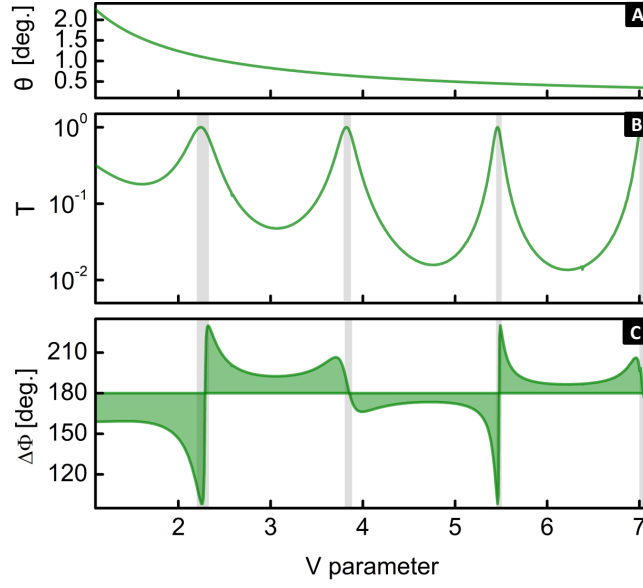


Fig. 3.8: The analysis for a single-ring microstructured fiber with a set of parameters: number of cylinders $N = 16$, $d/\Lambda = 0.50$, $\lambda = 1\mu\text{m}$, $n_c = n_{\text{SiO}_2}$ and $n_s = n_c + 0.02$. Regarding the V parameters of the surrounding cylinders ($V = \pi d \sqrt{n_s^2 - n_c^2} / \lambda$, here d is changing), the plots show: (A) Estimated incident angle θ for the fundamental mode HE11 corresponding to different core diameter d for specified V parameters; (B) The power transmission coefficient T corresponding to the angles θ and V parameters; (C) The phase difference between the forward scattered and the incident electric field $\Delta\Phi$. The gray color bars indicate the resonance positions of the cylinders.

planar model.

In addition to the case of perfectly reflecting core-cladding interface, the dispersion of the fundamental mode in such case can be expressed as:

$$\text{Re}(n_{\text{eff}}) = \sqrt{n_c^2 - \left(\frac{j_{01}}{k_0 R}\right)^2} + \frac{\Delta\Phi_r}{k_0 L}. \quad (3.5)$$

where $\Delta\Phi_r = \arg(r)$ is the phase change by the reflection. This can be thought of as from an effective penetration of the light into the cladding. Its analog in the total internal reflection of a linearly polarized beam is known as the Goos-Hänchen effect. The phase shift of the Goos-Hänchen effect can be physically understood as an interfering result between the plane waves of different propagation directions that compose the beam. Here, using expression (3.5) we show that the dispersion properties of the waveguides with resonant cladding depend, in addition to that of a perfectly reflection

guidance (first term in right hand side), on the phase change of the single reflection event.

Using the power transmission coefficient (T), the loss of the fundamental modes can be described as:

$$Loss[\text{dB/m}] = -10 \frac{\log_{10}(1 - T)}{L} \approx 10 \frac{T}{\log(10)L}, \quad \text{for } T \ll 1 \quad (3.6)$$

showing that, with approximation for low loss ($T \ll 1$), the loss is proportional to the power transmission coefficient of the single interface T .

In figure 3.9(A-B), we show the dispersion and loss of the fundamental mode in a single-ring microstructured fiber using the equation (3.5) and equation (3.6). The results from the planar model (olive lines) are confirmed with the results from the numerical mode calculation with the finite element method (FEM) for the same structure (red dots). Although the incident angles used in the reflection-based model were approximated for the case of perfectly reflecting cladding, we see that the results from the reflection-based model represent excellently the dispersion and loss of such large-core anti-resonant fiber. Only slight discrepancies are observed at small V parameters, which can be attributed to the larger angle θ requiring more critical assumptions.

The field distribution (E field norm $|E|^2$) in figure 3.9 demonstrates the correspondence between mode calculation (figure 3.9(C)) and the reflection-based model (figure 3.9(D)). Despite the simplification of the incident field being a TM-polarized plane wave, the excited fields in the cylinders, i.e. resonances, of the reflection-based model is consistent with that of the mode calculation.

The advantage of the reflection-based method we proposed here lies firstly in the fact that we reduce the calculation burden for large-core microstructured fibers. With the complex reflection coefficients from a simple numerical simulation in the approximated planar model, we can quantitatively analyze the dispersion and loss of the fundamental mode in the fiber using an analytical equation in a straightforward way regardless of core diameter. In addition, the method offers a simple model of transmission for qualitatively understanding the antiresonant behavior of a microstructured cladding. Note that we exhibited here the calculation for the fundamental core modes, which also holds for higher-order modes in a similar way.

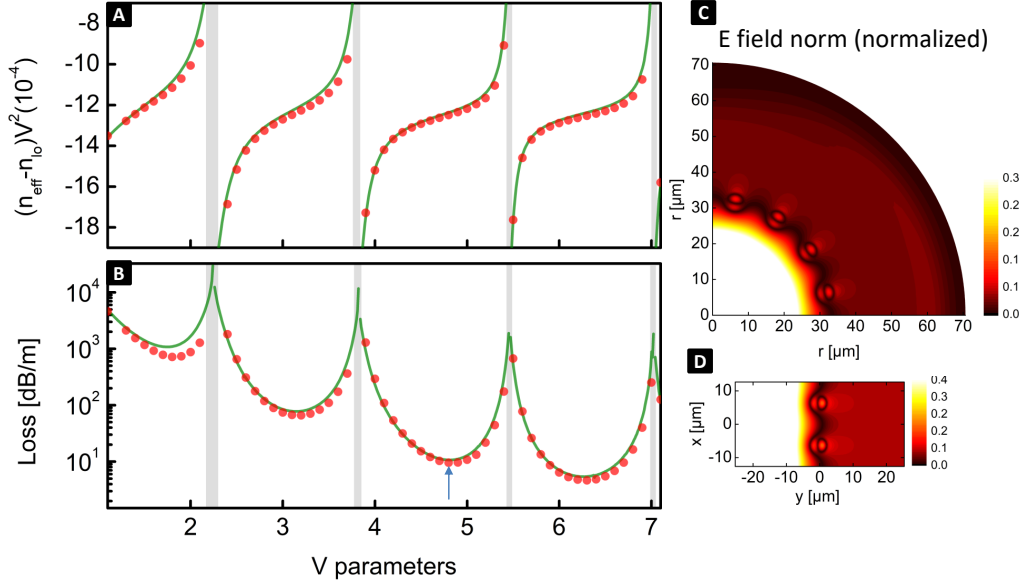


Fig. 3.9: The results calculated from the planar model (olive line) and from the FEM mode calculation (red dots) for a single-ring microstructured fiber with a set of parameters: number of cylinders $N = 16$, $d/\Lambda = 0.50$, $\lambda = 1 \mu\text{m}$, $n_c = n_{\text{SiO}_2}$ and $n_s = n_c + 0.02$. The plots show (A) the index dispersion and (B) the loss (dB/m) of the fundamental mode. The gray bars indicate the resonances of the cladding. The normalized E fields norms of an example solution corresponding to the arrow label in (B) are shown for both the quarter model of mode calculation (C) and the planar reflection model (D).

3.2.2 Parameter sweeping of the structure

Using reflection-based model introduced above, we did different kinds of parameter sweeping for the single-ring microstructured fiber, reaching unexpected situations of extremely low loss. The loss map from the parameter sweeping shows the regions of parameters giving same level of loss and the combination of the multi-parameters that leads to the lowest loss.

First, we focused the study on the region between the second and third resonances of the cladding and extended the calculation in figure 3.9 with another dimension by changing d/Λ of the structure. Figure 3.9(A) shows the loss map regarding the parameter V and d/Λ .

We confirmed the results from the reflection-based model with those from the mode calculation for data at $d/\Lambda = 0.3$ as plotted in figure 3.10(B). We see a good consistency between two results with a loss reaching $10^{-5} \text{ dB m}^{-1}$. In figure 3.10(C), also for data at $d/\Lambda = 0.3$, we show the phase difference $\Delta\Phi$ between the forward scattered field and the incident field compared with

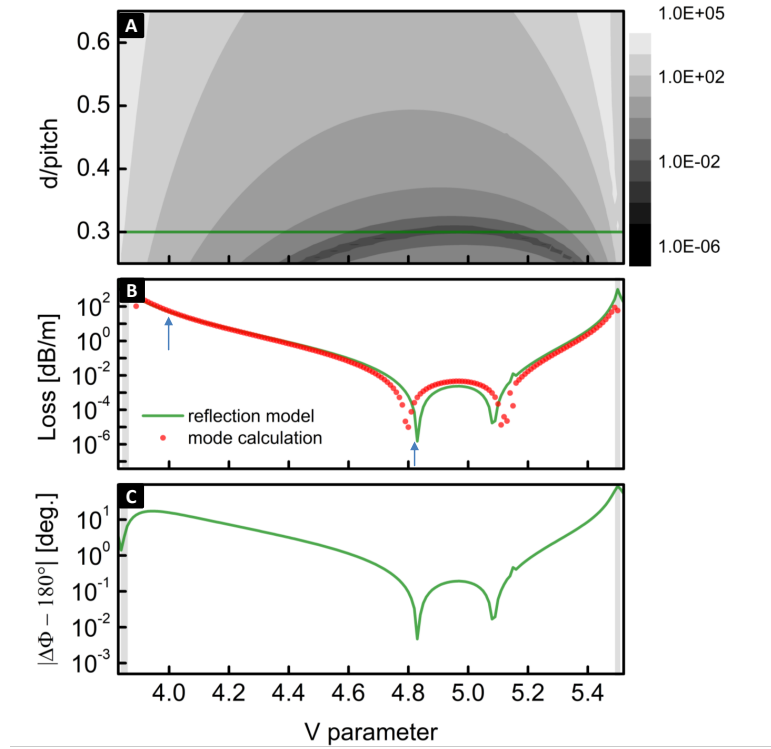


Fig. 3.10: (A) A loss map regarding d/Λ and V parameter of the surrounding cylinders for a single-ring microstructured fiber with the set of parameters: number of cylinders $N = 16$, $\lambda = 1\mu\text{m}$, $n_c = n_{\text{SiO}_2}$ and $n_s = n_c + 0.02$. (B) The loss plot of the cut-line in (A) ($d/\Lambda = 0.3$) from the reflection model (green line) and the mode calculation (red dots). (C) The phase difference between the forward scattered field by the structure and the incident field $\Delta\Phi$ compared with 180° for the corresponding data at cut-line. The gray color regions in (B) and (C) indicate the resonances of the cladding.

180° . We can see that $\Delta\Phi$ shows the same tendency as the loss and is very close to 180° for the parameters giving ultralow loss.

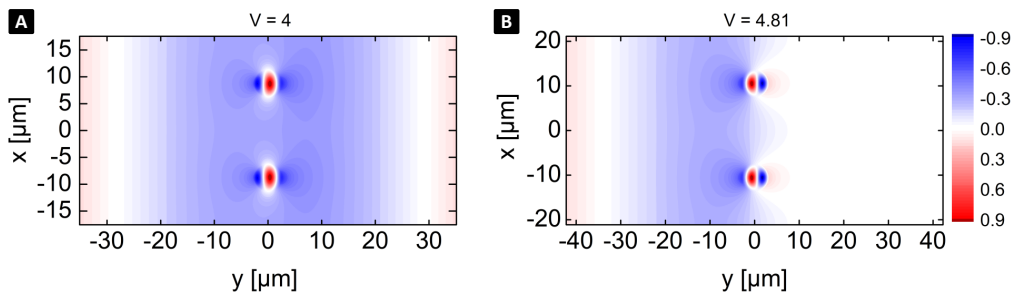


Fig. 3.11: Normalized E field z component plotted for the data labeled with arrows in figure 3.10: (A) $V = 4$; (B) $V = 4.81$.

To demonstrate the relevance of $\Delta\Phi$ for the waveguide losses, the normal-

ized z-component of the electric fields for the data labeled with two arrows in figure 3.10(B) are shown in figure 3.11. It is normalized by the maximum value to the range of $[0,1]$. We can see that the data giving phase difference very close to 180° ($V = 4.81$) has destructive interference after the structure. This is different for $V = 4$, which shows significant field transmission behind the structure. The results clearly reveal that the situation of anti-resonance in the cladding leads to low loss guidance.

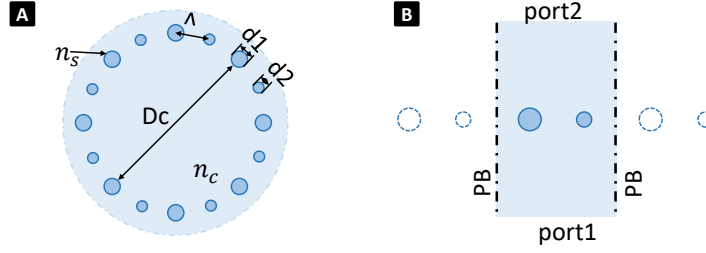


Fig. 3.12: Sketch of the cylinder-modified single-ring microstructured fiber and the corresponding planar reflection-based model.

Further, we studied a cylinder-modified single-ring microstructured fiber as shown in figure 3.12, in which the diameter of the cylinders alternates. The material indexes are the same as the previous case. The corresponding approximated planar model contents a unit of periodic structure. In addition to the previous studied single-ring microstructured fiber, with this cylinder-modified single-ring microstructured fiber, the alternating diameters offer additional degree of freedom to improve the guidance.

To calculate the loss map, we kept the core radius fixed (fixed pitch condition) for the data giving the lowest loss in the previous studied range (the R at $V = 4.81$), while sweeping the diameters of the neighboring strands (d_1, d_2). The loss map regarding V_1 and V_2 ($V_1 = \pi d_1 \sqrt{n_s^2 - n_c^2} / \lambda$, $V_2 = \pi d_2 \sqrt{n_s^2 - n_c^2} / \lambda$) are calculated using the planar model and shown in figure 3.13.

The loss map (figure 3.13(A)) here includes losses for two different cases regarding V_1 and V_2 . The left part in the loss map has V_1 in the region between the second and third resonances while V_2 in the region between the first and second resonances, while the right part has both in the the region between the second and third resonances. It is interesting to notice that the loss properties are different in these two cases. When the neighboring strands are of V parameters in different band gap (left part), ultralow loss appears

for certain combination of parameters. The situation is different when the neighboring strands are of V parameters in the same band gap (right part), showing rather flat loss dip.

The plot in figure 3.13(B) shows the loss at $V_1 = 4.81$ (cutline in figure 3.13(A)) calculated from the reflection-based model as well as from the mode calculation. Again they consist quite well with each other. The plot in figure 3.13(C) shows the phase difference between the forward scattered field and the incident field $\Delta\Phi$ compared with 180° , which highly consists with the trends of loss. We see in this case of cylinder-modified single-ring microstructured fiber, the phase difference can be very close to 180° giving ultralow loss.

In figure 3.14, we show the normalized E-field z component for the case of identical strands and the case with modified strands corresponding to the data labeled with arrows in figure 3.13(B). It is clearly to see that unlike the case of identical strands, the excited fields in the modified strands are of different order and the superposition of the fields results in stronger destructive interference.

The results clearly show that the coupling between the cylinders is essential for low-loss guidance. Such effect was also explained by the band gap concept, for example, in the work for pixelated Bragg fibers [87]. While the concept of band gap effect based on the coupling and forming of super-modes in the cladding is more about ideal periodic structures, the reflection and transmission analysis here is more practical to be used in cases with finite periodic structures and also modified periodic structures. Compared with the numerical modal calculation, a key advantage of the reflection-based model is the insight into the underlying physical mechanics of the light reflection process of the microstructure, allowing investigating sophisticated concepts from fields such as photonic crystals within the context of low-loss guidance leaky waveguides.

3.3 Conclusion

To summarize, we have developed efficient methods to investigate guidance with microstructured cladding, which consist of high index strands arranged periodically in a low index matrix, by its photonic band gap maps, as well as its reflection and transmission.

A complete analytical method using a binary function was developed

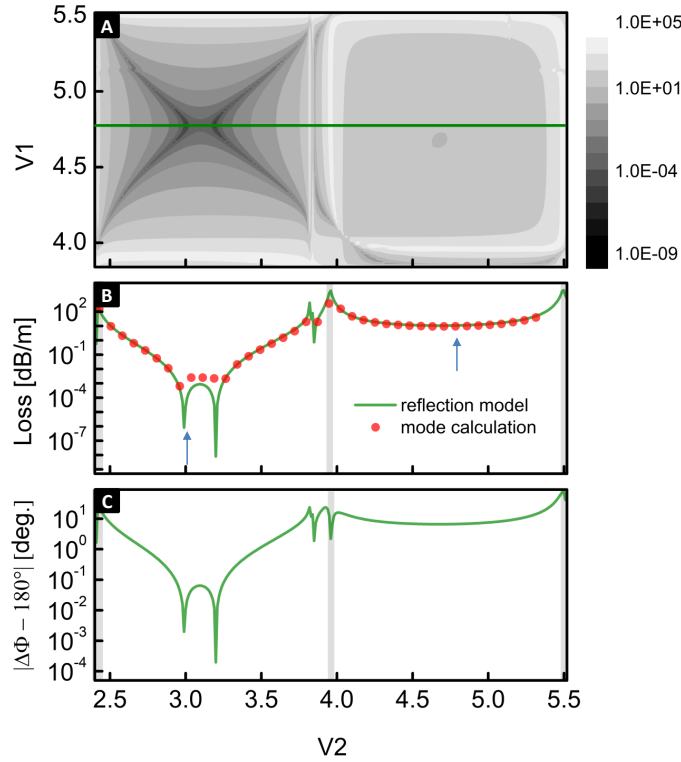


Fig. 3.13: (A) Loss map regarding parameters V_1 and V_2 for a cylinder-modified single-ring microstructured fiber with the set of parameters: number of cylinders $N = 16$, $\Lambda = 1.2669\mu\text{m}$, $\lambda = 1\mu\text{m}$, $n_c = n_{\text{SiO}_2}$ and $n_s = n_c + 0.02$. (B) Loss corresponding to the cutline in (A), where $V_1 = 5.81$, from the reflection model (green line) and the mode calculation (red dots). (C) Phase difference of the scattered field after structure to the incident field $\Delta\Phi$ compared with 180° for the corresponding data at cutline. The gray color regions in (B) and (C) indicate the resonances of the cladding.

from Birks' model to investigate the band gap map for an all-solid photonic band gap cladding, which consists of high index strands in hexagonal arrays embedded in silica. The method combined equations in Birks' model to a binary function and was proven very efficient to identify band gaps of photonic crystal fibers for different parameter combinations. With the binary function, the calculation using our self-written Python code is straightforward and takes only a few hours for the entire photonic band gap map, whereas with numerical simulation using finite element method it would be much more complex and time consuming.

Although the binary function was based on scalar wave equations with assumptions of low index contrast of the structure, a parameter analysis with small variations was done showing how the fundamental band gap deepens

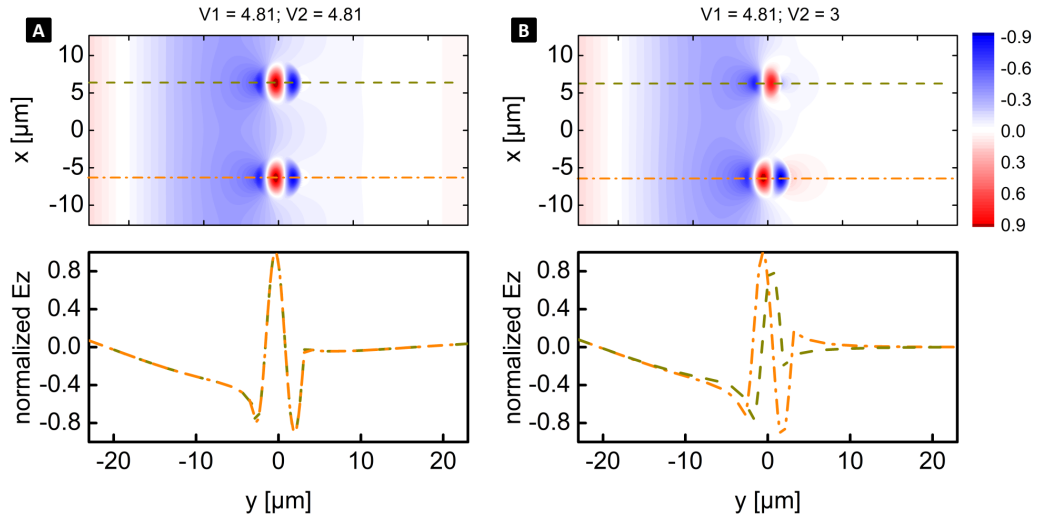


Fig. 3.14: Normalized E field z component plotted for the data labeled with arrows in figure 3.13: (A) for $V_1 = V_2 = 4.81$; (B) for $V_1 = 4.81$, $V_2 = 3$. The plots at the bottom show the two field distributions at the cutline of the corresponding colors.

with the increasing of the geometry parameter d/Λ or the increasing of the material parameter n_{hi} (kept n_{lo} unchanged). It indicates the ways to achieve light guidance in a core of lower index materials with all-solid band gap cladding.

We then introduced a reflection-based simulation method offering the possibility to qualitatively and quantitatively study the guidance loss of the core mode in a large core microstructured fiber from the perspective of the reflection and transmission of its structured cladding. Specifically, we applied an approximated planar model for analyzing the fundamental core modes of the all-solid single-ring microstructured fiber, which has high index strands arranged in a ring form in low index matrix. We modeled the reflection using an approximated planar model, which consists of only two strands with periodic boundary condition in COMSOL. We demonstrated that the power transmission in the planar model can be directly related to the loss of the guided modes based on the assumption of low loss guidance. Moreover, the phase difference between the forward scattered field and the incident field in the planar model reflects the interference of the fields allowing for better insights into the underlying physics of the guidance.

The exact dispersion and loss of the fundamental fiber modes were calculated from the complex reflection coefficient in the planar model and confirmed by the results from the corresponding numerical mode calculation.

Loss maps with massive parameters sweeping using the planar model were done for the all-solid single-ring microstructured fiber as well as its cylinder-modified version. We found particular parameter combinations allowing for ultralow loss. We revealed the destructive interference after the structured cladding for the case of low loss guidance.

The reflection-based planar model was approved as practical and efficient for analyzing guidance in a large core microstructured fiber with finite periodic structures and even modified periodic structures. The model is not limited to a single ring structure, but can be extended straightforwardly to more complex cladding geometries. Principally, it is available for all cases where the core diameter is much larger than the wavelength and the cladding is sufficiently thin for the approximation of a planar model to be valid. The model can also be applied to the structure with considerably higher refractive index contrast with an analysis of reflection from both TE- and TM- polarized incident wave in the planar model, as we did for the work discussed in the next chapter.

The guidance of light in air or water is of interest for many research fields including high power lasers, quantum experiments, nonlinear optics and ultra-fast spectroscopy. In this part of the work, we will introduce designs of novel microstructured fibers for light guidance in a water core or an air core.

All-solid photonic band gap (PBG) fibers utilizing the photonic band gap effect offer guidance of light in low index materials, while so far only in solid materials like silica. By increasing the index contrast or the ratio of the strand's diameter to pitch of an all-solid band gap cladding, we can have band gaps extended to lower index as discussed in previous section 3.1. Here, we proposed for the first time an example design of water-core all-solid band gap fiber, which has a core of index as water and is surrounded by all-solid band gap cladding. A semi-analytical method based on the reflection-based planar model, which has been discussed in the previous chapter, was applied on the investigation of the properties of its guided modes and verified by FEM simulations.

Due to the low refractive index of air, it is really difficult if not impossible to have guidance of light in air directly by all-solid band gap cladding, i.e. band gaps going below the air line. Here, we introduced an air-core waveguide, which consists of suspended polymer strands in air, implemented on chip by 3D direct laser-writing. It can be easily integrated on planar photonic circuitry and are promising for infusion of interesting gases into the core area of the waveguide for further applications.

4.1 Guidance in a water core

Here, we are proposing a design of the water-core all-solid photonic band gap fiber, which consists of an all-solid cladding with high index strands in hexagonal arrays embedded in silica and a central water-core of hexagonal shape as shown in figure 4.1. The idea is to place a water core in the defect of an all-solid band gap fiber. The water core has its boundary in the defect section formed by omitting several rings of the high index strands. The hexagonal shape of the core boundary fits the cladding structure with uniform distance from the boundary to the strands in the first ring of the

cladding.

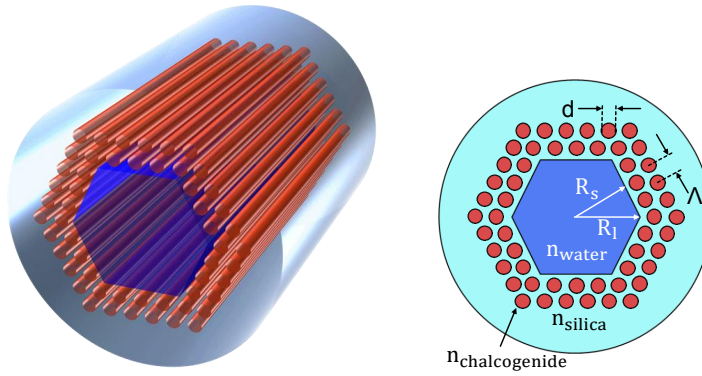


Fig. 4.1: Sketch of the water-core all-solid photonic band gap fiber and its cross section with the key parameters labeled.

The refractive index of the strands, the background and the core have been chosen to match those of chalcogenide (As_2S_3), silica (SiO_2) and water (H_2O) at 900 nm ($n_{chalcogenide} = 2.5$, $n_{silica} = 1.47$ and $n_{water} = 1.33$). The choice of these materials is from the consideration of the relative high index contrast of the photonic band gap cladding and also based on the numerous works [24, 88–91] demonstrating experimentally the implementation of hybrid chalcogenide/silica fibers with strands of sub-micrometer diameter. The key structure parameters for the band gap guidance are the diameter of strands (d), the neighboring distance of strands (pitch Λ) as well as the number of rings (N) in the cladding. For designing, a normalized parameter d/Λ based on the scaling law is used and chosen to be 0.44, which is in accordance with typical capillary dimensions used in the stack-and-draw method for fiber drawing. The hexagonal core can be characterized by either the shortest or longest possible radius (R_s and R_l) with $R_s = \sqrt{3}/2 \cdot R_l$. The inner silica wall facing the water is characterized by the distance of its boundary to the center of the strands of the first ring in the cladding g , which is assumed to be half of the pitch ($g = \Lambda/2$) considering the stack-and-draw process. The realization of the large hollow core in hexagonal shape fabricated using stack-and-drawing is challenging but was experimentally demonstrated in various publications including HCFs [38] and Kagome-design [49, 92].

In this section, we verified the possibility to guide light in the water core of our photonic band gap fiber. First, we calculated the band gap map for the photonic crystal structure of the cladding. Then, we analyzed the guidance of

the water-core all-solid band gap fiber by the simulation of a single reflection on the core boundary based on the reflection-based planar model. The dispersion and loss of the guided modes were calculated from the reflection parameters using a semi-analytical method, which were also confirmed by the calculation with FEM simulation. Moreover, we discussed several guiding properties of the proposed fiber regarding the geometry parameters (i.e. core radius, number of rings in the cladding) and the mode orders.

4.1.1 Photonic band gap for light guidance in a water core

To guide light in the water core of our photonic band gap fiber, the photonic crystal cladding must offer a band gap below the index of water. Due to the high index contrast, the analytical method based on scalar wave equation is invalid to give exact results. We simulated the cladding Bloch modes using the FEM method and calculated their DOS (density of states, details introduced in section 2.4) for the above proposed photonic crystal structure. To check the possible deepest band gap, the DOS map as a function of the real part of the effective index of the Bloch modes and the normalized parameter Λ/λ in the range of the fundamental band gap is shown in figure 4.2.

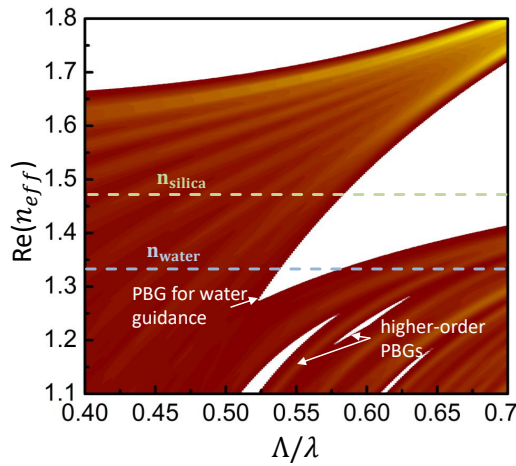


Fig. 4.2: DOS map of the photonic crystal cladding for the fundamental band gap range calculated for parameters: $d/\Lambda = 0.44$, $n_{\text{silica}} = 1.47$, $n_{\text{water}} = 1.33$ and $n_{\text{chalcogenide}} = 2.5$. The color scale ranges linearly from low (wine) to high (yellow) values of density of states. The white regions indicate zero cladding modes (band gaps). The dashed lines indicate the refractive index of silica (light green) and water (light blue) without considering dispersion. Band gaps below the water line are labeled with arrows.

We can see that the fundamental band gap of this photonic crystal struc-

ture goes far below the RI of silica and has a region ($0.53 < \Lambda/\lambda < 0.59$) below the RI of water, which is labeled as PBG for water guidance in figure 4.2. The possibility of the guidance is associated with high RI contrast between the strands and matrix ($n_{\text{silica}} = 1.47$ and $n_{\text{chalcogenide}} = 2.5$), while the geometry parameters including diameter of strands d , pitch Λ and wavelength can be scaled based on the normalized values: $d/\Lambda = 0.44$ and Λ/λ in the region of the band gap. Several isolated band gaps, which are labeled as higher-order PBGs in the map, appear in the lower region below the RI of water. They are not considered, as they support higher-order modes only, which are practically difficult to excite. Here we focused on the region of the fundamental PBG below the RI of water and examined the guided modes for different parameters in the following section.

4.1.2 Reflection model for the water-core all-solid photonic band gap fiber

While the possibility of the guidance is promised by the photonic band gap, the attenuation of the guidance scales directly with inverse cubed of the core radius as observed for a hollow core PBG fiber [47]. Therefore, for low-loss guidance in water, it is reasonable to assume a relative large core with the cladding structure proposed above.

To circumvent heavy simulations of the core modes with the FEM method for the large-core structure, here, we applied a semi-analytical method based on the reflection-based planar model for the water-core all-solid photonic band gap fiber (figure 4.3). Since the proposed fiber has a core of diameter being much larger than the wavelength ($R \gg \lambda$), it is possible to approximate the properties of the core modes based on the reflection of light on the core boundary as we have discussed with the reflection-based planar model in section 2.3.3 and 3.2. Therefore, a straightforward analytical calculation of both real and imaginary parts of the effective index (dispersion and loss) of the core modes can be done with the reflection parameters for the water-core all-solid photonic band gap fiber.

To apply the reflection-based model, we built up an approximated planar model of the proposed cladding structure in COMSOL, which is a slice of width equal to the pitch Λ including the cladding and the core-cladding interface (figure 4.4). We simulated the reflection regarding the angle ψ of light ray to the the core-cladding interface as labeled in figure 4.3. For the

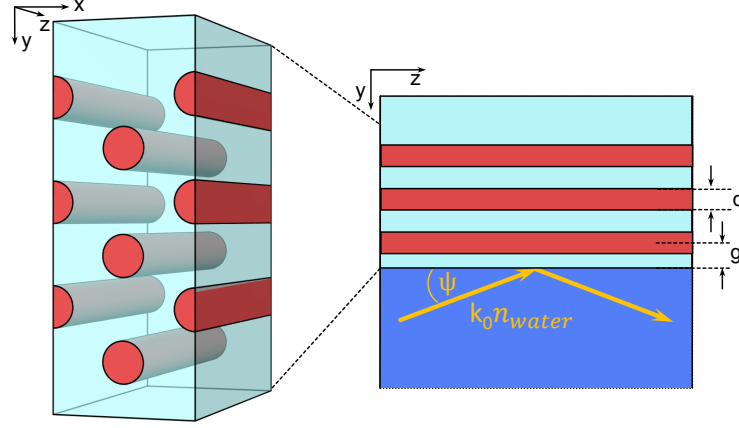


Fig. 4.3: Sketch of the planar model for the water-core all-solid photonic band gap fiber.

physics, we set the left and right boundaries as periodic boundary and the top and bottom boundaries as port. Due to the high index contrast of the structure, both TE and TM polarized incident waves were considered here. The excitation of the field on port1 was either E_x or H_x respectively for TE or TM polarized waves with a propagation constant $k_{y1} = |k_0 n_{water} \sin(\psi)|$ at port1 and $k_{y2} = |\sqrt{k_0 n_{silica}^2 - (k_0 n_{water} \cos(\psi))^2}|$ at port2. To obtain the corresponding reflection coefficients at the core-cladding interface, the additional phase was added to the S-parameters resulting in a complex reflection coefficient as $r = S_{11} \cdot \exp(2ik_{y1}c)$, where c is the distance from port1 to the interface.

Plots in figure 4.4 show an example of the dependence of the reflection coefficients on the angle ψ , which was calculated for a parameter combination in the middle of the band gap ($\Lambda/\lambda = 0.545$), for the case of our proposed structure. The fittings in figure 4.4 confirm that the reflection coefficient r can be approximated here by a series expansion to the quadratic term regarding small angle ψ : $r = -1 + q_1\psi + q_2\psi^2 + O(\psi^3)$, where $q_1 = q_1' + iq_1''$ and $q_2 = q_2' + iq_2''$ were used for further calculation of the effective index of the modes. While (q_1^e, q_2^e) and (q_1^m, q_2^m) were used for calculation of TE and TM modes, in case of hybrid modes (i.e. HE_{11}), we assumed its parameter q_1 and q_2 as $q_1 = (q_1^e + q_1^m)/2$, $q_2 = (q_2^e + q_2^m)/2$.

By considering the loss per reflection and the phase induced per reflection, which we have discussed in detail in the theory part for the reflection-based model (section 2.3.3), we calculated the real and imaginary part of the effective index of the core modes using the following analytical expression with

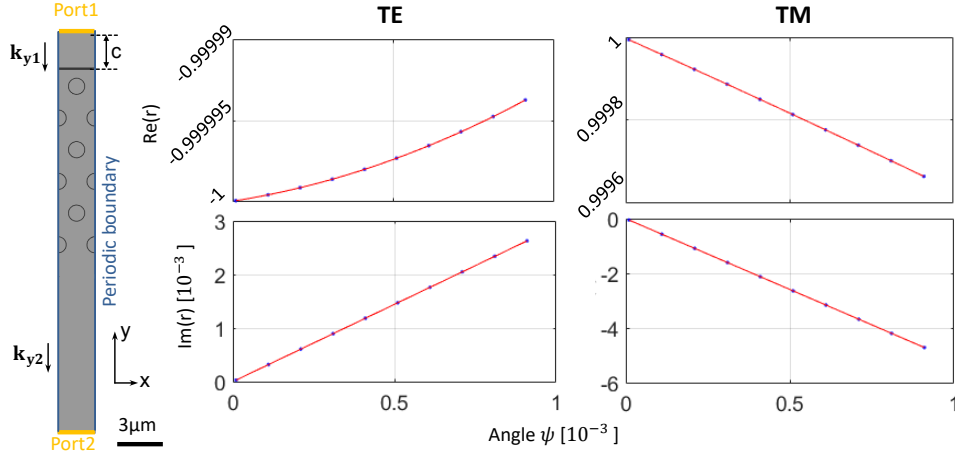


Fig. 4.4: Planar reflection model built in COMSOL and the example plots of the dependence of the real and imaginary parts of the reflection coefficients $r = S_{11} \cdot \exp(2ik_{y1}c)$ on the angle ψ for TE and TM incident waves. The calculation was done for the structure as proposed before ($d/\Lambda = 0.44$, $n_{\text{silica}} = 1.47$, $n_{\text{water}} = 1.33$ and $n_{\text{chalcogenide}} = 2.5$) in the middle of the band gap ($\Lambda/\lambda = 0.545$). The dots are the data points and the red line shows the fitting result.

core radius as a parameter.

$$n'_{eff} = n_{\text{water}} \left[1 - \frac{j^2}{2k_w^2 R^2} + \frac{D_1 j^2}{2k_w^3 R^3} + O\left(\frac{1}{k_w^4 R^4}\right) \right] \quad (4.1a)$$

$$n''_{eff} = n_{\text{water}} \left[\frac{C_1 j^2}{2k_w^3 R^3} + \frac{C_2 j^3}{2k_w^4 R^4} + O\left(\frac{1}{k_w^5 R^5}\right) \right] \quad (4.1b)$$

where $k_w = k_0 n_{\text{water}}$. Parameters C_1 , C_2 and D_1 are based on the reflection parameters: $C_1 = 2q'_1$, $C_2 = 2q'_2 - |q_1|^2$ and $D_1 = -q''_1$. The j indicates the root of the Bessel function defined as following (higher order modes were also discussed for the proposed fiber):

$$j = \begin{cases} j_{1,n} & TE_{0n}, TM_{0n} \\ j_{m-1,n} & HE_{mn} \\ j_{m+1,n} & EH_{mn} \end{cases}$$

where j_{mn} is the n^{th} zero of the Bessel function J_m ($J_m(j_{mn}) = 0$).

As we can see from the analytical expression for the effective index (equation 4.1), the radius of the core is a variable in the analytical expression. With the reflection-based planar model, it is valid to calculate directly cases

of different core radius of the water-core all-solid band gap fiber, while with FEM model, renewed numerical calculation is needed for the cases of different core radius. Here, we have to note that the core radius, which is used in the analytical expression of the complex effective index, is to some extent undefined due to the hexagonal shape of the core. Therefore, we checked two extreme values of the core radius (R_s and R_l , defined in figure 4.2) for the calculations with the reflection model.

4.1.3 Results and discussion

We first show the complex effective index of the fundamental mode guided in the water-core all-solid photonic bandgap fiber calculated using FEM in COMSOL (a quarter-model introduced in section 2.4.1), as well as the reflection parameters from our reflection model.

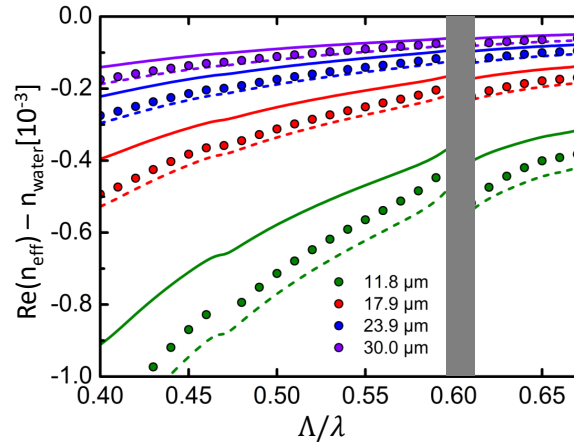


Fig. 4.5: Dispersion of the normalized real part of the effective index of the fundamental mode (HE_{11}) for the water-core all-solid photonic band gap fiber with four different values of core radius: R_s : $11.8\mu\text{m}$ (green), $17.9\mu\text{m}$ (red), $23.9\mu\text{m}$ (blue), $30\mu\text{m}$ (purple) and number of rings: $N = 6$. The solid and dashed lines refer to the analytical calculation by the reflection model with core radius defined by R_l and R_s , respectively. The dots refer to the results of the FEM. The gray region covers the exceedingly high loss part caused by the resonance of the cladding supermodes.

Figure 4.5 shows the dispersion of the normalized real part of the effective index of the fundamental mode for different values of the water-core radius. We can see that the dispersion of $Re(n_{eff})$ follows the expected behavior of the phase index with increasing values towards higher frequencies. The bending of the dispersion close to the frequencies of the resonances, where coupling to the cladding modes happens, results from the anti-crossing of the

core modes with the cladding modes. The results from the FEM calculation (dots) lie in-between the two curves calculated from the reflection parameters with the radius being the two extreme values, showing the consistence of the two methods. The results of the approximated analytical calculation with the reflection model are more close to the results of numerical calculation for the case of larger core radius as expected.

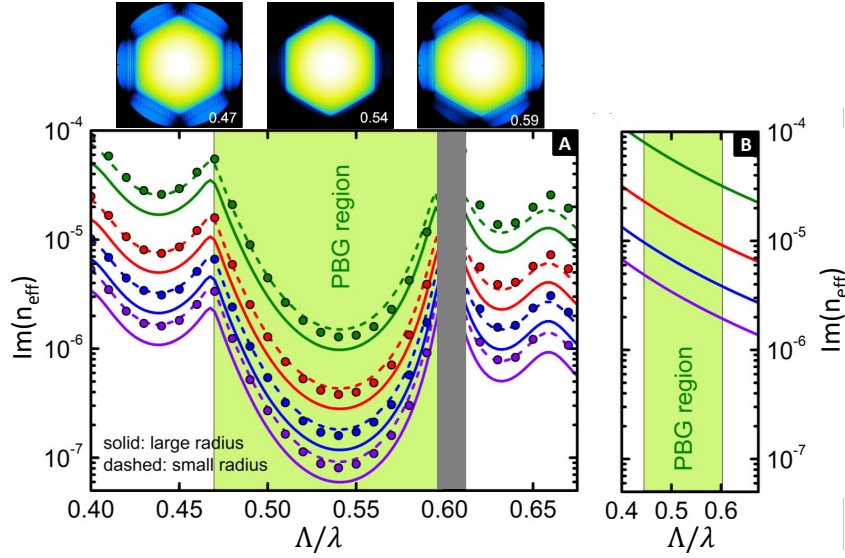


Fig. 4.6: (A) Dispersion of the imaginary part of the effective index of the fundamental modes (HE_{11}) for the water-core all-solid photonic band gap fiber with four different values of core radius: R_s : $11.8\mu\text{m}$ (green), $17.9\mu\text{m}$ (red), $23.9\mu\text{m}$ (blue), $30\mu\text{m}$ (purple) and number of rings: $N = 6$. The solid and dashed lines refer to the analytical calculation by reflection model with core radius defined by R_l and R_s , respectively. The dots refer to the results of the Finite-element simulations. The gray region covers the exceedingly high loss part caused by the resonance of the cladding supermodes. The three images above the plot show spatial Poynting vector distributions (decadic logarithmic color code, white:1, dark: $5 \cdot 10^{-5}$) for core radius R_s : $17.9\mu\text{m}$ at three selected normalized frequencies Λ/λ : 0.47, 0.54 and 0.59. (B) Dispersion of the imaginary part of the modes of a silica capillary filled with water with the core radius as in (A). The green regions highlights the photonic band gap region of the water-core all-solid fiber.

The dispersion of the imaginary part of the effective index of the fundamental modes in the water-core all-solid band gap fiber shows the typical features observed for band gap guidance (figure 4.6(A)): within the spectral region of the PBG in figure 4.2 (green region here), the imaginary part of the refractive index has lower values with an apparent dip in the middle compared with the values outside. The examples of the modal profile at three selected normalized frequencies Λ/λ : 0.47, 0.54 and 0.59 show clearly

more leakage of light into the cladding when it is close to the edge of the band gap, whereas the mode is well confined in the middle of the band gap. The consistent tendencies of the results from the two methods reveal that the loss of light guidance in the water-core all-solid cladding band gap fiber can be understood through the reflection of the ray at the core-cladding interface. It is important to notice that close to the resonances (the region we overlaid with gray bar), where light couples strongly to the cladding modes, the assumption of a high reflectivity (small incident angle at the boundary) from the cladding is not fulfilled any more, leading to the invalidity of the results from the reflection model. However, these regions are associated with high attenuation and are not interesting for any application.

To see the relevance of the microstructure in the cladding, we compared the imaginary part of the refractive index of the mode in our structure (figure 4.6(A)) with the one of the modes in a water-filled silica capillary with corresponding radius (figure 4.6(B)). It shows that the PBG effect from the structure reduces losses of the mode by a factor of about 45 at the mid-gap frequency.

The results presented above have shown an influence of the water-core radius on the modal attenuation. More data for different values of the core radius at the mid-gap frequency ($\Lambda/\lambda = 0.545$) were collected in figure 4.7(A) showing the dependency of the imaginary part of the effective index of the fundamental mode on the value of the core radius (R_s). Due to the unavoidable consuming of time, we calculated only four data points of the core radius by the FEM simulation and fitted them by a polynomial function with the exponent being one fitting parameter. We can see in figure 4.7(A) that the fitted curve (red line) and the data from analytical expression of reflection model (purple line) have both shown a scaling of the modal loss with inverse cubed of the core radius (FEM: $Im(n_{eff}) = 0.00178 \cdot R^{-2.932}$, reflection model: $Im(n_{eff}) = 0.00243 \cdot R^{-2.99}$), which agrees with the radius dependency of the loss for the cases of hollow core photonic band gap fibers or metamaterial fibers[76, 93].

The number of rings in the cladding of the band gap fiber is another key aspect regarding the modal attenuation. By fitting the data from the FEM simulation as well as the reflection model, we found that for the case of water-core all-solid band gap fiber the imaginary part of the effective index of fundamental mode scales exponentially with the number of rings (FEM:

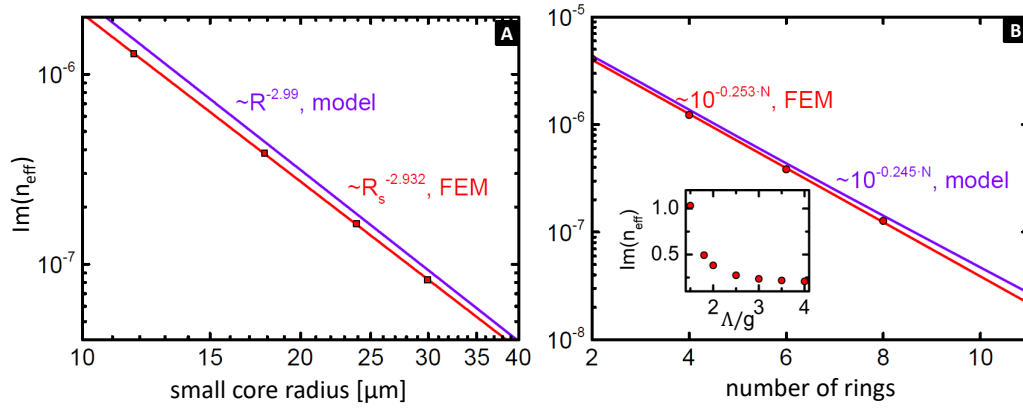


Fig. 4.7: Dependency of the imaginary part of effective index $Im(n_{eff})$ of the fundamental mode (HE_{11}) on various structural parameters. (A) Dependency on the core radius (R_s for the analytical expression) with fixed parameters: $N = 6$, $\Lambda/\lambda = 0.545$. The data from FEM simulations are indicated by squares and fitted by a polynomial functions with the exponent being a fit parameter. The purple line refers to the data from the analytical expression of the reflection model. (B) Dependency of the $Im(n_{eff})$ on the number of rings with fixed parameters: $R_s = 17.9 \mu\text{m}$, $\Lambda/\lambda = 0.545$. The circles are data calculated from the FEM simulation and the purple line refers from the corresponding results from the reflection model. Both have been fitted by exponential functions. The inset shows the $Im(n_{eff})$ depending on Λ/g , where g is the thickness of the silica wall around the core and number of rings is 6. All other parameters used here are the same as the proposed geometry ($d/\Lambda = 0.44$, $n_{silica} = 1.47$, $n_{water} = 1.33$ and $n_{chalcogenide} = 2.5$).

red line $Im(n_{eff}) = 1.275 \cdot 10^{-5} \cdot 10^{-0.252 \cdot N}$, reflection model: purple line $Im(n_{eff}) = 1.317 \cdot 10^{-5} \cdot 10^{-0.245 \cdot N}$, in figure 4.7(B)). By adding one more ring of the strands in the cladding, the modal loss can be reduced by about 5 dB. It has to be noticed that so far the calculation was done for a silica wall around the core of thickness g related to the cladding geometry as $\Lambda/g = 2$, whose change will also influence the modal attenuation. The inset in figure 4.7 (B) deals with the change of the thickness g of the silica wall (defined in figure 4.3) in a range feasible for fabrication. Since the frequency we analyzed is in the middle of the band gap $\Lambda/\lambda = 0.545$, we see that for the case $\Lambda/g = 2$ or even larger ratio, the wavelength is way larger than the dimension of the silica wall and the influence of the silica wall thickness on modal attenuation is substantially less pronounced. For smaller ratio Λ/g (i.e. thicker walls with comparable dimension to the wavelength), the modal attenuation will grow exponentially with the increase of the silica wall

thickness due to the increased surface modes held by the silica wall.

The validity of the reflection model has been proven with the previous calculations (figure 4.5 - 4.7) especially for the case of a large core radius, providing a tool for straightforward parameter sweeping to optimize guidance. The simulation with reflection model, analyzing only the reflection at the boundary of the water core, minimizes considerably the computing burden compared with the FEM simulation, especially for an enlarged geometry. Therefore, we were able to plot a loss map for the fundamental mode by investigating a wide range of the geometry parameters d/Λ together with the normalized frequencies as shown in figure 4.8.

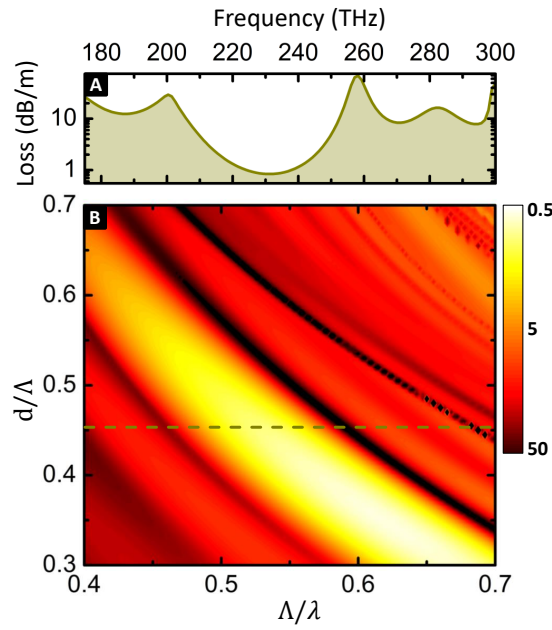


Fig. 4.8: (A) The loss plot in frequency domain for the previous used geometry parameters $d/\Lambda = 0.44$ and core radius $R=50\mu\text{m}$. (B) Loss map regarding Λ/λ and d/Λ for the fundamental mode (HE_{11}) of the water-core all-solid photonic band gap fiber calculated using reflection model ($R=50\mu\text{m}$). The color bar scales from bright yellow (low loss) to dark red (high loss) in units of dB/m. The dashed cut line corresponds to the data of the loss plot shown above the map. The material parameters used here are the same as previous ($n_{\text{silica}} = 1.47$, $n_{\text{water}} = 1.33$ and $n_{\text{chalcogenide}} = 2.5$).

In the map in figure 4.8, the combinations of the structure parameters offering low loss are the region of bright yellow color. We can see that a band gap in the frequency domain shifted by the change of the structural parameters d/Λ . This loss map covers all feasible combinations of the structural parameters of the band gap cladding exhaustively, meaning that for a given combination of material parameters this map is enough to identify the loss of

the fundamental mode for any combination of the structural parameters in practice.

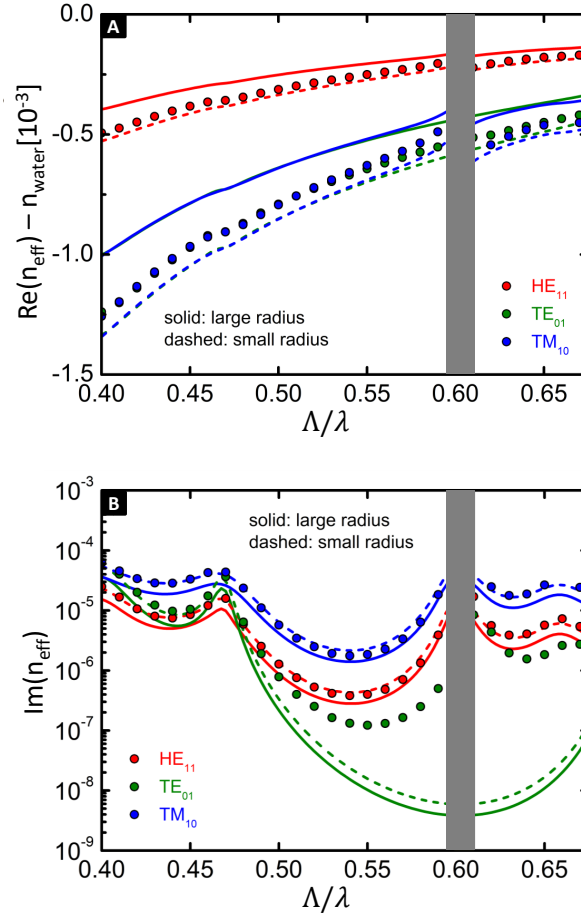


Fig. 4.9: Spectral distribution of the real (A) and imaginary (B) part of the effective index for the three lowest order modes of the water-core all-solid photonic band gap fiber with parameters: $R_s = 17.9 \mu\text{m}$, $d/\Lambda = 0.44$, $n_{\text{silica}} = 1.47$, $n_{\text{water}} = 1.33$ and $n_{\text{chalcogenide}} = 2.5$. The solid and dashed lines refer to the analytical calculation by reflection model with core radius defined by R_l and R_s respectively. The dots refer to the results of the Finite-element simulations (red: HE_{11} , green: TE_{01} , blue: TM_{01}). The gray region covers the exceedingly high loss part caused by the resonance of the cladding supermodes.

Besides the fundamental mode (HE_{11}), our water-core all-solid photonic band gap fiber can support several higher order modes. Here we show the real and imaginary part of the effective index for the three lowest order modes (HE_{11} , TE_{01} and TM_{01}) calculated with both the FEM simulation and the reflection parameters (figure 4.9). For the spectral distribution of $Re(n_{\text{eff}})$, the mode HE_{11} shows the largest phase index overall as expected for the fundamental mode. Moreover, the dispersion of the mode TM_{01} shows

particular pronounced bending when approaching the resonances, suggesting a strong interaction with the the cladding modes. The spectral distribution of $Im(n_{eff})$ reveals an interesting phenomenon, that the loss of the TE_{01} mode is below the loss of the HE_{11} mode in the band gap region, which has been also observed for hollow core fibers of other types such as Omniguide design[94]. Since the water-silica interface itself has a close-to-unity reflection in the case of large core radius, we believe that our water-core all-solid band gap fiber is distinguished from the typical all-solid band gap fiber and actually a waveguide combining different guidance principles.

The spectral distributions of the effective index of the HE_{11} and TM_{01} modes calculated with reflection parameters agree with those from FEM simulations, whereas an obvious discrepancy was found for the $Im(n_{eff})$ of the TE_{01} mode. The results from the reflection model for the $Im(n_{eff})$ of the TE_{01} mode disregard the resonance at around $\Lambda/\lambda = 0.6$ and show lower loss in the band gap region. The reason for this effect can be that the planar reflection model neglects the actual hexagonal shape of the core. A close look into the modal field shows that the corners of the hexagonal core support in no case entirely TE-polarized fields and include always a fraction more like TM-polarized fields, which was not considered in the analytical calculation for the TE_{01} mode by involving only the TE-related reflection parameters.

We believe that we have proved the guidance of light in our proposed water-core all-solid band gap fiber by the low modal attenuation and the modal profiles. Besides, it is interesting to notice that the planar reflection model built for the designed structure gave results matched well with that from the FEM simulation for the fundamental modes. From the practical perspective, the high index inclusions and hexagonal shape core in our proposed concept may be challenging to be implemented, but it is possible based on the current technique as we discussed at the beginning. For its unique structure of all-solid cladding with a single central channel and capacities of guiding light in liquids of index like water with low attenuation, the proposed fiber can substantially widen the application range of PBG fibers. This theoretical work is published with a discussion on the experimental feasibility of the proposed design and further application from the practical perspective [95].

4.2 Guidance in an air core

Here, we would like to introduce a hollow core waveguide consisting of 12 suspended polymer strands arranged in a hexagonal ring as shown in the inset of figure 4.10(A). We estimated the cladding modes of such leaky waveguides using the analytical binary function based on Birks's model (introduced in section 3.1). To explore its guidance properties, its fundamental core modes were simulated using the multipole method (CUDOS MOF) (introduced in section 2.4.2) .

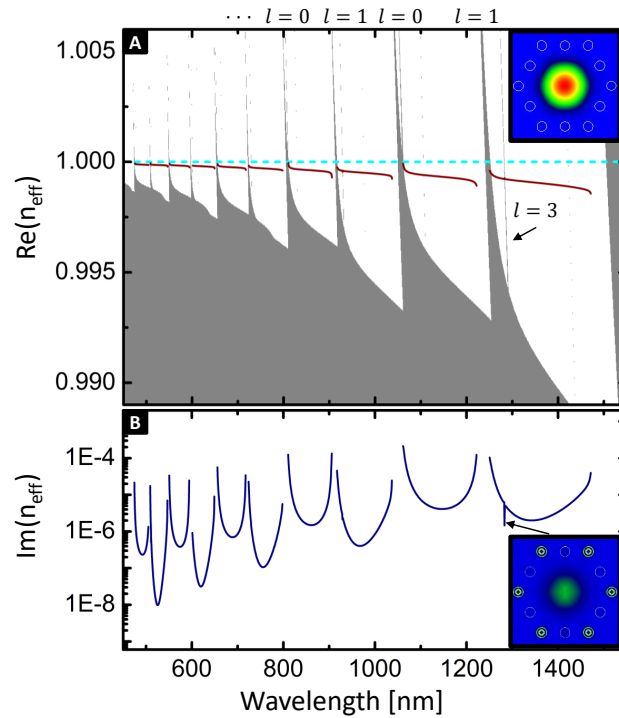


Fig. 4.10: Simulation of the complex effective index of the modes in the hollow core waveguide consisting of polymer strands arranged in a hexagonal ring with parameters: refractive index: 1.52, diameter: $3\mu\text{m}$ and pitch: $7\mu\text{m}$. (A) Dispersion of the real part of the effective index $Re(n_{eff})$ (red line). The gray region shows the bands of the cladding modes, overlaying of the first 5 orders, estimated with the Birk's model. The dashed light-blue line indicates the index of air. l labels the order of the corresponding LP modes. The inset shows the structure and the z component of the Poynting vector of the fundamental mode at wavelength 485 nm. (B) Imaginary part of the effective index $Im(n_{eff})$ of the modes. The inset shows the z component of the Poynting vector of the mode corresponding to the spike.

In figure 4.10(A), we show the bands of the cladding modes (gray region) calculated with the binary function based on Birks' model. It is just a rough estimation, since instead of 2D photonic crystal lattice, we have only a single

ring structure. Besides, the approximation for Birks' model is only suitable for the low order modes due to the large index contrast here. However, the real part of the complex effective index ($Re(n_{eff})$) of the fundamental modes (red lines) calculated numerically fits well in between the bands of the cladding modes. The inset shows the Poynting vector z component of an example mode at wavelength 485 nm, which has an effective mode area of around $215\mu\text{m}^2$ located in the center of the hollow core with a distance to the surrounding polymer strands.

The corresponding imaginary part of the complex effective index ($Im(n_{eff})$) is shown in figure 4.10(B). We can see that $Im(n_{eff})$ gets larger near bands, and the minimum of the dips increases for larger wavelengths as in case of anti-resonant guidance [57]. It is also noticed that the minimum of the dips above the second order bands ($l = 1$) show lower value than that of its neighboring dips above the first order bands ($l = 0$). It can be explained by the easier coupling to the first order cladding modes for a smaller index difference between core modes and the first order bands compared with that between core modes and the neighboring second order bands [75]. We also noticed a dip in the last dip, which corresponds to the coupling to a higher order highly dispersive mode of the cladding as shown by the modal profile in the inset in figure 4.10(B). Due to the large dimension of the strands, there are quite a large amount of higher order modes, which aren't shown here, but it is already clearly noticed with the calculation for the first 5 order modes that higher order cladding modes barely affect the loss of the core modes, especially at small wavelengths. This inhibited coupling between the core modes and the cladding modes can be explained by the strong transverse-mismatch between the core and cladding modes [52, 96].

From the simulation, we see that 12 polymer strands arranged in a hexagonal ring offer guidance along wavelength range from visible to infra-red in the central hollow core based on a guidance mechanism in combination of anti-resonant guidance and inhibited coupling guidance. In the following sections, we show that samples of different lengths of such "light cage" structures were fabricated on silicon chips by the 3D direct-laser-writing and characterized under the microscope. The guidance of light with these hollow core waveguides was verified by the transmission spectra and output modal profiles.

4.2.1 Light-cage written by 3D direct laser writing

Practically, hollow core waveguides “light cage” consisting of 12 polymer strands and supporting elements were directly written by laser on the silicon chips as shown in figure 4.11. The details of the fabrication will be described in this section.

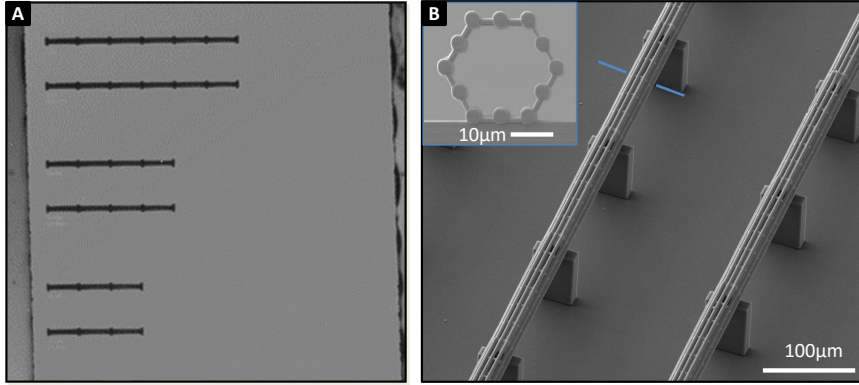


Fig. 4.11: Fabrication of the light cage: (A) the microscopy image of a sample with light cages in different lengths on a silicon substrate. (B) close look of the structure with a SEM image. The inset shows the cross section of the light cage.

The light cage structures were fabricated on polished silicon substrates (done by our collaboration group at Imperial College London) using a commercial femtosecond-laser based lithography system (Photonic Professional GT, Nanoscribe), which realizes 3D direct laser-writing in a UV sensitive photoresist (IP-Dip, Nanoscribe) based on two photon polymerization. This system uses Er-doped fiber laser operating at a wavelength of 780 nm with pulse duration of 100 fs, peak power of 25 kW and repetition rate of 80 MHz. The laser-writing works by focusing the laser beam in the photosensitive material and scanning it laterally by galvanometric mirrors (moving-beam fixed-sample (MBFS) approach), while the sample can be vertically moved by the piezo-actuator for 3D structures. The voxel size of the writing process, the volume in the photoresist that is cured by the focused laser light, is around hundreds nanometers, which is determined by the factors including the laser spot size, the power of the laser source and the properties of the photosensitive material itself. The system makes it possible to write structure from the microscale to mesoscale with high resolution (in the scale of the voxel size). The mesoscale structures need to be written line-by-line and layer-by-layer. The distances between adjacent lateral lines and vertical layers are referred to

as hatching and slicing distance respectively in the Nanoscribe manual. After the laser-writing, the rest of the photoresist is removed with the following processes: immersing the sample first in a bath of photo-resist developer (PGMEA, Sigma-Aldrich) for 20 min, then in 1-methoxyheptafluoropropane (3M, Novec) for 2 min and at last, drying it under a gentle stream of Nitrogen gas.

Figure 4.11 shows a sample fabricated by the above described method and the scanning electron microscope (SEM) image of the final light cage structures. Due to the limited lateral scanning range based on the movement of the Galvano-mirror (around $200\mu\text{m}$), the structures in length of 5 mm to 10 mm were actually written segment by segment. Each segment is in length of around $180\mu\text{m}$ and written consecutively by moving the mechanical stage in the system. The 12 strands forming the hollow core structure were arranged in a hexagonal ring with supporting struts. To have the structure suspended in air with a suitable height for direct coupling with fiber, we arranged supporting blocks for each segment. In order to minimize self-shading from the previously written structures, a certain writing order was followed: the supporting blocks were printed first, then the individual strand followed by its supporting struts. The supporting blocks and struts were written with hatching and slicing distance both of 250 nm and a writing speed of 40 mm s^{-1} , while the strands of the light cage were written with a hatching distance of 150 nm, a slicing distance of 100 nm and a writing speed of 25 mm s^{-1} . The “light cage” structures in different lengths are aligned on one side to the edge of the silicon substrate with a short distance for further optical characterization.

The direct laser-writing method offers a convenient way to implement the light cage structures of different designs. However, there are inevitable limitations. First, although laser writing offers writing vessels down to hundred nano-meters, the size of the strands cannot go down freely as we wish for that if the polymer strands are not thick enough, the strength of the strands wouldn’t be enough to form the suspended structure. Second, the core size of the structure, which is directly related to the pitch between strands, cannot be scaled up without limitation considering the stability of the structure. For example, we observed collapshion of the top part of the hexagonal ring and a deformed core for a structure of a large pitch. More details about

the fabrication limits and tolerances can be found in this published work [97].

4.2.2 Optical characterization of a Light cage

Light cage guides light with two dimensional confinement like fibers. Here, we measured transmission spectra and modal profiles of light cages with a setup as sketched in figure 4.12. The sample, silicon substrate on which light cage structures of different lengths are written, was mounted on a 3-axis stage for the selective coupling into individual structure. We collimated a broad band light source (NKT SuperK COMPACT super-continuum source: spectral range from 450 nm to 2400 nm with the pump at 1064 nm) and coupled it into the core of the structure with a $10\times$ objective. For the transmission spectral measurement, the output light from the structure was collected with $10\times$ objectives into a large core fiber (FG050LGA, core size $50\mu\text{m}$, $\text{NA}=0.22$) connected to an optical spectral analyzer (AQ-6315A, Ando). We optimized the coupling of the system at 900 nm before each measurement. The transmission spectra were recorded with a resolution of 2 nm or 5 nm, which were then normalized by subtracting the spectrum measured without sample. To image the output modes, we used narrow band filters to have light source at certain wavelengths and applied a CCD camera after the output objective.

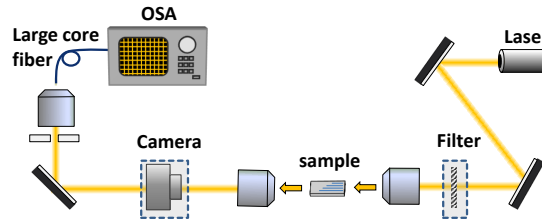


Fig. 4.12: Sketch of the setup for characterization of the “light cage” sample. The dashed squares indicate the elements that are removable.

Normalized transmission spectra in wavelength range from 600 nm to 1350 nm for “light cage” structures in different lengths (0.7 mm, 1.4 mm and 6.3 mm) are shown in figure 4.13. We observed dips in the transmission spectra, which correspond to the resonances of the cladding (figure 4.10). We can see that the transmission window broadens and the loss increases at longer wavelengths, which is consistent with the simulation results. The contrast of the dips in the spectra gets more distinct as the length of the structure increases, which results from a longer interaction distance for coupling from

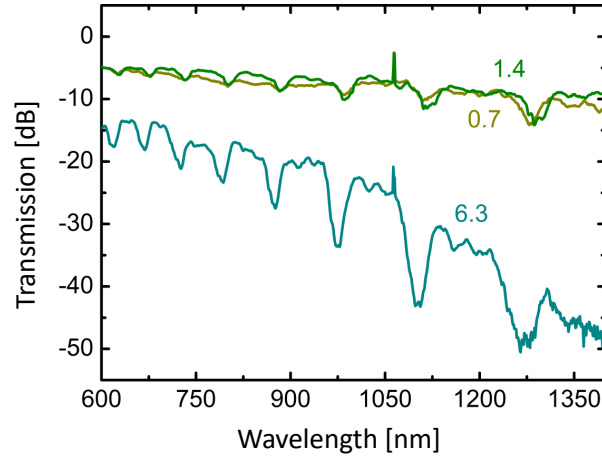


Fig. 4.13: Transmission spectra of “light cage” structures in different lengths: 0.7 mm, 1.4 mm and 6.3 mm as labeled with the corresponding color of the spectrum. The small peak around 1064 nm is from the pump of the laser source.

the core mode to cladding modes.

The longest structure I measured has a length of 10.5 mm (not the limitation), whose transmission spectrum is shown in figure 4.14. The inset in figure 4.14(A) shows the SEM image of the end face of the “light cage” structure. We found that the three strands at the top of the structure collapsed together with almost no gap at this end face of the structure. Despite the defect of the structure, the transmission spectra seem not affected. It is for the reason that the strands are well separated and supported by the struts along the structure (figure 4.11) except at the end face and the variation of the pitch in this small range has little influence on the spectra.

From the modal profile images in figure 4.14(B), we see that the output mode at the end face of the light cage structure is not centrally located in the structure. We suppose that the deformed structure end face does influence the output modal profile and similar deformation at the input end face may affect the coupling of the laser light to the individual structure. It was also noticed that for all the modal images at different wavelengths from 550 nm to 900 nm, the light mostly distributes in the core of the structure and no light was observed at the end face of the cladding strands even for the wavelengths near the resonances of the cladding modes. To explain this, we should consider two facts: first, due to the large core diameter, the core mode overlaps very little with the cladding and couples to the cladding modes with low efficiency, which is also the reason for the limited depth of the dips in the

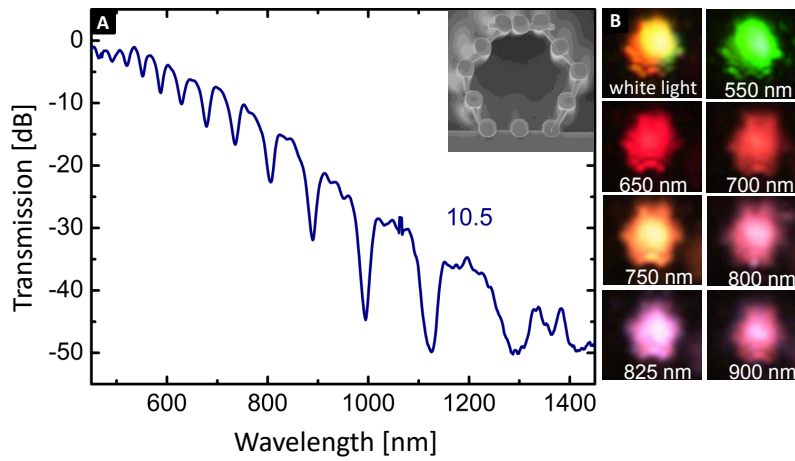


Fig. 4.14: (A) Transmission spectra of the “light cage” in a length of 10.5 mm. The inset shows the SEM image of the structure end face. The small peak around 1064 nm corresponds to the pump of the laser source. (B) The mode images at the output end face of the “light cage” structure for the broad band light source and for the filtered narrow band light sources centered at the wavelengths as labeled.

transmission spectra; second, the part of the light, which was coupled to the cladding from the core, may be too weak to see at the end of the structure due to the strong scattering loss of the cladding modes at every connecting points of the supporting struts as we observed in figure 4.15. Also the strand modes have high numerical aperture and may not be detect by our objective.

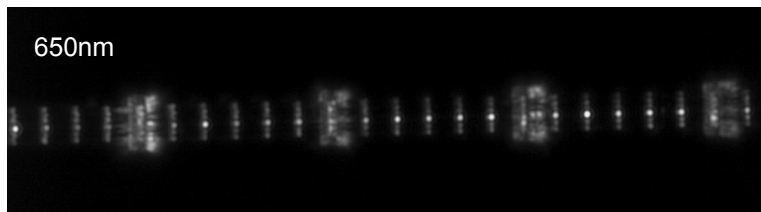


Fig. 4.15: Top view of a “light cage”, while the light of wavelength 650 nm propagates in it.

In figure 4.15, we showed the top view of the “light cage”. A CCD camera connected to a $12\times$ zoom lens system (Navitar) was mounted vertically above the sample. The picture was taken while the light of wavelength around 650 nm propagates in the light cage. We can see the supporting blocks below the structure. The struts appear as disconnected scattering points, which correspond to the connecting points of struts to the strands. This result shows

the scattering loss of the cladding modes at the connecting points in a “light cage” structure.

4.3 Conclusion

In this chapter, we presented two key results of our work regarding the novel hollow-core waveguides in this chapter.

In the first part, we proposed the design of a water-core all-solid band gap fiber claiming the possibility of light guidance in a water core surrounded by all-solid photonic band gap cladding. The reflection-based planar model was built for the proposed structure to calculate analytically the complex effective index of the fundamental mode in the water-core all-solid band gap fiber with much lower computation burden regarding the change of the core radius. It was shown that the results analytically calculated with the reflection parameters matched well with the results from the FEM simulation in case of the fundamental guided mode, especially for the large core (low loss) cases. The loss of the fundamental mode of the proposed fiber exhibits a reduction by a factor of about 45 compared with the loss of the mode in a water-filled silica capillary in the middle of the band gap region. Regarding the modal attenuation, we analyzed at the mid-gap frequency those geometry parameters of the structure, which do not affect the band gap: the core radius, the number of the rings in the cladding and the thickness of the silica wall around the core. Further, the analytical calculation based on the reflection parameters allows us to plot a loss map for the fundamental mode in a large core ($R=50\mu\text{m}$) covering all the feasible combinations of the structural parameters d/Λ of the band gap cladding and a range of frequencies. The loss map showed the band gap behavior together with the information of the modal losses for the fundamental modes, saving any further calculation to analyze the loss of the fundamental mode for any structures of the design in practice.

The all-solid band gap fiber with a core of index of water will be an ideal alternative waveguide compared with the large-core tube-type waveguides such as capillaries, Teflon based tubes or metal-coated tube waveguides, for that our design provided low attenuation of the guided light in a core of relative small diameters (a few tens of micrometers rather than millimeter in other cases) and proper outer diameter of the final fiber for straightforwardly integrating of the fiber into microfluidic chip-based devices. Our design of

key features: solid cladding and a single central channel, also surpasses the holey hollow core band gap fibers in the optofluidic applications to avoid undesired penetration of the liquid into the cladding channels, which leads to uncertainties in further optical characterization.

In the second part, hollow core “light cage” structures were constructed with polymer strands directly written by 3D laser writing on planar silicon substrates for guidance in an air-core. Analysis with simulations show that a “light cage” structure consisting of a single hexagonal ring of 12 polymer strands (refractive index: 1.52, diameter: $3\mu\text{m}$ and pitch: $7\mu\text{m}$) offer guidance in the central air-core based on a combined mechanism of anti-resonant and inhibited coupling in the wavelength range from 450 nm to 1550 nm. Structures, which consist of 12 polymer strands arranged in a hexagonal ring shape and connected by struts, were fabricated of different lengths and suspended on the silicon wafer with supporting blocks. The optical characterization of the resulting “light cage” structures exhibits guidance of light in the central air core for wavelength range from visible to near infra-red and transmission spectra with dips corresponding to the resonances of the low-order cladding modes. It was noticed that the guidance of the light has tolerance on the deviations of the pitch. Such one ring structure constructed by polymer strands can be regarded as one ring of an amorphous lattice operating in large pitch regime as in the cases of tube lattice anti-resonant fibers [98].

Further research on the applications of the light cage is promising. First, the light cage structures realized the guidance of the focused light in air without diffraction up to centimeters [97, 99]. Besides, the large pitch of the structure up to few micrometers opens a way for gas analytic to diffuse into the core of the waveguide fast and efficient [100–102]. A hollow core nearly fully filled with guided light and direct side access to the core via open spaces in the cladding are extraordinary features that make the light cage a promising choice for on-chip photonics applications regarding light-matter interaction, for example, quantum technology, ultra-fast spectroscopy, bioanalytics and nonlinear optics.

Instead of the core, the cladding of a band gap fiber can also work as a platform for light-matter interaction, eg. refractive index sensing. One way is to fill the channels in the cladding of a solid-core band gap fiber by liquids forming liquid-filled band gap (LFBG) fibers [103]. A LFBG fiber has cladding consisting of liquid strands arranged in hexagonal arrays. Its cladding modes, i.e. bands and band gaps, are susceptible to the refractive index of the filled liquids. Here, using the analytical method introduced in chapter 3.1, we related the variation in the refractive index of liquid filled in the cladding to the shift of the spectral position of the dips in the transmission spectrum of the LFBG fiber.

With LFBG fibers, it is possible to analyze the refractive index of the liquid using rather small volumes of liquids that are encapsulated from the environment, which avoids the difficulties in measuring the refractive index of liquids with low vapor pressure, being toxic or expensive. Besides, whereas the majority of the dielectric-based photonic refractive index sensors using propagating eigenwave operate only around 1500 nm [104], by using LFBG fibers that offer bands of cladding modes in a wide wavelength range, we were able to characterize the refractive index of the filled liquid from visible to infrared and retrieve its dispersion properties with one transmission measurement.

In this chapter, I first introduced our methods to fabricate the LFBG fibers and to determine the refractive index and its dispersion of the liquids from their transmission spectra. Then, I showed the applications of the method on: determination of the refractive index dispersion of a liquid mixture system of carbon disulphide (CS_2) solution and tetrachloroethylene (C_2Cl_4) solution; investigation of the temperature dependence of the refractive index of CS_2 solution, showing its thermo-optic coefficient in a wide wavelength range.

5.1 Method

The sensing with LFBG fibers is based on the fact that the spectral position of the phase matching between the cladding band and the fundamental core

mode ($n_{eff}^{cl} = n_{eff}^{co}$) matches that of the transmission dip. Therefore, the key idea is to obtain the phase matching points from the transmission dips and compare it with the calculated phase matching bands to determine the refractive index of the liquids in the cladding of LFBG fibers. The implementation of the sensing with LFBG fibers requires the fabrication of the LFBG fibers, optical characterization of their transmission properties and analysis of the refractive index of the filled liquids, which will be introduced in this section.

5.1.1 Fabrication of LFBG fibers

We fabricated LFBG fibers straightforwardly by filling the holes in commercial solid-core PCFs (LMA20 and LMA25, from Thorlabs) with the interested high index liquids: carbon disulphide (CS_2) solution ($\geq 99.9\%$, from Sigma-Aldrich) and tetrachloroethylene (C_2Cl_4) solution ($\geq 99\%$, from Sigma-Aldrich). The refractive index of CS_2 is around 1.6 [25, 105] and C_2Cl_4 is around 1.49 [106] at 900 nm .

We used silica based solid-core photonic crystal fibers with air channels in the cladding (LMA20 and LMA25 from Thorlabs), which are characterized with large core area and air holes in size of micrometers as shown by the SEM pictures in figure 5.1(b,c). We chose them to have a reasonable amount of dips in the transmission spectra with a better-defined spectral position. First, holes in the size of micrometers result in liquid strands in the size of micrometers, which support a reasonable amount of cladding modes leading to dips in the transmission spectra from visible to infrared. Figure 5.1(a) shows the number of modes for liquid strands of size as holes in LMA20 and LMA25 in silica regarding the refractive index of the liquids. Second, a large core with large pitches lead to bands of cladding modes with a narrow spectral widths due to the weak coupling between strands, especially near the cutoff line (the effective index of the core modes in case of a large core) [74]. This is visible in the example band map in figure 5.3 and leads to transmission dips with narrow spectral width. Besides, the uniform diameter of the holes in commercial PCFs is also relevant for the width of the bands.

The fabrication processes of the LFBG fibers includes two parts: filling liquids into the PCF and sealing the ends of the PCF.

The filling of the PCFs was done by capillary force. The fiber pieces were prepared in a length of around 10 cm using a commercial cleaver (ProCleave LD II, Northlab Photonics AB). The collapsing of the ends of the fiber pieces

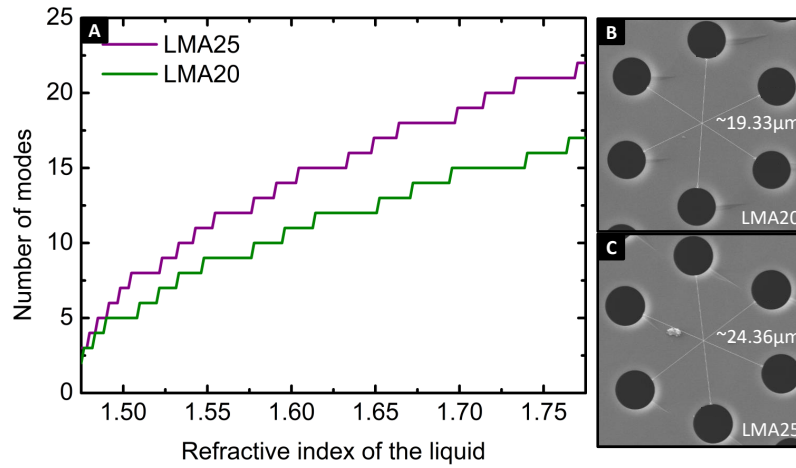


Fig. 5.1: (a) Plot of the number of modes of a liquid strand embedded in silica in the wavelength range from 500 nm to 2000 nm regarding the refractive index of the liquids, calculated with the geometry parameters of the holes in PCFs LMA20 and LMA25 (Thorlabs). (b,c) The SEM images of the PCFs we used: core dimension as labeled; radius of the strands, LMA20: $2.85\mu\text{m} \pm 0.03\mu\text{m}$, LMA25: $3.71\mu\text{m} \pm 0.06\mu\text{m}$; pitch, LMA20: $12.4\mu\text{m} \pm 0.12\mu\text{m}$, LMA25: $15.8\mu\text{m} \pm 0.18\mu\text{m}$.

was done by melting the silica with arc heating using a commercial splicer (FITELE S184 Fusion Splicer). The processing steps are described in detail here (figure 5.2):

- First, both ends of a fiber piece are cleaved to a length around 10 cm.
- Then, one end of the cleaved fiber piece is immersed into the liquid for a while until the sample is fully filled with liquid (for a length of around 10 cm it demands only a few seconds). Afterwards, the filled fiber piece is taken out and placed there for a moment for the liquid at the very end of the sample to evaporate resulting in an empty space of a length around 5 mm at the ends of the fiber piece.
- Finally, the fiber piece is fixed in the splicer to apply the arc power at the ends of the fiber piece (one end at a time). The arc power is adjusted so that by several times arc heating, the end of the fiber piece collapses to a silica block in a length of under $100\mu\text{m}$.

During the fabrication, it has to be noticed that: first, since the liquids used here are toxic and of low boiling point, the preparation of the liquids and filling of the samples need to be operated in the fume cupboard carefully; second, enough empty spaces at the ends of the filled fiber pieces are necessary to avoid the explosion of the liquids caused by the arc heating

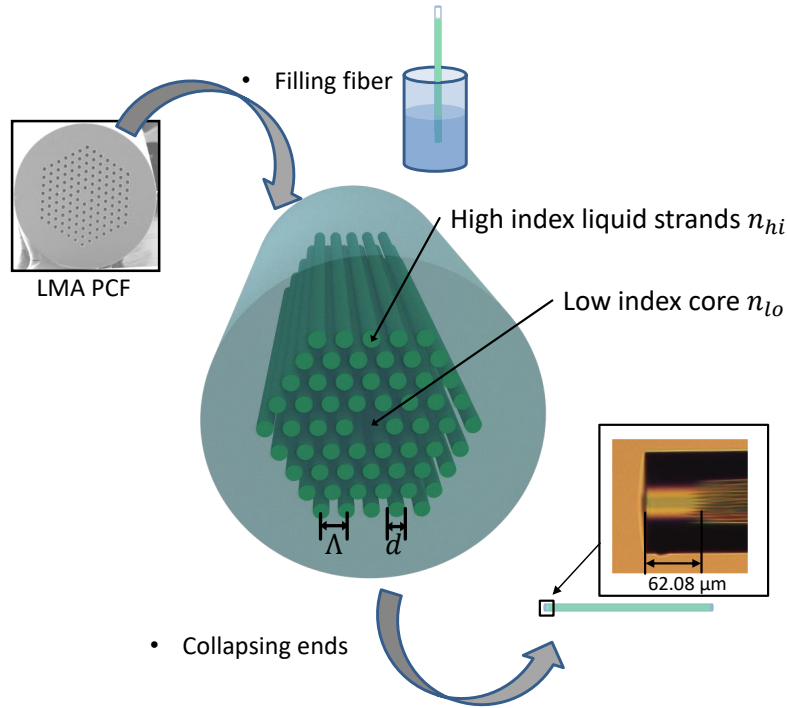


Fig. 5.2: Sketch for the fabrication of a LFBG fiber. The inset image shows the collapsed end of the fiber piece under a microscope.

during the collapsing; third, the arc power of the splicer should be adjusted to such amount that the collapsing length at the ends of the samples can be controlled to less than $100\mu\text{m}$ by the number of arcs. Still, due to inevitable evaporation of the liquids during the collapsing process, the end of the fiber pieces collapsed later will have a longer empty space.

The resulting filled fiber pieces were directly used in the transmission measurement with several noticeable features. First, the fiber pieces show sunk end faces due to the collapsing of the holly structured cladding. However, the end face of the core part will not be influenced by the collapsing since it is all solid. Second, a small amount of the liquids collect in the tips of the small empty cones at the end of the filled channels, which are separated to the liquid strands with a piece of empty space. After the measurements, a further collection of the liquids in the tips at the end and small nonconsecutive empty spaces along the filled channels may be found due to the evaporation and condensation of the liquids after heating.

5.1.2 Optical characterization and analysis of the refractive index

To measure the transmission spectra of the filled fiber pieces, a broad band light source (spectral range from 450 nm to 2400 nm, pump at 1064 nm, NKT SuperK COMPACT) was collimated, focused into the fiber piece with an objective (10x), while the output from the fiber piece was collected into an optical spectral analyzer (AQ-6315A, Ando) with a pair of objectives (10x) (figure 5.4).

To straightforwardly identify the cladding band phase matched to the fundamental core modes of a LFBG fiber with respect to different combinations of strands refractive index and wavelength, the phase matching band maps were calculated analytically using the binary functions, which were developed based on Birks' model (chapter 3.1), for the geometry of the LFBG fiber. They were calculated for a fixed effective index: $n_{eff} = n_{est}$, where n_{est} is the estimated effective index of the core modes, regarding the refractive index of the strands in the cladding n_{hi} and wavelength as shown in figure 5.3. The phase matching band maps relate the spectral positions of the cladding modes, which are phase matched to the fundamental modes, to the strands refractive index.

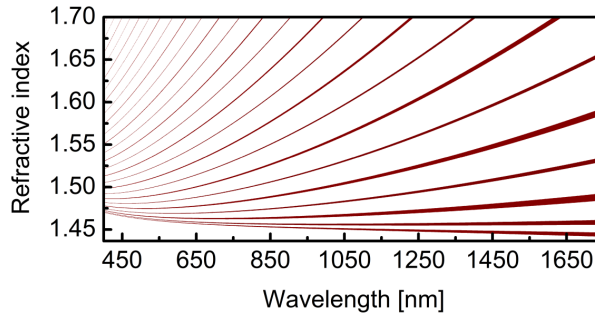


Fig. 5.3: Example of the phase matching band map with fixed effective index ($n_{eff} = n_{est}$) plotted for refractive index of the liquid filled in the strands (n_{hi}) regarding wavelengths. The plot here was calculated using the binary functions based on the Birks' model for the first two orders ($l = 0, 1$) and the geometry of the PCF LMA20. The red regions indicate the bands of the cladding.

The refractive index of the strands (n_{hi}) is determined by the bands in the phase matching band map that are of the spectral positions consistent with that of the dips in the transmission spectra of a LFBG fiber.

In figure 5.4(a), we show an example transmission spectrum of the fiber LMA20 filled with 100% CS_2 solution. We can see that the transmission spectrum exhibits pronounced transmission dips in the wavelength range from 450 nm to 1700 nm, whose widths broaden for longer wavelengths. The blue green drop lines indicate the spectral positions of the transmission dips, i.e. the phase matching points.

The spectral positions indicated by the transmission dips are used to determine the refractive index of the filled liquid in the calculated phase matching band map of the sample as shown in figure 5.4(b). The black line, indicating the dispersion of refractive index of CS_2 from the literature [25], crosses with the bands that supposed to be the corresponding bands for the transmission dips. As expected, the spectral positions of the transmission dips, shown by the blue green drop lines, are consistent with the crossing points determined by the refractive index from the literature.

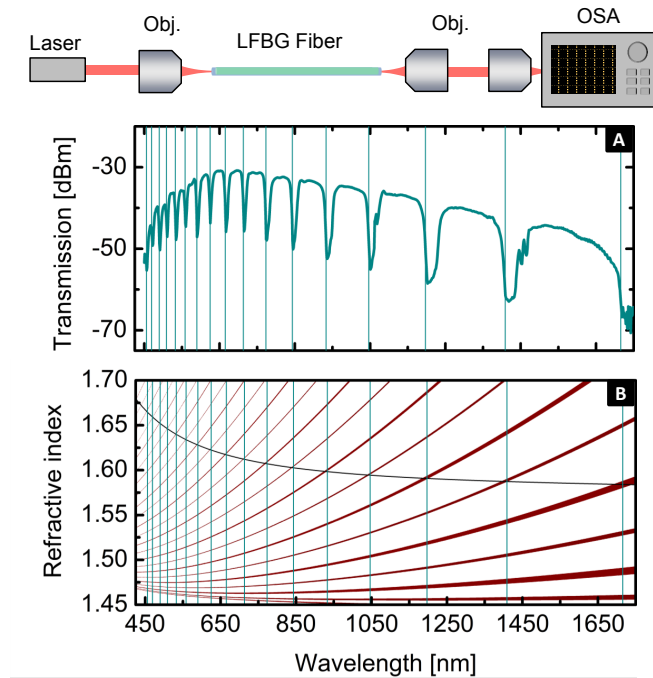


Fig. 5.4: Sketch of the setup for the transmission measurement of LFBG fiber. (A) an example transmission spectrum of the fiber LMA20 filled with 100% CS_2 solution; (B) corresponding phase matching bands (red regions) regarding refractive index of the liquids versus wavelengths and the plot (black line) of the dispersion of CS_2 from the literature[105]. The drop lines (blue green) correspond to the spectral positions of the dips defined by the local minimum of the first derivative of the spectrum showing the analyzing process.

It was tricky to define the spectral positions of the dips here. A close look

at those dips shows that the dips are not really in a symmetric shape, but a clean slope at short wavelength side and a gentle slope with sub-dips, which correspond likely to the higher order cladding modes, at long wavelength side. Therefore, we chose to locate the steepest slope at short wavelength side, which is reasonable to be considered as the coupling points of the core mode with the lower order cladding modes, as the position of the dips. To define the steepest slope of the down-slope of the dips, first, the baseline was extracted by applying a local maximum filter on the spectra and then subtracted from the spectra. In the end, we found the points of the steepest slope by calculating the first derivative of the spectrum, of which we defined the minimums as the spectral positions of each dip and showed them with drop lines in figure 5.4(a).

Another tricky point is to determine the refractive index from the bands indicated by the spectral position of the transmission dips. First, as we can see in figure 5.4(b), a spectral position (drop green line) corresponds to several bands in the phase matching band map. Therefore, an estimated refractive index range for the liquids is needed. For the mixture system, we found the corresponding band to be used to determine the refractive index of the liquid with the theoretical values either from the literature or from the calculation with a model for mixtures used in literature [107]. For example in figure 5.4(b), for fiber LMA20 filled with 100% CS_2 solution, the corresponding bands for the refractive index can be chosen by the black dispersion line. Then, we chose the value in the middle of the corresponding band as the refractive index of the liquid.

The effective index used for the calculation of the band map was the estimated effective index of the fundamental mode for the perfectly reflecting waveguide with the geometry and index of the liquid strands: $n_{est1} = \sqrt{n_{co}^2 - (j_{01}/(k_0 R))^2}$, where R and n_{co} is the radius and index of the core material, k_0 is the wave number and j_{01} is the first root of Bessel function J_0 . We tried also using its simplified expression $n_{est2} = n_{co} - j_{01}^2/(2k_0^2 R^2 n_{co})$, as well as just using the refractive index of the cladding matrix as the estimated effective index ($n_{est3} = n_{silica}$). Figure 5.5 shows the deviations from the reference of the resulting refractive index determined by the above described method with these three differently estimated effective indexes. We see that the results using full expression (n_{est1}) and the simplified expression (n_{est2}) as the estimated effective index are hard to distinguish from each other.

However, using simply the cladding matrix index (n_{est3}) leads to an obvious bias in the results from that of the other two methods, which increases for longer wavelengths.

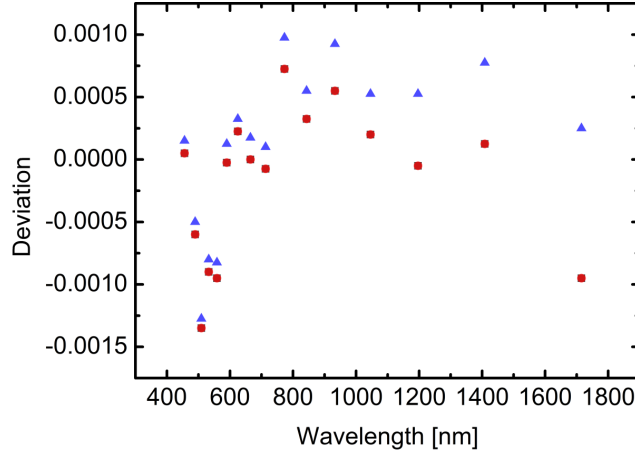


Fig. 5.5: Deviations from the reference of the refractive index of the liquids (100% CS_2 solution) determined from the LFBG fiber (LMA20). The results of different labels refer to methods with three differently estimated effective index for the calculation of the band map (black square: $n_{est1} = \sqrt{n_{co}^2 - ((j_1)/(k_0 R))^2}$; red dot: $n_{est2} = n_{co} - j_1^2/(2k_0^2 R^2 n_{co})$; blue triangle: $n_{est3} = n_{silica}$).

The reference of CS_2 and the results from the sample of the 100% CS_2 filled fiber LMA20 was used to characterize different analyzing methods. Considering the least root mean square error (RMSE) of the results from the reference, in the end, we used the first derivative method for the position of the dips, the full expression ($n_{est1} = \sqrt{n_{co}^2 - (j_{01}/(k_0 R))^2}$) as the estimated effective index and the value corresponding to the middle of the crossing band as the refractive index of the liquid in the PCF cladding.

5.2 Results

5.2.1 Refractive index of a bi-mixture system

The above described method was applied to determine the dispersion of the refractive index of the bi-mixtures system of carbon disulphide (CS_2) and tetrachloroethylene (C_2Cl_4) solutions in the wavelength range from 450 nm to 1700 nm. We prepared a series of liquids of refractive indexes above that of silica using the mixtures of two high index liquids, CS_2 and C_2Cl_4 , with different weight ratios: 0%, 25%, 50%, 75%, 100% of CS_2 . The dimensions of the structure of LMA20 and LMA25 PCFs measured in the SEM pictures

were corrected by a value in order of $0.1\mu\text{m}$ using the samples filled with 100 % CS_2 and 100 % C_2Cl_4 solutions respectively, to have the least root mean square error between the resulting data and their references [25, 106].

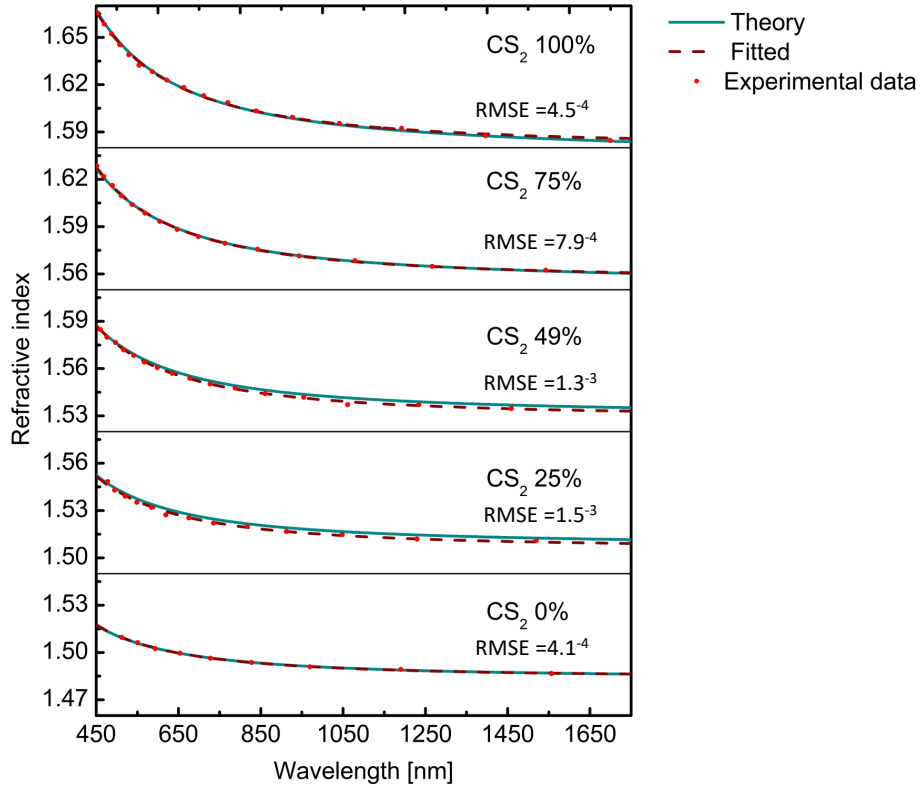


Fig. 5.6: Refractive index dispersions of liquids mixtures of CS_2 and C_2Cl_4 with a weight ratio of CS_2 around 100 %, 75 %, 49 %, 25 %, 0 % from top to bottom. The labels show the RMSE of the data from the theory reference. Dashed lines are the fittings for the experimental data using a single resonance Sellmeier equation.

The resulting refractive index determined for samples filled with bi-mixtures of different weight ratios are shown in figure 5.6. The data points we got from experiments (red dots) were fitted (dashed dark red line) and compared with the reference (blue green line). We can see that the dispersion of the refractive index of 100 % CS_2 and C_2Cl_4 solutions in a wide wavelength range from 450 nm to 1700 nm from the experimental data show a good match with the theory reference. The consistence of the experimental data with the theory reference is shown by the root mean square error (RMSE): 4.5×10^{-4} for CS_2 filled in LMA20 and 4.1×10^{-4} for C_2Cl_4 filled in LMA25, which confirms the validity of the method for dispersion determination.

Here, the reference dispersion of mixture was calculated using the estimated method for the refractive index of a bi-mixture without considering the

internal interaction among molecules in the solutions [107]. They were used only to narrow the range of the refractive index to the corresponding band at the wavelength of the transmission dips. The RMSE between the data of the mixtures and the reference is up to 10^{-3} , which is one order higher than the assumed error of the method. It shows that the estimated method used here to calculate the theory reference gives an error in the order of 10^{-4} to 10^{-3} . The mechanism behind this involving the internal interactions among the molecules is complex and also depends on the concentration ratios of two solutions. Since the error from our system is also in order of 10^{-4} , we would not investigate the deep mechanism of the internal interaction based on our measurement.

The fitting of the data points from experiments were done with a Sellmeier formula, which considers only one absorption resonance of the material for the wavelength range here, as shown in equation (5.1). The fitting parameters (a and b) and the standard deviation errors of the parameters are shown in table 5.1. The fittings here offer the continuous dispersion of the bi-mixture solutions for different concentrations (weight ratios of CS_2).

$$n = \sqrt{1 + \frac{a\lambda^2}{\lambda^2 - b}}, \quad (5.1)$$

where, b are related to the UV-resonance wavelength of the material as $b = \lambda_b^2$. λ is in unit of μm .

Tab. 5.1: Table of the fitting parameters for the Sellmeier equation (equation 5.1).

Concentration(CS_2)	a	a_{error}	b	b_{error}
100 %	1.49653	0.00119	0.03216	2.56079E-4
75 %	1.4204	5.57545E-4	0.02791	1.14512E-4
49 %	1.33998	6.22743E-4	0.025	1.49556E-4
25 %	1.26901	0.00138	0.02073	3.7882E-4
0 %	1.20115	4.38268E-4	0.01641	1.51425E-4

In figure 5.6, we see that the refractive index shifts with the concentration ratio of the bi-mixture system. Therefore, the parameters a and b in the equation (5.1) can also be expressed as a function of concentration. In figure 5.7, we plot the parameters a and b with respect to the concentration with linear fittings. It shows that the linear fit can predict the parameters quite

well with reasonable errors for the bi-mixture system here as proposed in the literature [107]. As a result, the bi-mixture system can be designed for a refractive index in a wide wavelength range from visible to infra-red using different concentration ratios of the liquids. The dependence of the refractive index on both wavelength and the concentration ratio of the liquid mixtures is shown with the following equation:

$$n = \sqrt{1 + \frac{a(c)\lambda^2}{\lambda^2 - b(c)}}, \quad (5.2)$$

where $a(c)$ and $b(c)$ are linear functions of concentrations of CS_2 with intercepts and slopes as shown in figure 5.7, λ is in unit of μm .

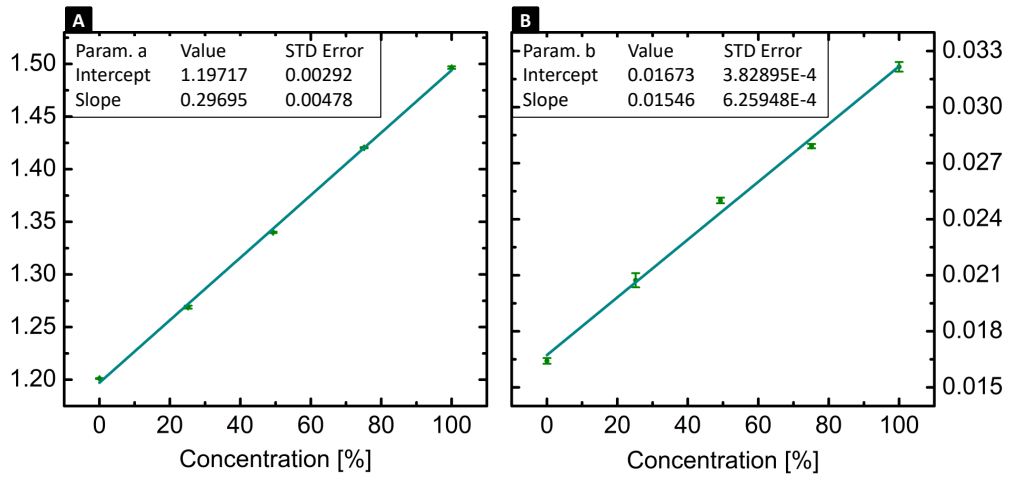


Fig. 5.7: Fitting parameters of the Sellmeier equation (5.1) regarding the concentrations (weight ratio of CS_2): (A) parameter a , (B) parameter b . The error bars correspond to the errors in table 5.1. The linear fitting data are shown in the insets.

In figure 5.8, we plotted the data from experiments (dots) at wavelength 600 nm and 800 nm to show the refractive index variations regarding the concentration ratios of the liquid mixture. We found that the refractive indexes of the liquids at one wavelength change approximately linearly with respect to the concentration of liquid CS_2 in the mixture. It was also noticed that the slope of the refractive index regarding concentration is different for these two wavelengths (around 0.12 at 600 nm and 0.11 at 800 nm).

With equation 5.2, we calculated the refractive index of the mixture at wavelength 600 nm and 800 nm for concentrations from 0 to 100 % (lines in figure 5.8). We can see that the calculated results are consistent with the

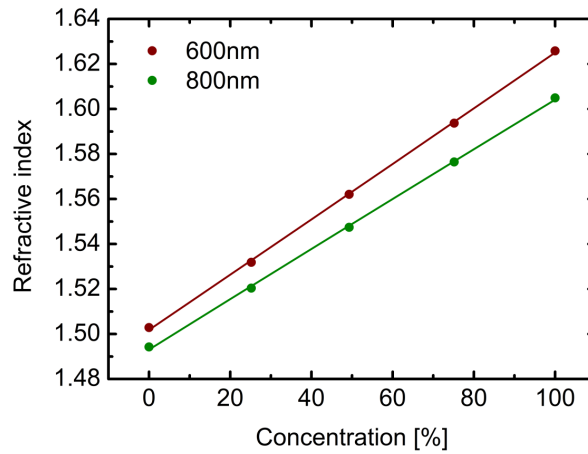


Fig. 5.8: Refractive index of the bi-mixture liquids at wavelengths 600 nm and 800 nm regarding the concentration (weight ratio of CS_2). The dots represent the experimental results and the lines are calculated with equation (5.2) for wavelength 600 nm and 800 nm with concentrations from 0 to 100 %.

experimental data and give continuous prediction of the refractive index regarding concentration changes.

5.2.2 Temperature dependence of refractive index

To demonstrate the capabilities of the method, we further obtained the refractive index dispersion of the liquid CS_2 at different temperatures and determined its thermo-optic coefficient (TOC) (around 30 °C) for a large wavelength range.

We heated the sample of LMA20 PCF filled with 100% CS_2 solution using Peltier effect. The sample was placed in the groove of a metal plate and covered with a piece of soft thermal conductive material, which was contacted with a Peltier element. By adjusting the voltage applied on the Peltier element, we changed the environmental temperature of the sample from 26 °C to 138 °C, which was monitored with a thermometer with type K/J thermocouple (resolution 0.1 °C).

The transmission spectra of the sample at different temperatures from 26 °C to 138 °C are shown in figure 5.9. We observed that the transmission dips shift to shorter wavelengths regarding the increasing temperature. It was also noticed that when the temperature is above 53 °C, more features as sub-dips appear in the spectra. For even higher temperatures (above 100 °C), the dips start to disappear and the spectrum is almost flat.

Since many liquids exhibit much higher temperature dependence of refrac-

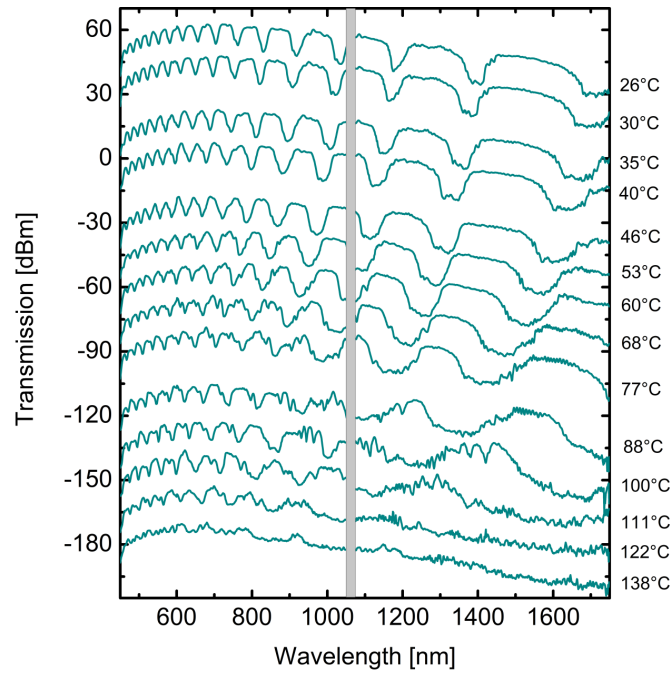


Fig. 5.9: Transmission spectra of the LMA20 PCF filled with CS_2 solution regarding different environmental temperatures. The gray bar covers the region of the laser pump. The y-axis label shows not the absolute values of the transmission for that the spectra were vertically shifted to be distributed in the same plane.

tive index (two orders of magnitude larger thermo-optic coefficient (TOC) than that of fused silica [108]), the changes in the spectra can be attributed to the changes of refractive index of the liquid regarding the thermal process. It is a rather complex thermal process for the liquid is encapsulated in a volume-conserved channel. As the temperature increases, the liquid expands until it fills up the container, during which the increased pressure inside the sealed channel prevents the boiling of the liquid even above its boiling temperature (around 46°C for CS_2 [109]). For such thermal process, a previous work about the liquid filled two-core fiber [105] has identified two operation regimes: in the first regime, the liquid is free to expand and the refractive index of liquid decreases significantly for increasing temperature even above the liquid's boiling point; in the second regime, no more space for liquid to expand and the refractive index of the liquid changes very little with increasing temperature. In figure 5.9, we can see that the spectra shift happened in the whole temperature range in our experiments, suggesting that in our heating process, we don't have the liquid fill up the fiber piece completely. In the process of increasing temperature, the refractive index

of the filled liquid decreases, leading to shifted transmission dips. When the refractive index of filled liquid is comparable to the refractive index of the silica background, the transmission dips from band gap effect disappear resulting in a flat transmission spectrum.

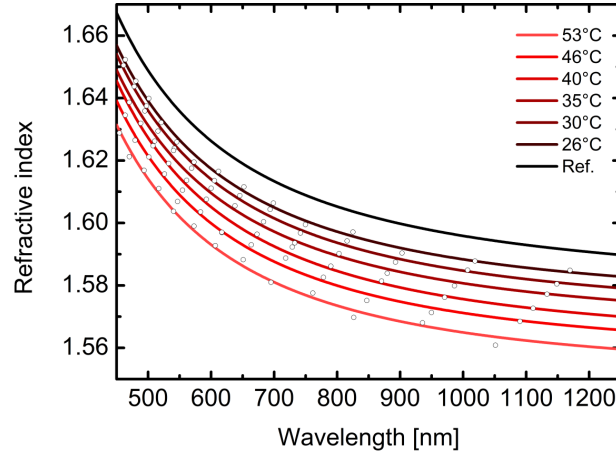


Fig. 5.10: Dispersion of the refractive index of CS_2 regarding different environmental temperatures. The circles are data calculated from the transmission dips in figure 5.9. The color lines correspond to the fits of the data with the Sellmeier equation (5.1). The black line is the reference data from the literature for the refractive index of CS_2 at room temperature (20 °C) [25].

For the environmental temperature of the sample was controlled to be stable at each point for a while, we can assume that what we measured is the temperature of the filled liquid. From the transmission spectra at these temperatures, we obtained the refractive index dispersion of the filled CS_2 for these temperatures using the analyzing method introduced in the last section. We used the transmission spectra at temperatures from 26 °C to 53 °C in the wavelength range from 450 nm to 1250 nm, where we see clear narrow dips, for the determination of the refractive index. To specify the bands for the case of 26 °C, we just shifted the reference dispersion of CS_2 , which is at the room temperature (20 °C) [25], with small steps (-10^{-3}) to lower values until the next band appears at the positions of the dips. Again, we defined the middle values at the crossing region of these bands as the results of the refractive indexes of CS_2 at 26 °C. Then we shifted the reference dispersion further for the bands of the next temperature and so on. The results of the refractive index at different temperatures are shown in figure 5.10. The dispersion lines of the refractive index in a broad wavelength range from 450 nm to 1250 nm at different temperatures were fitted from the data using

the Sellmeier equation (5.1).

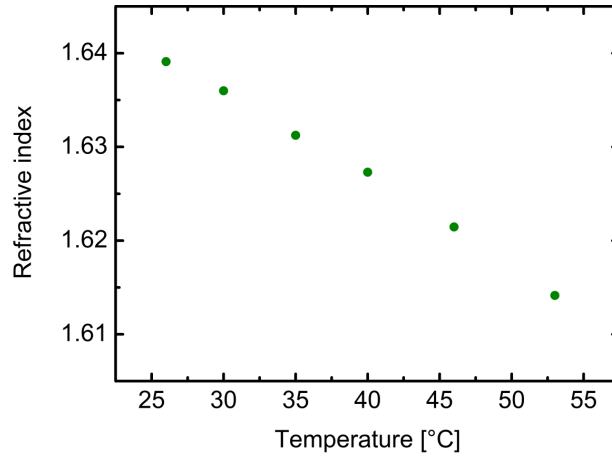


Fig. 5.11: Refractive index of CS_2 regarding temperature at wavelength 500 nm. The data is taken from the fittings in figure 5.10.

In figure 5.11, we plot the refractive index regarding temperature according to the dispersion lines at wavelength 500 nm. We can see that the dependence of the refractive index of CS_2 on temperature is not linear. This is reasonable because the dependence of the refractive index on temperature, the thermo-optic coefficient (TOC), is also a function of temperature (section 2.2.2).

We then analyzed the TOC of CS_2 in the case of our experiments by linear fitting of the data in a small temperature ranges (with data at temperature 26 °C, 30 °C, 35 °C, measured with an accuracy of about 0.1 °C) for all wavelengths in figure 5.10. The resulting TOC for around 30 °C regarding wavelength are plotted in figure 5.12. We can see that the TOC of CS_2 in our experiments at around 30 °C is of negative values in the measured wavelength range. In the wavelength range from 600 nm to 800 nm, the TOC at around 30 °C show a smaller value compared with the known TOC of CS_2 at room temperature (around $-8 \times 10^{-4} \text{ K}^{-1}$ at 20 °C [105, 110–112]). The dispersion of the TOC along the wavelength with decreasing slope is similar to the dispersion of the TOC for solid optical materials introduced in literature [73]. With our data, we have the dispersion of the TOC of CS_2 expanded from 800 nm to near infra-red compared with the latest related work [105].

The errors of the results are from the analyzing method to determine the refractive index of the liquid filled in the PCF, which is around 10^{-4} , as well as from the temperature measurement for the heating process with a

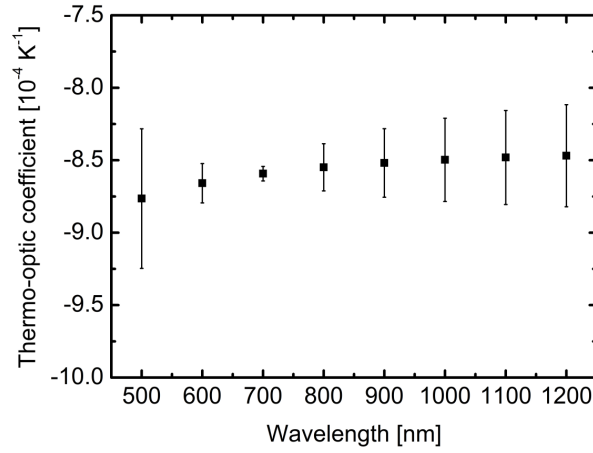


Fig. 5.12: Thermo-optic coefficient of CS_2 regarding wavelength at temperature around 30°C . The squares show the linear fitting coefficient for the data at temperature 26°C , 30°C , 35°C , while the error bars show the fitting standard errors.

thermometer in resolution of 0.1°C . Besides, a bias can be induced to the temperature data due to the direct heating of the sample by the light guided in the sample, which leads to a higher temperature of the liquid filled in the sample than the measured surrounding temperature.

5.3 Conclusion

In conclusion, by filling the solid-core PCF with high index liquids, we got a liquid-filled band gap (LFBG) fiber, whose transmission spectra reflects the optical properties of the liquid filled in the cladding. By analyzing the spectral positions of their transmission dips, we were able to determine the refractive index of the liquids filled in the LFBG fiber in a broad wavelength range using the analytical method introduced in the previous work (section 3.1). Specifically, we filled the commercial solid-core PCFs, LMA20 and LMA25 (Thorlab), with bi-mixtures of different weight ratios of CS_2 and C_2Cl_4 . We determined the refractive index of the filled liquids in the wavelength range from 450 nm to 1700 nm . By fitting the data, we offered an equation for the refractive index of the bi-mixture system of CS_2 and C_2Cl_4 regarding the mixture concentration ratios and wavelengths.

Further, with the sample of the LMA20 PCF filled with 100% CS_2 solution, we analyzed its transmission spectra at different environmental temperatures (from 26°C to 138°C). The dispersion of the refractive index of CS_2 at different temperatures was determined and fitted with one resonance Sellmeier

equation for the wavelength range from 450 nm to 1250 nm. As a result, we achieved data of the refractive index of CS_2 for a broad range of wavelengths at different temperatures. It allows us to study the change of the refractive index regarding temperature, the thermo-optic coefficient (TOC) and present the dispersion of the TOCs of CS_2 around 30 °C from visible to infra-red wavelength range.

The limitations of the methods lie on the facts: first, the band gap effect (transmission dips) of the LFBG fiber requires the filled liquid of a refractive index higher than that of silica; second, to get the absolute value of the refractive index with a high precision, the calibration of a LFBG fiber needs ready data from literature as reference. Despite these limitations, our method offers an easy way to get the refractive index of the liquids in a broad wavelength range: the data in a wavelength range from visible to infrared can be achieved with one transmission measurement. The precision of the results in order of 10^{-4} is comparable to the other delicate methods[104]. Besides, our method requires only a tiny amount of the liquids in an encapsulated environment and is especially suitable for those liquids with low vapor pressure or that are toxic or rare.

Our work on refractive index sensing with the LFBG fiber has also promising applications in the fields of spectral filters and non-linear optics. Based on the LFBG fiber with the bi-mixture system of liquids CS_2 and C_2Cl_4 of different concentration ratios, it is possible to adjust the transmission window of the fiber continuously. Otherwise, it is also possible to shift the transmission windows by changing the environmental temperature of the LFBG fiber. Moreover, close to the photonic band edge, the group velocity dispersion (GVD) of the guided core modes changes from normal to anomalous with a point of $GVD = 0$, which is important for nonlinear optics like super continuum generation [113]. By shifting the photonic bands of the LFBG fiber, it provides a novel way for dispersion engineering for nonlinear optics.

Microstructured fibers guide light with photonic properties based on their structured cladding, offering promising solutions for hollow core guidance. This study is set out to investigate the possibility of hollow core guidance with all-solid photonic crystal cladding, which consists of high index strands in periodic arrays embedded in a low index matrix. Two methods were developed here to study microstructured cladding from the perspective of their band gap maps, as well as their reflection and transmission.

We developed a complete analytical method using a binary function based on Birk's model to investigate the photonic band gap map of all-solid photonic crystal claddings. The method combined equations in Birks' model to a binary function and was proven very efficient to identify band gaps of photonic crystals for different parameter combinations. With the binary function, the calculation of photonic band gap map is straightforward and a parameter analysis with small variations shows that the fundamental band gap goes deeper to smaller effective index for the increasing of the geometry parameter d/Λ and the increasing of the material parameter n_{hi} with fixed n_{lo} . It appears that the guidance in a hollow core with such all-solid photonic crystal cladding would be difficult if not impossible due to the limited materials of high index that can be fabricated as strands in the cladding.

The guidance in an air core surrounded by suspended polymer strands in size of around $3\mu\text{m}$ in the wavelength range from visible to near infrared was shown theoretically with simulations and achieved experimentally. Such hollow core waveguide consisting of 12 polymer strands arranged in a hexagonal ring, of length to one centimeter, was implemented using 3D direct laser-writing on the silicon wafer. The optical characterization of such hollow core waveguide shows guidance in the central air core and transmission spectra with dips corresponding to the resonances of the low-order cladding modes. It appears that this waveguide guides light with a mechanism combining the band gap guidance with inhabited coupling guidance as the case of revolve AR fibers.

The analytical method using binary functions is so convenient that we apply it to determine the refractive index of the filled liquid in a liquid-filled band gap (LFBG) fiber. Specifically, we filled the commercial solid core PCFs, LMA20 and LMA25 (Thorlab), with bi-mixtures of different weight ratios of

CS_2 and C_2Cl_4 solutions. By analyzing the spectral position of the dips in their transmission spectra, we determined the refractive index of the filled liquids in the wavelength range from 450 nm to 1700 nm with an error of around 10^{-4} , leading to an equation for the refractive index of the bi-mixture system of CS_2 and C_2Cl_4 regarding the mixture concentration ratios and wavelengths. Besides, with the same method, we achieved data of the refractive index of CS_2 for a broad range of wavelengths at different temperatures. We studied the change of the refractive index regarding temperature, the thermo-optic coefficient (TOC), and presented the dispersion of the TOCs of CS_2 at temperature around 30 °C for wavelength from 450 nm to 1250 nm.

On the other hand, we introduced a reflection-based simulation method offering the possibility to qualitatively and quantitatively study the guidance in a large core microstructured fiber from the perspective of the reflection and transmission of its structured cladding. Specifically, we analyzed the fundamental core modes of an all-solid single-ring microstructured fiber, which has high index strands arranged in a ring form in low index matrix. We modeled the reflection from the structured cladding using an approximated planar model, which includes only a small part of the whole structure. We demonstrated that the power transmission in the planar model can be directly related to the loss of the guided modes based on the approximation of low loss. Moreover, the phase difference between the forward scattered field and the incident field in the planar model reflects the interference of the fields allowing for better insights into the underlying physics. The exact dispersion and loss of the fundamental fiber modes were calculated from the complex reflection coefficient in the planar model and confirmed by the results from the corresponding numerical mode calculation. Ultimately, we did intensive parameters sweep for the all-solid single-ring microstructured fiber as well as its cylinder-modified version with cylinders of alternating diameters. We found structure arrangements allowing for ultralow loss and revealed the destructive interference after the structured cladding for the case of low loss.

We proposed the design of a water-core all-solid band gap fiber claiming the possibility of light guidance in a water core surrounded by all-solid photonic band gap cladding. The modal properties of the proposed fiber were analyzed using the reflection-based planar model for its complex effective index. It was shown that the results analytically calculated with the reflection parameters from the planar model matched well with the results

from the modal simulation with finite element method (FEM) in case of the fundamental guided mode, especially for the large core (low loss) cases. For higher order modes, the hexagonal shape of the core makes the planar model unrealistic to the TE-polarized mode leading to considerable discrepancy between the results from the reflection model with TE-polarized incidence and the results from the FEM simulation for TE_{01} mode. Regarding the modal attenuation, we analyzed at the mid-gap frequency those geometry parameters of the structure, which would not affect the band gap: the core radius, the number of the rings in the cladding and the thickness of the silica wall around the core. Further, the analytical calculation based on the reflection parameters makes it rather easy for us to plot a loss map for the fundamental mode in a large core ($R=50\mu\text{m}$) covering all the feasible combinations of the structural parameter d/Λ of the band gap cladding and a range of frequencies. The loss map showed the band gap behavior together with the information of the modal attenuation for the fundamental mode, saving any further calculation to analyze the loss of the fundamental mode for any structures of the design in practice.

The validity of the reflection-based planar model should be noticed: first, a large core compared to the wavelength and the cladding structure is essential; second, the core shape is influential depending on the polarization of the modes. The advantage of the method relies on that it relates the calculation of the core modes analytically to the simulation results of the cladding part, which is of a greatly reduced dimension, leading to much lower computation burden for achieving the complex effective index of the fundamental mode and a straightforward analytical calculation regarding the change of the core radius.

The reflection-based planar model was approved as practical and efficient for analyzing guidance in a large core microstructured fiber. While the concept of photonic band gap effect based on the coupling and forming of super-modes in the cladding is more about ideal periodic structures extended into infinite, the reflection and transmission analysis is more practical to be used in cases with finite periodic structures and modified periodic structures. Specifically, the reflection-based planar model exhibits properties most suitable for the studying of a hollow-core all-solid microstructured fiber, for it is valid for analyzing the band gap structure with high index contrast, which is not possible with the analytical methods based on Birks' model but essential

for a deep band gap into low index region; it is also validated for the case of microstructured cladding with modified periodicity rather than hexagonal periodicity; moreover, it allows the fast calculation of the core modes in a large core of radius on scale of hundred micrometers, which is the normal case for the hollow core guidance but will be very time-consuming with the FEM simulation.

For future work, we would like to continue to pursue hollow core guidance with key features: solid structured cladding and a single central channel, for it has obvious guidance advantages over capillaries and also surpasses the holey hollow core band gap fibers in the optofluidic applications to avoid undesired penetration of the liquid into the cladding channels. A further version of our concept to be investigated using the reflection-based planar model will be all-solid microstructured cladding with various modifications in the periodicity offering low loss guidance in a center water/air core. Such design is of great relevance for the sophisticated research fields studying light-matter interactions and will find applications in bioanalytic, quantum gas and lasers.

Bibliography

- [1] M. E. Lines. „The search for very low loss fiber-optic materials“. In: *Science* 226.4675 (1984), pp. 663–668 (cit. on p. 1).
- [2] J. B. MacChesney and D. J. DiGiovanni. „Materials development of optical fiber“. In: *Journal of the American Ceramic Society* 73.12 (1990), pp. 3537–3556 (cit. on p. 1).
- [3] G. Keiser. „Optical fiber communications“. In: *Wiley encyclopedia of telecommunications* (2003) (cit. on p. 1).
- [4] G. A. Thomas, B. I. Shraiman, P. F. Glodis, and M. J. Stephen. „Towards the clarity limit in optical fibre“. In: *Nature* 404.6775 (2000), pp. 262–264 (cit. on p. 1).
- [5] R. R. Alfano and S. L. Shapiro. „Observation of self-phase modulation and small-scale filaments in crystals and glasses“. In: *Physical Review Letters* 24.11 (1970), p. 592 (cit. on p. 1).
- [6] K. Q. Kieu and M. Mansuripur. „Biconical fiber taper sensors“. In: *IEEE Photonics Technology Letters* 18.21 (2006), pp. 2239–2241 (cit. on p. 1).
- [7] K. A. Willets and R. P. Van Duyne. „Localized surface plasmon resonance spectroscopy and sensing“. In: *Annual Review of Physical Chemistry* 58 (2007), pp. 267–297 (cit. on p. 1).
- [8] E. Yablonovitch. „Inhibited spontaneous emission in solid-state physics and electronics“. In: *Physical Review Letters* 58.20 (1987), p. 2059 (cit. on p. 2).
- [9] S. John. „Strong localization of photons in certain disordered dielectric superlattices“. In: *Physical Review Letters* 58.23 (1987), p. 2486 (cit. on p. 2).
- [10] O. Painter, R. K. Lee, A. Scherer, et al. „Two-dimensional photonic band-gap defect mode laser“. In: *Science* 284.5421 (1999), pp. 1819–1821 (cit. on p. 2).
- [11] L. I. Halaoui, N. M. Abrams, and T. E. Mallouk. „Increasing the conversion efficiency of dye-sensitized TiO₂ photoelectrochemical cells by coupling to photonic crystals“. In: *The Journal of Physical Chemistry B* 109.13 (2005), pp. 6334–6342 (cit. on p. 2).

- [12] P. Bermel, C. Luo, L. Zeng, L. C. Kimerling, and J. D. Joannopoulos. „Improving thin-film crystalline silicon solar cell efficiencies with photonic crystals“. In: *Optics Express* 15.25 (2007), pp. 16986–17000 (cit. on p. 2).
- [13] M. F. Yanik, S. Fan, M. Soljačić, and J. D. Joannopoulos. „All-optical transistor action with bistable switching in a photonic crystal cross-waveguide geometry“. In: *Optics Letters* 28.24 (2003), pp. 2506–2508 (cit. on p. 2).
- [14] J. D. Joannopoulos, G. Steven Johnson, J. N. Winn, and R. D. Meade. *Photonic crystals: molding the flow of light*. Princeton university press, 2008 (cit. on pp. 2, 13).
- [15] M. Fox. *Optical properties of solids*. 2002 (cit. on pp. 2, 13).
- [16] J. C. Knight, T. A. Birks, P. St. J. Russell, and D. M. Atkin. „All-silica single-mode optical fiber with photonic crystal cladding“. In: *Optics Letters* 21.19 (1996), pp. 1547–1549 (cit. on p. 3).
- [17] J. C. Knight. „Photonic crystal fibres“. In: *Nature* 424.6950 (2003), pp. 847–851 (cit. on p. 3).
- [18] P. St. J. Russell. „Photonic crystal fibers“. In: *Science* 299.5605 (2003), pp. 358–362 (cit. on p. 3).
- [19] V. R. K. Kumar, A. K. George, W.H. Reeves, et al. „Extruded soft glass photonic crystal fiber for ultrabroad supercontinuum generation“. In: *Optics Express* 10.25 (2002), pp. 1520–1525 (cit. on p. 3).
- [20] C. M. B Cordeiro, A. K. L. Ng, and H. Ebendorff-Heidepriem. „Ultra-simplified single-step fabrication of microstructured optical fiber“. In: *Scientific Reports* 10.1 (2020), pp. 1–12 (cit. on p. 3).
- [21] B. Temelkuran, S. D. Hart, G. Benoit, J. D. Joannopoulos, and Y. Fink. „Wavelength-scalable hollow optical fibres with large photonic bandgaps for CO₂ laser transmission“. In: *Nature* 420.6916 (2002), pp. 650–653 (cit. on pp. 3, 5, 6).
- [22] F. Du, Y. Lu, and S. Wu. „Electrically tunable liquid-crystal photonic crystal fiber“. In: *Applied Physics Letters* 85.12 (2004), pp. 2181–2183 (cit. on p. 3).
- [23] H. K. Tyagi, M. A. Schmidt, L. P. Sempere, and P. St. J. Russell. „Optical properties of photonic crystal fiber with integral micron-sized Ge wire“. In: *Optics Express* 16.22 (2008), pp. 17227–17236 (cit. on p. 3).
- [24] N. Granzow, P. Uebel, M. A. Schmidt, et al. „Bandgap guidance in hybrid chalcogenide–silica photonic crystal fibers“. In: *Optics Letters* 36.13 (2011), pp. 2432–2434 (cit. on pp. 3, 56).
- [25] M. Chemnitz, M. Gebhardt, C. Gaida, et al. „Hybrid soliton dynamics in liquid-core fibres“. In: *Nature Communications* 8.1 (2017), pp. 1–11 (cit. on pp. 3, 78, 82, 85, 90).

- [26] C. Martelli, J. Canning, N. Groothoff, and K. Lyytikainen. „Strain and temperature characterization of photonic crystal fiber Bragg gratings“. In: *Optics Letters* 30.14 (2005), pp. 1785–1787 (cit. on p. 3).
- [27] S. C. Warren-Smith, H. Ebendorff-Heidepriem, T. C. Foo, et al. „Exposed-core microstructured optical fibers for real-time fluorescence sensing“. In: *Optics Express* 17.21 (2009), pp. 18533–18542 (cit. on p. 3).
- [28] B. Doherty, M. Thiele, S. Warren-Smith, et al. „Plasmonic nanoparticle-functionalized exposed-core fiber—An optofluidic refractive index sensing platform“. In: *Optics Letters* 42.21 (2017), pp. 4395–4398 (cit. on p. 3).
- [29] T. A. Birks, J. C. Knight, and P. St. J. Russell. „Endlessly single-mode photonic crystal fiber“. In: *Optics Letters* 22.13 (1997), pp. 961–963 (cit. on p. 4).
- [30] J. C. Knight, T.A. Birks, R. F. Cregan, P. St. J. Russell, and P. D. De Sandro. „Large mode area photonic crystal fibre“. In: *Electronics Letters* 34.13 (1998), pp. 1347–1348 (cit. on p. 4).
- [31] A. Ferrando, E. Silvestre, J. J. Miret, and P. Andres. „Nearly zero ultraflattened dispersion in photonic crystal fibers“. In: *Optics Letters* 25.11 (2000), pp. 790–792 (cit. on p. 4).
- [32] D. Mogilevtsev, T. A. Birks, and P. St. J. Russell. „Group-velocity dispersion in photonic crystal fibers“. In: *Optics Letters* 23.21 (1998), pp. 1662–1664 (cit. on p. 4).
- [33] J. K. Ranka, R. S. Windeler, and A. J. Stentz. „Visible continuum generation in air–silica microstructure optical fibers with anomalous dispersion at 800 nm“. In: *Optics Letters* 25.1 (2000), pp. 25–27 (cit. on p. 4).
- [34] D. V. Skryabin, F. Luan, J. C. Knight, and P. St. J. Russell. „Soliton self-frequency shift cancellation in photonic crystal fibers“. In: *Science* 301.5640 (2003), pp. 1705–1708 (cit. on p. 4).
- [35] J. Limpert, T. Schreiber, S. Nolte, et al. „High-power air-clad large-mode-area photonic crystal fiber laser“. In: *Optics Express* 11.7 (2003), pp. 818–823 (cit. on p. 4).
- [36] W. J. Wadsworth, N. Joly, J. C. Knight, et al. „Supercontinuum and four-wave mixing with Q-switched pulses in endlessly single-mode photonic crystal fibres“. In: *Optics Express* 12.2 (2004), pp. 299–309 (cit. on p. 4).
- [37] J. M. Dudley, G. Genty, and S. Coen. „Supercontinuum generation in photonic crystal fiber“. In: *Reviews of Modern Physics* 78.4 (2006), p. 1135 (cit. on p. 4).
- [38] R. F. Cregan, B. J. Mangan, J. C. Knight, et al. „Single-mode photonic band gap guidance of light in air“. In: *Science* 285.5433 (1999), pp. 1537–1539 (cit. on pp. 4, 5, 56).

- [39] B. J. Mangan, L. Farr, A. Langford, et al. „Low loss (1.7 dB/km) hollow core photonic bandgap fiber“. In: *Optical Fiber Communication Conference*. Optical Society of America. 2004, PD24 (cit. on p. 4).
- [40] F. Luan, A. K. George, T. D. Hedley, et al. „All-solid photonic bandgap fiber“. In: *Optics Letters* 29.20 (2004), pp. 2369–2371 (cit. on pp. 4, 7).
- [41] A. Argyros, T. A. Birks, S. G. Leon-Saval, et al. „Photonic bandgap with an index step of one percent“. In: *Optics Express* 13.1 (2005), pp. 309–314 (cit. on pp. 4, 7).
- [42] F. Couny, F. Benabid, P. J. Roberts, M. T. Burnett, and S. A. Maier. „Identification of Bloch-modes in hollow-core photonic crystal fiber cladding“. In: *Optics Express* 15.2 (2007), pp. 325–338 (cit. on p. 4).
- [43] P. Yeh, A. Yariv, and E. Marom. „Theory of Bragg fiber*“. In: *Journal of the Optical Society of America* 68.9 (1978), pp. 1196–1201 (cit. on p. 5).
- [44] Y. Fink, J. N. Winn, S. Fan, et al. „A dielectric omnidirectional reflector“. In: *Science* 282.5394 (1998), pp. 1679–1682 (cit. on p. 5).
- [45] D. Torres, O. Weisberg, G. Shapira, et al. „OmniGuide photonic bandgap fibers for flexible delivery of CO2 laser energy for laryngeal and airway surgery“. In: *Photonic Therapeutics and Diagnostics*. Vol. 5686. International Society for Optics and Photonics. 2005, pp. 310–321 (cit. on p. 5).
- [46] T. A. Birks, P. J. Roberts, P. St. J. Russell, D. M. Atkin, and T. J. Shepherd. „Full 2-D photonic bandgaps in silica/air structures“. In: *Electronics Letters* 31.22 (1995), pp. 1941–1943 (cit. on p. 5).
- [47] P. J. Roberts, F. Couny, H. Sabert, et al. „Ultimate low loss of hollow-core photonic crystal fibres“. In: *Optics Express* 13.1 (2005), pp. 236–244 (cit. on pp. 5, 6, 58).
- [48] T. D. Hedley, D. M. Bird, F. Benabid, J. C. Knight, and P. St. J. Russell. „Modelling of a novel hollow-core photonic crystal fibre“. In: *Quantum Electronics and Laser Science Conference*. Optical Society of America. 2003, QTuL4 (cit. on p. 5).
- [49] F. Couny, F. Benabid, and P. S. Light. „Large-pitch kagome-structured hollow-core photonic crystal fiber“. In: *Optics Letters* 31.24 (2006), pp. 3574–3576 (cit. on pp. 5, 56).
- [50] A. Argyros and J. Pla. „Hollow-core polymer fibres with a kagome lattice: potential for transmission in the infrared“. In: *Optics Express* 15.12 (2007), pp. 7713–7719 (cit. on p. 5).
- [51] F. Benabid, J. C. Knight, G. Antonopoulos, and P. St. J. Russell. „Stimulated Raman scattering in hydrogen-filled hollow-core photonic crystal fiber“. In: *Science* 298.5592 (2002), pp. 399–402 (cit. on p. 5).

- [52] F. Couny, F. Benabid, P. J. Roberts, P. S. Light, and M. G. Raymer. „Generation and photonic guidance of multi-octave optical-frequency combs“. In: *Science* 318.5853 (2007), pp. 1118–1121 (cit. on pp. 5, 69).
- [53] P. St. J. Russell, P. Hölzer, W. Chang, A. Abdolvand, and J. C. Travers. „Hollow-core photonic crystal fibres for gas-based nonlinear optics“. In: *Nature Photonics* 8.4 (2014), pp. 278–286 (cit. on p. 5).
- [54] S. Février, B. Beaudou, and P. Viale. „Understanding origin of loss in large pitch hollow-core photonic crystal fibers and their design simplification“. In: *Optics Express* 18.5 (2010), pp. 5142–5150 (cit. on p. 6).
- [55] F. Gérôme, R. Jamier, J. L. Auguste, G. Humbert, and J. M. Blondy. „Simplified hollow-core photonic crystal fiber“. In: *Optics Letters* 35.8 (2010), pp. 1157–1159 (cit. on p. 6).
- [56] A. Hartung, J. Kobelke, A. Schwuchow, et al. „Double antiresonant hollow core fiber–guidance in the deep ultraviolet by modified tunneling leaky modes“. In: *Optics Express* 22.16 (2014), pp. 19131–19140 (cit. on p. 6).
- [57] N. M. Litchinitser, A. K. Abeeluck, C. Headley, and B. J. Eggleton. „Antiresonant reflecting photonic crystal optical waveguides“. In: *Optics Letters* 27.18 (2002), pp. 1592–1594 (cit. on pp. 6, 69).
- [58] N. M. Litchinitser, S. C. Dunn, B. Usner, et al. „Resonances in microstructured optical waveguides“. In: *Optics Express* 11.10 (2003), pp. 1243–1251 (cit. on p. 6).
- [59] Y. Wang, N. V. Wheeler, F. Couny, P. J. Roberts, and F. Benabid. „Low loss broadband transmission in hypocycloid-core Kagome hollow-core photonic crystal fiber“. In: *Optics Letters* 36.5 (2011), pp. 669–671 (cit. on p. 6).
- [60] B. Debord, M. Alharbi, T. Bradley, et al. „Hypocycloid-shaped hollow-core photonic crystal fiber Part I: Arc curvature effect on confinement loss“. In: *Optics Express* 21.23 (2013), pp. 28597–28608 (cit. on p. 6).
- [61] M. Alharbi, T. Bradley, B. Debord, et al. „Hypocycloid-shaped hollow-core photonic crystal fiber Part II: Cladding effect on confinement and bend loss“. In: *Optics Express* 21.23 (2013), pp. 28609–28616 (cit. on p. 6).
- [62] F. Poletti. „Nested antiresonant nodeless hollow core fiber“. In: *Optics Express* 22.20 (2014), pp. 23807–23828 (cit. on p. 6).
- [63] F. Yu and J. C. Knight. „Negative curvature hollow-core optical fiber“. In: *IEEE Journal of Selected Topics in Quantum Electronics* 22.2 (2016), pp. 146–155 (cit. on p. 6).
- [64] B. Debord, A. Amsanpally, M. Chafer, et al. „Ultralow transmission loss in inhibited-coupling guiding hollow fibers“. In: *Optica* 4.2 (2017), pp. 209–217 (cit. on p. 6).

- [65] S. Gao, Y. Wang, W. Ding, et al. „Hollow-core conjoined-tube negative-curvature fibre with ultralow loss“. In: *Nature Communications* 9.1 (2018), p. 2828 (cit. on p. 6).
- [66] S. Gao, Y. Wang, W. Ding, Y. Hong, and P. Wang. „Conquering the Rayleigh scattering limit of silica glass fiber at visible wavelengths with a hollow-core fiber approach“. In: *Laser & Photonics Reviews* 14.1 (2020), p. 1900241 (cit. on p. 6).
- [67] H. Sakr, Y. Chen, G. T. Jasion, et al. „Hollow core optical fibres with comparable attenuation to silica fibres between 600 and 1100 nm“. In: *Nature Communications* 11.1 (2020), pp. 1–10 (cit. on p. 6).
- [68] F. Yu, W. J. Wadsworth, and J. C. Knight. „Low loss silica hollow core fibers for 3–4 μm spectral region“. In: *Optics Express* 20.10 (2012), pp. 11153–11158 (cit. on p. 6).
- [69] A. N. Kolyadin, A. F. Kosolapov, A. D. Pryamikov, et al. „Light transmission in negative curvature hollow core fiber in extremely high material loss region“. In: *Optics Express* 21.8 (2013), pp. 9514–9519 (cit. on p. 6).
- [70] A. W. Snyder and J. D. Love. *Optical Waveguide Theory*. Chapman and Hall Ltd, 1983 (cit. on p. 9).
- [71] F. Zolla and et al. *Foundations of Photonic Crystal Fibers*. Imperial College Press, 2012 (cit. on pp. 9, 24, 27).
- [72] G. Ghosh. „Sellmeier coefficients and dispersion of thermo-optic coefficients for some optical glasses“. In: *Applied Optics* 36.7 (1997), pp. 1540–1546 (cit. on p. 15).
- [73] E. D. Palik. *Handbook of optical constants of solids*. Vol. V. Academic press, 1997, pp. 115–261 (cit. on pp. 15, 91).
- [74] T. A. Birks, G. J. Pearce, and D. M. Bird. „Approximate band structure calculation for photonic bandgap fibres“. In: *Optics Express* 14.20 (2006), pp. 9483–9490 (cit. on pp. 19, 20, 22, 33, 34, 36, 39, 78).
- [75] T. A. Birks, F. Luan, G. J. Pearce, et al. „Bend loss in all-solid bandgap fibres“. In: *Optics Express* 14.12 (2006), pp. 5688–5698 (cit. on pp. 24, 69).
- [76] M. Zeisberger and M. A. Schmidt. „Analytic model for the complex effective index of the leaky modes of tube-type anti-resonant hollow core fibers“. In: *Scientific Reports* 7.1 (2017), pp. 1–13 (cit. on pp. 24, 43, 63).
- [77] S. G. Johnson and J. D. Joannopoulos. „Block-iterative frequency-domain methods for Maxwell’s equations in a planewave basis“. In: *Optics Express* 8.3 (2001), pp. 173–190 (cit. on p. 27).

- [78] J. M. Pottage, D. M. Bird, T. D. Hedley, et al. „Robust photonic band gaps for hollow core guidance in PCF made from high index glass“. In: *Optics Express* 11.22 (2003), pp. 2854–2861 (cit. on p. 28).
- [79] R. Spittel, H. Bartelt, and M. A. Schmidt. „A semi-analytical model for the approximation of plasmonic bands in arrays of metal wires in photonic crystal fibers“. In: *Optics Express* 22.10 (2014), pp. 11741–11753 (cit. on p. 28).
- [80] T. P. White, B. T. Kuhlmeiy, R. C. McPhedran, et al. „Multipole method for microstructured optical fibers. I. Formulation“. In: *JOSA B* 19.10 (2002), pp. 2322–2330 (cit. on p. 29).
- [81] B. T. Kuhlmeiy, T. P. White, G. Renversez, et al. „Multipole method for microstructured optical fibers. II. Implementation and results“. In: *JOSA B* 19.10 (2002), pp. 2331–2340 (cit. on p. 29).
- [82] G. Li and M. A. Schmidt. „Identification of zero density of states domains in band gap fibers using a single binary function“. In: *Optics Express* 24.14 (2016), pp. 16212–16221 (cit. on p. 34).
- [83] B. E. A. Saleh and M. C. Teich. *Fundamentals of Photonics*. John Wiley and Sons, 1991 (cit. on p. 37).
- [84] E. Istrate and E. H. Sargent. „Photonic crystal waveguide analysis using interface boundary conditions“. In: *IEEE Journal of Quantum Electronics* 41.3 (2005), pp. 461–467 (cit. on p. 43).
- [85] P. Blown, C. Fisher, F. J. Lawrence, N. Gutman, and C. M. de Sterke. „Semi-analytic method for slow light photonic crystal waveguide design“. In: *Photonics and Nanostructures-Fundamentals and Applications* 10.4 (2012), pp. 478–484 (cit. on p. 43).
- [86] J. P. Yehouessi, O. Vanvincq, A. Cassez, et al. „Extreme large mode area in single-mode pixelated Bragg fiber“. In: *Optics Express* 24.5 (2016), pp. 4761–4770 (cit. on p. 44).
- [87] O. Vanvincq, J. P. Yehouessi, G. Bouwmans, L. Bigot, and Y. Quiquempois. „Pixelated Bragg fibers: bandgap guiding, generalized half-wave stack condition, and application to large mode area fibers“. In: *JOSA B* 32.9 (2015), pp. 1986–1992 (cit. on p. 51).
- [88] S. Wang, C. Jain, L. Wondraczek, et al. „Non-Newtonian flow of an ultralow-melting chalcogenide liquid in strongly confined geometry“. In: *Applied Physics Letters* 106.20 (2015), p. 201908 (cit. on p. 56).
- [89] S. Xie, F. Tani, J. C. Travers, et al. „As₂S₃/silica double-nanospike waveguide for mid-infrared supercontinuum generation“. In: *Optics Letters* 39.17 (2014), pp. 5216–5219 (cit. on p. 56).

- [90] K. F. Lee, N. Granzow, M. A. Schmidt, et al. „Midinfrared frequency combs from coherent supercontinuum in chalcogenide and optical parametric oscillation“. In: *Optics Letters* 39.7 (2014), pp. 2056–2059 (cit. on p. 56).
- [91] N. Granzow, M. A. Schmidt, W. Chang, et al. „Mid-infrared supercontinuum generation in As₂S₃-silica “nano-spike” step-index waveguide“. In: *Optics Express* 21.9 (2013), pp. 10969–10977 (cit. on p. 56).
- [92] C. M. Smith, N. Venkataraman, M. T. Gallagher, et al. „Low-loss hollow-core silica/air photonic bandgap fibre“. In: *Nature* 424.6949 (2003), pp. 657–659 (cit. on p. 56).
- [93] E. A. J. Marcatili and R. A. Schmelitzer. „Hollow metallic and dielectric waveguides for long distance optical transmission and lasers“. In: *Bell System Technical Journal* 43.4 (1964), pp. 1783–1809 (cit. on p. 63).
- [94] S. G. Johnson, M. Ibanescu, M. Skorobogatiy, et al. „Low-loss asymptotically single-mode propagation in large-core OmniGuide fibers“. In: *Optics Express* 9.13 (2001), pp. 748–779 (cit. on p. 67).
- [95] G. Li, M. Zeisberger, and M. A. Schmidt. „Guiding light in a water core all-solid cladding photonic band gap fiber—an innovative platform for fiber-based optofluidics“. In: *Optics Express* 25.19 (2017), pp. 22467–22479 (cit. on p. 67).
- [96] R. Fatobene, A. Hartung, B. Jang, and M. A. Schmidt. „Approximate model for analyzing band structures of single-ring hollow-core anti-resonant fibers“. In: *Optics Express* 27.7 (2019), pp. 10009–10021 (cit. on p. 69).
- [97] J. Bürger, J. Kim, B. Jang, et al. „Ultrahigh-aspect-ratio light cages: fabrication limits and tolerances of free-standing 3D nanoprinted waveguides“. In: *Optical Materials Express* 11.4 (2021), pp. 1046–1057 (cit. on pp. 72, 76).
- [98] B. Debord, A. Amsanpally, M. Chafer, et al. „Ultralow transmission loss in inhibited-coupling guiding hollow fibers“. In: *Optica* 4.2 (2017), pp. 209–217 (cit. on p. 76).
- [99] B. Jang, J. Gargiulo, R. Fatobene, et al. „Light guidance in photonic band gap guiding dual-ring light cages implemented by direct laser writing“. In: *Optics Letters* 44.16 (2019), pp. 4016–4019 (cit. on p. 76).
- [100] C. Jain, A. Braun, J. Gargiulo, et al. „Hollow Core Light Cage: Trapping Light Behind Bars“. In: *ACS Photonics* 6.3 (2018), pp. 649–658 (cit. on p. 76).
- [101] J. Kim, B. Jang, J. Gargiulo, et al. „The optofluidic light cage—on-chip integrated spectroscopy using an antiresonance hollow core waveguide“. In: *Analytical Chemistry* 93.2 (2020), pp. 752–760 (cit. on p. 76).
- [102] F. Davidson-Marquis, J. Gargiulo, E. Gómez-López, et al. „Coherent interaction of atoms with a beam of light confined in a light cage“. In: *Light: Science & Applications* 10.1 (2021), pp. 1–10 (cit. on p. 76).

- [103] B. T. Kuhlmei, B. J. Eggleton, and D. K. C. Wu. „Fluid-filled solid-core photonic bandgap fibers“. In: *Journal of Lightwave Technology* 27.11 (2009), pp. 1617–1630 (cit. on p. 77).
- [104] Y. Xu, P. Bai, X. Zhou, et al. „Optical refractive index sensors with plasmonic and photonic structures: promising and inconvenient truth“. In: *Advanced Optical Materials* 7.9 (2019), p. 1801433 (cit. on pp. 77, 93).
- [105] S. Pumpe, M. Chemnitz, J. Kobelke, and M. A. Schmidt. „Monolithic optofluidic mode coupler for broadband thermo- and piezo-optical characterization of liquids“. In: *Optics Express* 25.19 (2017), pp. 22932–22946 (cit. on pp. 78, 82, 89, 91).
- [106] M. Chemnitz, C. Gaida, M. Gebhardt, et al. „Carbon chloride-core fibers for soliton mediated supercontinuum generation“. In: *Optics Express* 26.3 (2018), pp. 3221–3235 (cit. on pp. 78, 85).
- [107] J. W. Fleming. „Dispersion in GeO₂–SiO₂ glasses“. In: *Applied Optics* 23.24 (1984), pp. 4486–4493 (cit. on pp. 83, 86, 87).
- [108] J. H. Wray and J. T. Neu. „Refractive index of several glasses as a function of wavelength and temperature“. In: *JOSA* 59.6 (1969), pp. 774–776 (cit. on p. 89).
- [109] National Institute of Standards and Technology. *NIST Chemistry WebBook*, SRD 69 (cit. on p. 89).
- [110] National Research Council et al. *International critical tables of numerical data, physics, chemistry and technology*. Vol. 7. National Academies, 1930 (cit. on p. 91).
- [111] H. El-Kashef. „Optical and electrical properties of materials“. In: *Review of Scientific Instruments* 65.6 (1994), pp. 2056–2061 (cit. on p. 91).
- [112] H. El-Kashef. „Thermo-optical and dielectric constants of laser dye solvents“. In: *Review of Scientific Instruments* 69.3 (1998), pp. 1243–1245 (cit. on p. 91).
- [113] X. Qi, K. Schaarschmidt, G. Li, et al. „Understanding Nonlinear Pulse Propagation in Liquid Strand-Based Photonic Bandgap Fibers“. In: *Crystals* 11.3 (2021), p. 305 (cit. on p. 93).

List of Figures

1.1	Key development of hollow core fibers	6
1.2	Conception of a hollow core fiber	7
2.1	Modes dispersion in SIF	18
2.2	Scalar solutions compared with vector solutions	18
2.3	Sketch for Birks' Model	19
2.4	Band gap map based on Birks' Model	22
2.5	Reflection model	25
2.6	Photonic crystal model in COMSOL	27
2.7	A Bloch mode solution in photonic crystal model in COMSOL .	28
2.8	Example modals of Photonic crystal fiber in COMSOL	29
2.9	An example in CUDOS MOF Utilities	30
3.1	Principle of the binary function from Birks' Model	35
3.2	Band gap map calculated by binary function with Birks' Model .	36
3.3	Photonic band gap maps calculated with binary functions re- garding geometry parameters	38
3.4	Fundamental band gap with varying d/Λ	40
3.5	Fundamental band gap with varying n_{hi}	41
3.6	Field profiles of the edge modes of the fundamental band gap .	42
3.7	Sketch of a single-ring microstructured fiber and the concept of the reflection model	44
3.8	Reflection-based model in COMSOL	46
3.9	Results from the reflection-based model	48
3.10	A loss map regarding d/pitch and V parameter	49
3.11	Normalized E field z component	49
3.12	Cylinder-modified single-ring antiresonant fiber	50
3.13	A loss map	52
3.14	Normalized E field z component	53
4.1	Sketch of the water-core all-solid photonic band gap fiber	56

4.2	DOS map of the water-core photonic band gap fiber.	57
4.3	Sketch of the reflection model for the water-core all-solid photonic band gap fiber	59
4.4	Planar reflection model for the water-core all-solid photonic band gap fiber in COMSOL	60
4.5	Modes dispersion of the fundamental modes of the water-core all-solid photonic band gap fiber	61
4.6	Imaginary part of the refractive index of the fundamental mode of the water-core all-solid photonic band gap fiber	62
4.7	Dependency of the imaginary part of effective index $Im(n_{eff})$ of the fundamental mode on various structural parameters for the water-core all-solid photonic band gap fiber	64
4.8	Loss map by planar reflection model for the water-core all-solid photonic band gap fiber	65
4.9	Spectral distribution of the real and imaginary part of the effective index for the three lowest order modes for the water-core all-solid photonic band gap fiber	66
4.10	Simulation of the complex effective index for the 12 strands light cage	68
4.11	Fabrication of the light cage	70
4.12	Sketch of the setup for characterization of the light cage sample	72
4.13	Transmission spectra of the light cage structures in different lengths	73
4.14	Transmission spectra of the “light cage” in length of 10.5 mm10.5 mm	74
4.15	Top view of light cage	74
5.1	Photonic crystal fibers used for the liquid-filled band gap fiber. .	79
5.2	Fabrication of the liquid-filled photnics crystal fiber.	80
5.3	The band map to be used for the LFBG fiber.	81
5.4	Optical characterization of the LFBG fiber	82
5.5	Estimated effective index used for the liquid filled in the PCF . .	84
5.6	Refractive index dispersions of liquids mixtures	85
5.7	Fitting parameters for RI of liquids mixtures	87
5.8	Refractive index of liquids bi-mixtures versus concentration . .	88

5.9	Transmission spectra of the LMA20 PCF filled with CS_2 solution regarding different environmental temperatures	89
5.10	Dispersion of the refractive index of CS_2 regarding different environmental temperatures	90
5.11	Thermal effect of the refractive index of CS_2	91
5.12	Thermo-optic coefficient of CS_2 regarding wavelength	92

List of Tables

5.1	Table of the fitting parameters for the Sellmeier equation (equation 5.1).	86
-----	--	----

Publication List

1. G. Schmidl, J. Dellith, A. Dellith, N. Teller, D. Zopf, **G. Li**, A. Dathe, G. Mayer, U. Hübner, M. Zeisberger and O. Stranik, “Silicon template preparation for the fabrication of thin patterned gold films via template stripping”, *Journal of Micromechanics and Microengineering*, 25.12 (2015), p. 125005.
2. **G. Li**, D. Zopf, G. Schmidl, W. Fritzsche and O. Stranik, “Concentric dot-ring metal nanostructures prepared by colloidal lithography”, *Applied Physics Letters*, 109.16 (2016), p. 163101.
3. **G. Li** and M. A. Schmidt, “Identification of zero density of states domains in band gap fibers using a single binary function”, *Optics Express*, 24.14 (2016), pp.16212-16221.
4. **G. Li**, M. Zeisberger and M. A. Schmidt, “Guiding light in a water core all-solid cladding photonic band gap fiber—an innovative platform for fiber-based optofluidics”, *Optics Express*, 25.19 (2017), pp. 22467-22479.
5. C. Jain, A. Braun, J. Gargiulo, B. Jang, **G. Li**, H. Lehmann, S. A. Maier and M. A. Schmidt, “Hollow core light cage: trapping light behind bars”, *ACS Photonics*, 6.3 (2018), pp. 649-658.
6. H.Chen, S. Fan, **G. Li**, M. A. Schmidt and N. Healy, “Single Crystal Ge Core Fiber Produced via Pressure Assisted Melt Filling and CO₂ Laser Crystallization”, *IEEE Photonics Technology Letters*, 32.2 (2019), pp. 81-84.
7. J. T. Zhao, C. Qi, **G. Li** and M. A. Schmidt, “An improved spectrophotometric method tests the Einstein–Smoluchowski equation: a revisit

and update”, *Physical Chemistry Chemical Physics*, 22.38 (2020), pp. 21784-21792.

8. **G. Li**, R. Fetobene, M. Zeisberger, T. Weiss and M. A. Schmidt, “Interpreting light guidance in antiresonant and photonic bandgap waveguides and fibers by light scattering: analytical model and ultra-low guidance”, *Optics Express*, 30(2) (2022), pp.2768-2779.

Ehrenwörtliche Erklärung

Ich erkläre hiermit ehrenwörtlich, dass ich die vorliegende Arbeit selbständig, ohne unzulässige Hilfe Dritter und ohne Benutzung anderer als der angegebenen Hilfsmittel und Literatur angefertigt habe. Die aus anderen Quellen direkt oder indirekt übernommenen Daten und Konzepte sind unter Angabe der Quelle gekennzeichnet.

Bei der Auswahl und Auswertung folgenden Materials haben mir die nachstehend aufgeführten Personen in der jeweils beschriebenen Weise unentgeltlich geholfen:

1. Frau Franka Jahn mit der Bereitstellung von gemessenen SEM Abbildung von Sample.

Weitere Personen waren an der inhaltlich-materiellen Erstellung der vorliegenden Arbeit nicht beteiligt. Insbesondere habe ich hierfür nicht die entgeltliche Hilfe von Vermittlungs- bzw. Beratungsdiensten (Promotionsberater oder andere Personen) in Anspruch genommen.

Niemand hat von mir unmittelbar oder mittelbar geldwerte Leistungen für Arbeiten erhalten, die im Zusammenhang mit dem Inhalt der vorgelegten Dissertation stehen.

Die Arbeit wurde bisher weder im In- noch im Ausland in gleicher oder ähnlicher Form einer anderen Prüfungsbehörde vorgelegt.

Die geltende Promotionsordnung der Physikalisch-Astronomischen Fakultät ist mir bekannt.

Ich versichere ehrenwörtlich, dass ich nach bestem Wissen die reine Wahrheit gesagt und nichts verschwiegen habe.

Jena, December 6, 2021

Guangrui Li

